Density functional theory study of oxygen and water adsorption on $SrTiO_3$(001)

D I S S E R T A T I O N

zur Erlangung des akademischen Grades

Dr. rer. nat.
im Fach Physik

eingereicht an der
Mathematisch-Naturwissenschaftlichen-Fakultät I
Humboldt-Universität zu Berlin

von
Dipl.-Phys. Hannes Guhl
17. 11. 1979, Elsterwerda

Präsident der Humboldt-Universität zu Berlin:
Prof. Dr. Dr. h.c. Christoph Markschies

Dekan der Mathematisch-Naturwissenschaftlichen-Fakultät I:
Prof. Dr. Andreas Herrmann

Gutachter:
1. Prof. Dr. Roberto Fornari
2. Prof. Dr. Norbert Koch
3. Prof. Dr. Karsten Reuter

eingereicht am: 7. 7. 2010
Tag der mündlichen Prüfung: 3. 12. 2010

Abstract

Strontium titanate is an extensively studied material with a wide range of application, for instance in photo-catalysis and most importantly, it is used as a substrate in growth of functional oxides. The surface chemistry is crucial and hence understanding the surface structure on atomic scale is essential for gaining insight into the fundamental processes in the aforementioned applications. Moreover, there exist a lot of evidence that this surface chemistry might be controlled to considerably by extrinsic species, such as residual hydrogen and water.

Investigating the properties of water and oxygen on the strontium titanate surface is certainly a natural starting point for a theoretical study based on density functional theory, because these species are practically present on the surface on a wide range of experimental conditions and they are computationally feasible.

For the oxygen and water adsorption the binding energy is controlled by long-range surface relaxations leading to an effective repulsion of the adsorbed specimen. The isolated oxygen ad-atom forms a covalently bonded "quasi-peroxide anion" in combination with a lattice oxygen atom. Contrariwise, in all investigated configurations containing water molecules and hydroxyl groups, the respective oxygen atoms assumed positions close to the oxygen sites of the continued perovskite lattice of the substrate. Most remarkably, on the strontium oxide termination, the water molecules adsorbs and dissociates effortlessly leading to the formation of a pair of hydroxyl groups. For the titanium dioxide termination, a coverage dependent adsorption mode is observed. Densely packings stabilize water molecules, whereas at lower coverage and finite temperatures the formation of hydroxyl groups is found. The energetics responsible for this behavior is consistent with recent experiments by Iwahori and coworkers.

Zusammenfassung

Strontiumtitanat ist ein häufig untersuchtes Oxidmaterial, mit einem breiten Anwendungsgebiet z.B. in der Photokatalyse oder auch als Substratmaterial beim Wachstum anderer Oxidschichten. Dabei spielen chemische Prozesse an der Oberfläche eine herausragende Rolle, deren Kenntnis für eine tieferes Verständnis der genannten Anwendungen unentbehrlich ist. Darüberhinaus gibt es deutliche Hinweise darauf, dass diese Oberflächenprozesse sehr stark, u.a. von Wasserstoff und Wasser beeinflußt werden.

Sowohl wegen der Relevanz als auch wegen der technischen Machbarkeit, stellt eine Untersuchung des Adsorptionsverhaltens von Sauerstoff und Wasserstoff mit Hilfe der Dichtefunktionaltheorie einen natürlichen Ausgangspunkt dar, um genaue Einblicke in die Prozesse auf der Oberfläche auf atomare Ebene zu gewinnen.

Bei der Adsorption des Sauerstoffs und des Wassers ist gleichermaßen auffällig, dass die Bindungsenergien sehr stark durch langreichweitige Verzerrungen im Substratgitter beeinflußt werden, welche damit eine effektive repulsive Wechselwirkung der adsorbierten Spezies bewirken. Adsorbierte Sauerstoffatome bilden mit jeweils einem Sauerstoffatom des Subtrats ein „Quasi-Peroxid-anion“, wodurch das adsorbierte Sauerstoffatom einen Gitterplatz einnimmt, der nicht einem Sauerstoffplatz des Perovskitgitters entspricht. Im Gegensatz dazu wurden bei allen untersuchten atomaren Konfigurationen, die Wasser und Hydroxylgruppen enthielten, beobachtet, dass sich hier die adsorbierten Sauerstoffatome an den Plätzen des forgesetzten Perovskitgitters befinden. Bemerkenswert ist die spontane Dissoziation und Bildung eines Hydroxylpaares auf der Strontiumoxidterminierung während des Adsorption des Wassermoleküls. Auf der Titandioxidterminierung hingegen werden abhängig von der Bedeckung Wassermoleküle und Hydroxylgruppen beobachtet. Die Energetik, die diesem Verhalten zugrunde liegt, zeigt sehr gute Übereinstimmung mit den experimentellen Beobachtungen von Iwahori und Kollegen.

Contents

1 Introduction

For its relative simplicity, strontium titanate ($SrTiO_3$) has been receiving attention in material science as a model or prototype material for scientifically and technically important more complex oxides [1]. Asides from this role, it has itself a wide range of potential and practical applications as well. Due to its high dielectric constant, $SrTiO_3$ is employed for instance in silicon complementary metal-oxide-semiconductor (CMOS) devices as a gate dielectric, because the economically desired decreasing of the devices' dimensions lead to extreme field strengths in the oxide semiconductor field effect transistors (MOSFET), which can not be withstood by the traditionally used silicon oxide and require a replacement [2, 3, 4, 5, 6, 7]. This high dielectric constant can also be exploited in microwave devices such as tunable filters or oscillators [8], whose role for today's communication technology can not be underestimated.

A very important field of application for $SrTiO_3$ is the use as a substrate material for high T_C-super-conducting [9] and ferroelectric and thin films [10], because many of these films crystallize like $SrTiO_3$ in the perovskite or a in a related structure. Especially piezo- and ferroelectric thin films of high quality have many applications of which we name only as a tip of the iceberg and to provide a basic orientation of their fundamental technological importance non-volatile memories, microwave devices optical waveguides and displays [10, 11, 12, 13, 14]. In addition, $SrTiO_3$ is also employed as gas sensing device exploiting the phenomenon that doped or oxygen reduced $SrTiO_3$ changes its electric resistivity in the environment of for instance oxygen gas [15, 16, 17, 18]. Moreover, in fundamental research hetero-structures of $SrTiO_3$ and $LaAlO_3$ serving as a model system for polar interfaces in general have recently attracted interest for the discovery of the formation of a two-dimensional electron gas at the interface, which offers itself new functionalities in future devices [19, 20, 21, 22, 23, 24].

Despite the different character of these interesting and important yet arbitrarily selected fields of applications, they have in common that their in-depth understanding depends on the ability to define and atomically flat $SrTiO_3$ surface as well as the chemical reactions and growth processes on it. Clearly, too rough and undefined $SrTiO_3$ surfaces will effectively lower the quality of the high-T_C super-conducting and ferroelectric thin films, a too bumpy $SrTiO_3$/$LaAlO_3$ interface will most likely not promote the emergence of delocalized electronic states and the adsorption of gas phase molecules on the surface is what make the gas sensor finally work. Consequently, research has also focused on fundamental chemical reactions and processes on $SrTiO_3$ as well as on the surface morphology itself.

However, the multitude of the experimental studies subjected to the surface of $SrTiO_3$ and its interaction with gas phase species and despite the various techniques that have been applied, reflect well the number of possible models and pictures of the physics of this system. While in early studies in the 1970's mostly conclusions were hampered simply by too disadvantageous signal-to-noise ratios, the number of experimentally observed reconstructions and surface formations increased remarkably and formed a zoo of structures such as for instance the forma-

tion of strontium oxide (SrO) islands [25], stoichiometric changes towards Ruddlesden-Popper phases [26], strontium ad-atom patterns [27] and TiO_2 double-layered structures [28]. Upon sputtering with Ar^+-ions, Brookes *et al.* found their $SrTiO_3$ samples to be terminated predominantly by a SrO-layer [29], whereas Henrich *et al.* [30] observed mainly TiO_2-planes on top of their samples after the applying the same procedure. The diversity of these few selected examples suggests that the actual surface morphology of this materials actual depends on the details in the sample preparation procedure, which was convincingly demonstrated eventually by Erdmann and Marks by showing that three different reconstructions on the TiO_2-terminated surface may appear in on relatively similar ambient conditions [31]. This situation leaves the industrial and scientific users of $SrTiO_3$-surfaces with tedious approach of trial-and-error in order to determine the appropriate procedures and techniques for preparing their samples. A way to find remedy is certainly to attack the problem with theoretical methods, of which the framework of density-functional theory (DFT) is most likely to make contact to experiment for its relative good reliability in combination with the ability to treat systems of experimentally relevant size. However, first the results of first serious DFT-studies were not very encouraging, for instance Johnston *et al.* [32] and Heifets *et al.* [33] could not support the proposed TiO_2 double layer over-structures proposed by Erdmann *et al.* as the thermodynamic equilibrium state, and similarly as Liborio *et al.* qualified Kubo and Nozoye's strontium ad-atom patterns as merely meta-stable structures. In contrast, theoetical works agree on the fact that only the relaxed but unreconstructed SrO and TiO_2 layers surface represent the equilibrium termination of the $SrTiO_3$(001) surfaces. Additionally, preceding theoretical studies on water adsorption on $SrTiO_3$ could also not to contribute substantially to the understanding of the numerous experimental studies addressing this subject [34, 35, 36, 37, 38]. However, understanding the interaction of water, hydroxyls and hydrogen is exceptionally important from the scientific as well as the industrial employers' point of view. Strontium titanate has been found to photocatalyze the dissociation of water upon ultraviolet light into hydrogen (H_2) and oxygen (O_2) gas [39, 40, 41] a phenomenon, which was at first observed at titania (TiO_2) electrodes [42] and whose potential importance for utilizing solar energy to hydrogen fuel production is obvious [43]. Doping the $SrTiO_3$ sample with for instance Rh atom promotes this reaction even upon irradiation of visible light [44] and coating $SrTiO_3$ it with platinum seems to amplify this process even further [45]. However, solar hydrogen production in general and in particular using $SrTiO_3$ as a photo-catalyst is still far from being application-ready because of many fundamental problems, which are partly connected again to the problem of the exact definition and atomic control of the surface of $SrTiO_3$ [46]. We mention here that in spite of the much greater attention TiO_2 has received in past and present [47], $SrTiO_3$ appears to have similar if not even advantageous photo-catalytic properties compared to the latter material [39]. On the other hand, the film-grower's concern for water and hydrogen comes from another side. These two species can never be really excluded in growth processes, not even in ultra-high vacuum (UHV) techniques such as the molecular beam epitaxy (MBE) and especially not in "dirty" techniques relevant in industry-scale applications such a metal-organic chemical vapor deposition (MOCVD) or metal organic vapor phase eptiaxy (MOVPE) [48, 49, 50]. It is virtually unknown, how in detail these species take part in the entire growth process, albeit some surface formations are only obtained with the assistance of hydrogen [51] and another study reported an increased growth rates of homo-epitaxial grown $SrTiO_3$ [52] In addition, a very recent studies could demonstrated the

nano-pattering of organic molecules and the formation of $SrRuO_3$ nano-structures on $SrTiO_3$ in a *humid* ambient, showing that the understanding the interaction of water with $SrTiO_3$ as representative for more complex oxides materials is of utmost importance especially for oxide film growth [53, 54].

The importance of the issue and the still open questions by experiment and theory provided the main motivation of this work for an systematic in-depth study of the water adsorption and dissociation on $SrTiO_3$ by means of state-of-the-art DFT framework. Before presenting our results concerning the water molecules in Chapter 5, we discuss at first in Chapter 4 the results of our similarly systematic study of the oxygen ad-atoms on the $SrTiO_3$ surface. These calculations were motivated mostly by crucial interaction of $SrTiO_3$ and oxygen in standard sample preparation procedures and of course, because it is also part of most of the grown films on $SrTiO_3$ substrates. We will also use this issue as a special example to introduce the formalism of the first-principles thermodynamics, which we also apply for the adsorbed water molecule and in which the relevance of electronic structure calculations for rationalizing the experimental observations is eventually manifested. In Chapter 6 we will then summarize our tentative results concerning the adsorption of hydrogen ad-atom, hydroxyls and hydrogen co-adsorbed oxygen molecules. Before addressing the results, we briefly summarize in Chapters 2 and Chapter 3 the applied electronic structure methods applied in this work as well as some general properties of bulk $SrTiO_3$ and its surfaces accompanied with the verification of the applied theoretical models. Readers being familiar with these topics, having faith in the appropriateness of our way to model the $SrTiO_3$ surface and being interested only in the actual results are advised to skip the next two chapters without any apprehensions.

2 Density functional theory

Density functional theory (DFT) is nowadays the most popular technique to attack the quantum-mechanical electronic many-body problem with a fundamental, in principle parameter-free approach for real solids, surfaces, molecules, nano-structures etc. The reason for this popularity is the balance of accuracy as well as the relative favorable computational costs, allowing to treat already realistic solids on a desktop computer and huge systems comprising several hundred atoms are still feasible on super-computers.

In this chapter provides a brief overview about the central aspects of DFT itself as well as the essential technicalities for its application within this thesis. For a detailed introduction to method in general we refer the reader to book of Dreizler and Gross [55].

2.1 Many-body hamiltionian

With the advent of quantum mechanics in the first half of the 20th century it became clear that matter has to be described strictly within wave-functions rather than the hitherto used particles. However, due mass of the atomic nuclei m_n being at least three orders of magnitude larger than that of the electrons m_e, the motion of the atomic nuclei evolves on a much larger time scale than that of the motion of the electrons. If the latter are stipulated to equilibrate adiabatically with respect to changes in the nuclei's positions, these two subsystems may be decoupled from each other the corresponding equations may be solved separately. This approximation was first introduced by Born and Oppenheimer and is quite reasonable for systems of interest in solid state physics and chemistry [56], but fails at extremely high energies, in plasma or in non-radiative transition is solids, i. e. electron-phonon coupling. Thus, the atomic nuclei are considered merely as classical point charges and masses exerting a potential on the fully quantum mechanically treated electrons. The positions $\mathbf{R}_i$ of the M atomic nuclei are mathematically nothing but parameters for the time-independent Schrödinger equation for the complex all electron wave-function Ψ_N of the N electrons in the system under consideration. In real-space representation of the electronic coordinates $\mathbf{r}_i$ the Schrödinger equation to solve reads then:

$$H\Psi_N(\mathbf{r}_1,\mathbf{r}_2,\ldots,\mathbf{r}_N) = E\Psi_N(\mathbf{r}_1,\mathbf{r}_2,\ldots,\mathbf{r}_N) \quad , \tag{2.1}$$

providing the total energy E of the system. The resulting Hamiltionian for the entire system reads then in atomic units relating the elementary charge e to $e = m_e = \hbar = 1$:

$$H = -\frac{1}{2}\sum_i \Delta_i - \frac{1}{2}\sum_{i\neq j}\frac{Z_i Z_j}{|\mathbf{R}_i-\mathbf{R}_j|} - \frac{1}{2}\sum_i\sum_j \frac{Z_j}{|\mathbf{r}_i-\mathbf{R}_j|} - \frac{1}{2}\sum_{i\neq j}\frac{1}{|\mathbf{r}_i-\mathbf{r}_j|} \quad , \tag{2.2}$$

where Δ_i denotes the Laplacian with respect to the spatial coordinates of the ith electron. The four terms represent from left to right the kinetic energy of the electrons, the coulomb repulsion of all the nuclei with the atomic number Z_i, the coulomb interaction of the electrons with the nuclei and the coulomb interaction of the electrons with each other. The factor of $\frac{1}{2}$ of the last three terms corrects for the double-counting of the pair-interaction. of the ith nucleus and the in jth electron. The interaction of the particles with themselves in the second and the last sum has to be excluded explicitly from the sumation for obvious reasons. Equation (2.1) represents a partial differential equation for $3N$ variables and can not be attacked analytically for systems having more than $N = 2$ particles. Brute force numerical methods are also limited for slightly larger problems for the finiteness of the computer memory and for the finiteness of the human lifetime. Thus, one has to be content with approximations. Mathematically, Eq. (2.1) poses the problem of finding the spectrum of the n eigenvalues E_n and the corresponding eigenstates Ψ_n of the hermitian operator H. It can be shown that there exists a lower boundary for the eigenvalues and it is practical to focus at first on the lowest one, i. e. $n = 0$, which will be referred to in the following as the ground-state. The ground-state contains already substantial information about the many-particle system, because it is known from every day experience that this is state in which all physical system will tend to assume. In turn, if we have found an algorithm being capable of calculating the ground-state wave-function Ψ_0 and the ground-state energy E_0 exactly, we can formulate a similar problem to obtain subsequently all further, i. e. excited eigenenergies and eigenstates of the original problem:

$$H \rightarrow H - E_0 \left|\Psi_0\right\rangle \left\langle\Psi_0\right| \quad , \tag{2.3}$$

where we have used the common abstract bracket nomenclature to denote the eigenstates Ψ_n of the Schrödigner equation.

Still, the exact calculation of the ground-state wave-function and the ground-state energy is formidable problem, which we will be hereafter only concerned with and which lets us drop the subscript enumerating the individual eigenstates.

For any test wave-function Ψ_{Test} one may calculate the corresponding test energy $E_{\text{Test}} = \left\langle\Psi_{\text{Test}}\right| H \left|\Psi_{\text{Test}}\right\rangle$, which has to be greater than the actual truly exact ground-state energy. Thus, minimizing E_{Test} yields also a representation of an approximate ground-state wave-functions, which is the essential statement of the variational principle.

2.2 Hartee-Fock approximation

Quantum mechanics teaches that the wave-function itself contains all accessible information physics of electronic system but its not an observable itself, because it may have numerous, yet equivalent representations. A physically significant quantity being directly derived from Ψ in the real space representation is certainly the electronic density $n(\mathbf{r})$:

$$n(\mathbf{r}) = N \int \ldots \int \mathrm{d}r_2^3 \ldots \mathrm{d}r_N^3 |\Psi(\mathbf{r}, \mathbf{r}_2, \ldots, \mathbf{r}_N)|^2 \quad , \tag{2.4}$$

which is indeed nothing but the probability to find an electron within the infinitesimal volume element dr^3 multiplied by N. A simple Ansatz was introduced by Hartree for the all-electron ground-state wave-function and is based on the assumption that the electrons are described in the absence of any atomic nuclei, external potentials and infinite spatial separation for each other as the product of the N individual one-electron wave-functions ψ_i [57]:

$$\Psi_N(\mathbf{r}_1,\ldots,\mathbf{r}_N) \stackrel{!}{=} \psi_1(\mathbf{r}_1)\psi_2(\mathbf{r}_2)\psi_3(\mathbf{r}_3)\ldots\psi_N(\mathbf{r}_N) \qquad \text{with} \quad \psi_i(\mathbf{r}_i) = \varphi_i(\mathbf{r}_i)\chi_i \quad , \tag{2.5}$$

where $\varphi_i(\mathbf{r}_i)$ denotes the spatial wave-function of the ith electron and χ_i stands for its spin-function. Note that the wave-function and the coordinates of the ith electron is marked individually. Whereas in Newtonian mechanics identical particles can by distinguished by means of the strict determinism and the initial conditions, in quantum mechanics they can not. Therefore, any one-electron wave-function depends only on the coordinates of one electron in an one-electron system, in a many-electron system all coordinates may serve in principle as arguments. Thus, the shape of all-electron wave-function in Eq. (2.5) is just one special case, in fact, all permutations of the spatial variables have to be considered and the most general Ansatz is certainly the normalized sum of all these permutations:

$$\Psi(\mathbf{r}_1,\mathbf{r}_2,\ldots,\mathbf{r}_N) = \frac{1}{\sqrt{N!}}\sum_{\{P\}}(\pm 1)^{p(P)}P[\psi_1(\mathbf{r}_1),\ldots,\psi_N(\mathbf{r}_N)] \quad , \tag{2.6}$$

where the operator P realizes one special of the $N!$ possible permutations comprising the simultaneous exchange of the spatial coordinates of p electrons. For the sake of most generality, we have to allow in principle the change of the sign of Ψ upon exchange of two electron coordinates. Any physically relevant observable such as for instance the electron density are not altered by this operation as it can be seen directly in Eq. (2.4). Pauli showed that for particles having a half-numbered spin, i. e. Fermions and in particular electrons with a spin of $\frac{1}{2}$, the negative sign applies strictly in the last expression [58]. Consequently, the all-electron wave-function assumes the shape of a determinant, which is being called in this context “Slater-determinant”. In fact, if two all-electrons posses an identical set of quantum numbers, Ψ vanishes exactly and therefore such a state can not exist. This is of course nothing but a reformulation of the Pauli’s exclusion principle [59].

The Ansatz of the wave-function in Eq. (2.6) can now be used in combination with the variational principle to calculate the approximate ground-state energy on the necessary condition that the number of electrons is conserved. This introduces a set of Lagrange-multipliers ε_i playing the role one-particle energies of the one-particle wave-functions ψ_i. The sum of these ε_i represents then the approximate total ground-state energy. The reduction of the initial many-body problem to N effective coupled single particle problems is a feature of the Hartree-Fock approximation, which lets each single-particle feel only an effectively averaged or mean-field-potential created by all the other electrons. This shortcoming can be remedied with higher-level techniques such as for instance the coupled-cluster method [60], the Møller-Plesset perturbation theory [61], the Greens-function technique [62, 63].

The actual derivation of the Hartree-Fock equations was performed at first by Fock [64] and can be found in many textbooks today in the version of Slater [65]. Because it involves some

algebra we skip it for the sake of brevity and proceed directly with discussing the result. In the following the contribution due to the coulomb repulsion of the atomic nuclei will be omitted, because it induces only an energetic shift being of no importance here. Next we introduce an abbrevation for the one-electron contribution in Eq. (2.2) of the kinetic energy and the electron ion-interaction:

$$H_i^{(0)} = \int \mathrm{d}r_\alpha^3 \psi_i^*(\mathbf{r}_\alpha) \left[-\frac{1}{2}\Delta_\alpha - \sum_j \frac{Z_j}{|\mathbf{r}_\alpha - \mathbf{R}_j|} \right] \psi_i(\mathbf{r}_\alpha) \quad . \tag{2.7}$$

The Hartee-Fock equations read then:

$$\varepsilon_i \psi_i(\mathbf{r}_\alpha) = H_i^{(0)}(\mathbf{r}_\alpha)\psi_i(\mathbf{r}_\alpha) + \sum_j \left[\int \mathrm{d}r_\beta^3 \frac{|\psi_j(\mathbf{r}_\beta)|^2}{|\mathbf{r}_\alpha - \mathbf{r}_\beta|} - \int \mathrm{d}r_\beta^3 \frac{\psi_j^*(\mathbf{r}_\beta)\psi_i(\mathbf{r}_\beta)}{|\mathbf{r}_\alpha - \mathbf{r}_\beta|} \right] \psi_i(\mathbf{r}_\alpha) \quad , \tag{2.8}$$

where the term in the squared brackets contains the classically expected mutual repulsion of the electrons and the a non-classical term due to the exchange of the electronic spatial coordinates. The remarkable feature is that for $i = j$ both terms cancel and manifest therefore the absence of non-physical self-interactions of the electrons. In a purely classical treatment this would have to be enforced only by explicit exclusion of the respective terms from the summation. The second issue to note is that due to the strict orthogonality of the spin-functions, only electrons with a parallel spin contribute to the exchange-term. This lets the energy decrease only due to the anti-symmetry of the all-electron wave-functions keeping spin-parallel electrons apart from each other and creates consequently an effective depletion of electron density at the point $\mathbf{r}$ due to the presence of another electron located around $\mathbf{r}'$. We try to illustrate this a little bit more by defining a general the electron pair density, which is being related to the electron density in Eq. (2.4):

$$n(\mathbf{r},\mathbf{r}') = N(N-1) \int \mathrm{d}r_3^3 \ldots \mathrm{d}r_N^3 |\Psi(\mathbf{r},\mathbf{r}',\ldots,\mathbf{r}_N)|^2 \quad , \quad n(\mathbf{r}) = \frac{1}{N-1} \int \mathrm{d}r'^3 n(\mathbf{r},\mathbf{r}') \quad . \tag{2.9}$$

This quantity can be viewed as the probability to find in a system of N electrons two of them simultaneously within the volume elements at $\mathbf{r}$ and $\mathbf{r}'$. In the classical limit, where the electrons would interact with each other only via the bare coulomb repulsion, the electron-pair density is exactly the product of the density at the points $\mathbf{r}$ and $\mathbf{r}'$. Using the many-particle ground-state wave-function obtained within Hartree-Fock approximation, we rewrite the pair density as a sum of these densities and a modifying term, which should contribute predominantly at close distances and which should also be proportional to the electron density itself:

$$n(\mathbf{r},\mathbf{r}') = n(\mathbf{r})n(\mathbf{r}') + n(\mathbf{r})n_\mathrm{X}(\mathbf{r},\mathbf{r}') \quad . \tag{2.10}$$

The last expression defines the exchange- or "Fermi"-hole" $n_\mathrm{X}(\mathbf{r},\mathbf{r}')$, which depends on two points in space and allows to visualize the effect of the anti-symmetry of the electronic wave-function in terms of the electron densities. Integration over $\mathbf{r}'$ and combining the last expressions

yields then two important relations:

$$\int \mathrm{d}r'^3 n_\mathrm{X}(\mathbf{r},\mathbf{r}') = -1 \qquad\qquad E_\mathrm{X} = \frac{1}{2}\int \mathrm{d}r^3 n(\mathbf{r}) \int \mathrm{d}r'^3 \frac{n_\mathrm{X}(\mathbf{r},\mathbf{r}')}{|\mathbf{r}-\mathbf{r}'|} \quad , \tag{2.11}$$

where the second one defines the exchange energy of the many-electron system. Furthermore, for collapsing points $\mathbf{r}$ and $\mathbf{r}'$ and two spin-parallel electrons the two-electron density vanishes, suggesting that the exchange-hole computes here in spin-saturated systems with equal number of spin-up and spin-down electrons to the half of the negative density. Consequently, it should be restricted in general to negative values as well, i. e.,

$$n_\mathrm{X}(\mathbf{r},\mathbf{r}) = -\frac{1}{2}n(\mathbf{r}) \qquad\qquad n_\mathrm{X}(\mathbf{r},\mathbf{r}') \leq 0 \quad . \tag{2.12}$$

Subtracting the first term on the right hand side gives Eq. (2.10) the general shape of a correlation function and suggests the definition of the so-called correlation energy [66]:

$$E_\mathrm{Corr} = E_\mathrm{Exact} - E_\mathrm{HF} \quad , \tag{2.13}$$

as the difference of E_Exact being the total ground-state energy obtained from the strictly exact, in most cases unknown solution of the all-electron Schrödinger equation and E_HF being the same energy obtained within Hartree-Fock approximation for the same Hamiltonian. Therefore, the "correlation energy" includes misleadingly only energy contributions due to the correlation of electrons with anti-parallel spin orientation. Unsurprisingly, the evaluation of this term is possible only in some limiting cases and finding decent approximations for realistic systems is a formidable task and subject of ongoing research. One of those limiting cases is the homogeneous electron gas, for which Noziére and Pines [67] derived an approximate expression of the total energy in Rydbergs:

$$E = \frac{2.21}{r_\mathrm{S}^2} - \frac{0.916}{r_\mathrm{S}} - 0.115 + 0.031\ln(r_\mathrm{S})\ldots \qquad \text{with} \qquad r_\mathrm{S}^3 = \frac{3}{4\pi n a_\mathrm{B}} \quad , \tag{2.14}$$

where a_B is the Bohr-radius, such that r_S gives a measure of the average electron-electron distance in a homogeneous electron gas with the density n. Here, the first two terms on the right hand side are calculated within the Hartree-Fock approximation and thus the remaining terms represent the correlation energy.

2.3 The density as key variable

Whereas many strategies to tackle the many-body problem outlined in Section 2.1 are based on wave-functions, using the electron density as primary variable does provide insight into the problem as well, which we were trying to hint at in the last paragraphs. Another advantage of the electron density is that it is a physical intuitive quantity, which is certainly not the case for a N-particle wave-function, if N becomes very large. In fact, for systems with more than only 1000 electrons, there are fundamental arguments that cast doubt on the legitimation of such a very-many wave-functions as a practical scientific concept [68].

Historically, the electron density was used as a key variable at first by Thomas and Fermi [69], leading to a number of expression tractable at that time and paving the way for the density functional theory to come. However, the actual results obtained with the Thomas-Fermi model are inaccurate rendering this approach interesting only for educational purposes and we will go further into it.

The actual breakthrough for density functional theory was made by Hohenberg and Kohn in 1964, when they delivered a strict prove that the ground-state wave function of an electron gas exerted to an external potential $V_{\text{Ext.}}$ can be bijectively mapped onto the corresponding ground-state electron density [70]. The other way around, a given ground-state density determines up to an arbitrary constant uniquely $V_{\text{Ext.}}$ and consequently any observable in the ground-state of the possibly very complex many-body system. The ground-state total energy of such a many-body system as a special but important observable can be written:

$$E[n(\mathbf{r})] = F[n(\mathbf{r})] + \int \mathrm{d}r^3 V_{\text{Ext.}}(\mathbf{r}) n(\mathbf{r}) \quad , \tag{2.15}$$

where $F[n(\mathbf{r})]$ is the universal Hohenberg-Kohn functional, depending exclusively on the electron density in the entire space. In a second step Hohenberg and Kohn proved that for this ground-state energy the variational principle strictly holds. Thus, as it will approach the exact ground-state energy, minimizing E with respect to the density $n(\mathbf{r})$ is the central task within DFT.

In addtion, the last form illustrates furthermore that the "external" potential is one arising only due the interaction with the atomic nuclei being represented by the third term in the many-body Hamiltonian in Eq. (2.2). Hence, increasing complexity of the system of interest does not form a principle obstacle for DFT. The functional $F[n(\mathbf{r})]$ contains only fundamental contributions such as kinetic energy and the remaining electron-electron interactions:

$$F[n(\mathbf{r})] = T_0[n(\mathbf{r})] + E_{\text{XC}}[n(\mathbf{r})] + \frac{1}{2}\int\int \frac{n(\mathbf{r})n(\mathbf{r}')}{|\mathbf{r}-\mathbf{r}'|}\mathrm{d}r^3\mathrm{d}r'^3 \quad . \tag{2.16}$$

The last term represents obviously the classically expected electron-electron repulsion or Hartree contribution to the total energy and will labeled $E_{\text{Hartree}}[n(\mathbf{r})]$ in the following letting us introduce the Hartree-potential as well:

$$E_{\text{Hartree}}[n(\mathbf{r})] = \int \mathrm{d}r^3 V_{\text{Hartree}}(\mathbf{r}) \quad , \qquad V_{\text{Hartree}}(\mathbf{r}) = \frac{1}{2}\int \mathrm{d}r'^3 \frac{n(\mathbf{r}')}{|\mathbf{r}-\mathbf{r}'|} \quad . \tag{2.17}$$

The first term $T_0[n(\mathbf{r})]$ computes the kinetic energy of the system with an electron density $n(\mathbf{r})$ for the hypothetical case of total absence of electron-electron interactions being symbolized by the subscript. This purely mathematical trick enabled Kohn and Sham to decouple the N-particle problem into N single-particle problems [71]. The contribution to the kinetic energy due to the electron-electron is then subsumed with all further non-classical terms to the exchange-correlation energy E_{XC}, which will be commented on forward below. The great advantage of this approach over the preceding Thomas-Fermi equations is that this interaction-free kinetic energy may be treated exactly for the hypothetical interaction-free electrons of which each is

being described in a single-particle wave-function $\varphi_i(\mathbf{r})$. With the definition of the exchange-correlation energy per particle $\varepsilon_{\mathrm{XC}}(\mathbf{r})$ and the exchange correlation potential $V_{\mathrm{XC}}(\mathbf{r})$

$$E_{\mathrm{XC}}[n(\mathbf{r}] = \int \mathrm{d}r^3 n(\mathbf{r})\varepsilon_{\mathrm{XC}}(\mathbf{r}) \qquad V_{\mathrm{XC}}(\mathbf{r}) = \frac{\delta E_{\mathrm{XC}}[n(\mathbf{r}]}{\delta n(\mathbf{r})} = \frac{\mathrm{d}[n(\mathbf{r})\varepsilon_{\mathrm{XC}}(\mathbf{r})]}{\mathrm{d}n(\mathbf{r})} \quad , \tag{2.18}$$

we lump together the latter, V_{Ext} and V_{Hartree} into one effective local one particle potential $V_{\mathrm{Eff}}(\mathbf{r})$. Variation of $E[n(\mathbf{r})]$ about the ground state density yields then with a Lagrange multiplier λ:

$$\frac{\delta T_0[n(\mathbf{r})]}{\delta n(\mathbf{r})} + V_{\mathrm{Eff}}(\mathbf{r}) = \lambda \quad , \tag{2.19}$$

which can be solved by N single particle Schrödinger equations [65]:

$$\left(-\frac{1}{2}\Delta + V_{\mathrm{Eff}}(\mathbf{r})\right)\varphi_i(\mathbf{r}) = \varepsilon_i\varphi_i(\mathbf{r}) \quad \text{with} \quad n(\mathbf{r}) = \sum_i |\varphi_i(\mathbf{r})|^2 \quad \text{and} \quad \sum_i \varepsilon_i = \lambda \quad . \tag{2.20}$$

These equations are called Kohn-Sham equations and express eventually the mapping the many particle interaction to N interaction-free single particles of which each is feeling the potential caused by the remaining $N-1$ particles. The fictitious interaction-free electrons have then the so-called Kohn-Sham eigen-energies ε_i and occupy the so-called Kohn-Sham orbitals $\varphi(\mathbf{r})$. Strictly speaking, the latter quantities are not physically relevant, only the total density and the energy constructed from them is essential. On the other hand, we realize that the Kohn-Sham eigen-energies can also be understood as the partial derivative of the total ground-state energy with respect to the occupation number of the orthogonal Kohn-Sham orbitals [72]. Thus, in practice the Kohn-Sham eigenvalues and orbitals are identified frequently with the real physical electron wave-functions and energies.

The Kohn-Sham equations have to be solved self-consistently in a similar manner as the Hartree-Fock equations. Starting with a set of trial wave-functions, one constructs the effective potential $V_{\mathrm{Eff}}(\mathbf{r})$ and solves Eq. (2.20) to obtain a new set of wave-functions. This procedure called any self-consistent-cycle (SCF-cycle) is repeated continued until the input density electron density equals the output density, i. e. until it is self-consistent. The kinetic energy can then be calculated:

$$T_0[n(\mathbf{r})] = -\frac{1}{2}\sum_i \int \mathrm{d}r^3 \varphi_i(\mathbf{r})^* \Delta\, \varphi_i(\mathbf{r}) \quad , \tag{2.21}$$

letting us finally compute the ground-state energy from Eq. (2.15). For the sake of clarity, we have dropped here the factor of two for the spin-degeneracy of the orbitals. In principle, if there existed a recipe how to construct exchange-correlation energy $E_{\mathrm{XC}}[n(\mathbf{r})]$ exactly from a given density, the grounds-state properties of any physical atomic system could be calculated exactly on the basis of the hitherto developed DFT-formalism. However, this recipe is presently unknown letting us therefore compile some fundamental properties of this functional.

Given the exact many-body ground-state wave-function being of the Hamiltonian in Eq. (2.2) lets us calculate again the electron pair density defined in Eq (2.9). Consequently, we may write down an analogue for Eq. (2.10), defining the exchange correlation hole $n_{\mathrm{XC}}(\mathbf{r},\mathbf{r}')$, which can

be used to obtain the in full analogy exchange correlation energy: Eq. (2.11):

$$E_{\mathrm{XC}}[n(\mathbf{r})] = \frac{1}{2}\int \mathrm{d}r^3 n(\mathbf{r}) \int \mathrm{d}r'^3 \frac{n_{\mathrm{XC}}(\mathbf{r},\mathbf{r}')}{|\mathbf{r}-\mathbf{r}'|} \quad \text{with} \quad n_{\mathrm{XC}}(\mathbf{r},\mathbf{r}') = n_{\mathrm{X}}(\mathbf{r},\mathbf{r}') + n_{\mathrm{C}}(\mathbf{r},\mathbf{r}') \quad , \tag{2.22}$$

where we have introduced in addition the correlation hole $n_{\mathrm{C}}(\mathbf{r},\mathbf{r}')$. It is intuitively clear that similar to the pure exchange-hole, $n_{\mathrm{XC}}(\mathbf{r},\mathbf{r}')$ should tend to zero in the limit of very distant positions $\mathbf{r}$ and $\mathbf{r}'$. An integration over one spatial variable similar to Eq. (2.11) yields then

$$\int \mathrm{d}r'^3 n_{\mathrm{XC}}(\mathbf{r},\mathbf{r}') = -1 \quad , \qquad \int \mathrm{d}r'^3 n_{\mathrm{C}}(\mathbf{r},\mathbf{r}') = 0 \quad , \tag{2.23}$$

saying that the exchange-correlation hole contains exactly one electron and implying that the relations in Eq. (2.12) apply also for $n_{\mathrm{XC}}(\mathbf{r},\mathbf{r}')$. Furthermore, we estimate the exchange-correlation hole for collapsing points in space in full analogy to Eq. (2.12):

$$-\frac{1}{2}n(\mathbf{r}) \geq n_{\mathrm{XC}}(\mathbf{r},\mathbf{r}) \geq -n(\mathbf{r}) \quad , \tag{2.24}$$

The upper bound corresponds to the total absence of the correlation, implying that the Hartree-Fock approximation delivers already the exact solution of the Schrödigner equation. The lower bound in turn suggests that the correlation energy in Eq. (2.13) dominates over the pure exchange energy in Eq. (2.11). Because both the exchange-correlation-hole and the pure exchange hole tend to zero in the limit of large distances, the last relation also implies that the correlation has its largest effects only on short distances.

Exploiting the isotropic character of the coulomb interaction we rewrite E_{XC} after substitution of $\mathbf{r}'' = |\mathbf{r}-\mathbf{r}'|$:

$$E_{\mathrm{XC}}[n(\mathbf{r})] = \frac{1}{2}\int \mathrm{d}r^3 n(\mathbf{r}) \int \mathrm{d}r'' r''^2 \frac{1}{r''} \int \mathrm{d}\Omega n_{\mathrm{XC}}(\mathbf{r},\mathbf{r}'') \quad , \tag{2.25}$$

such that we may evaluate the inner integral in spherical coordinates. This form makes clear that E_{XC} depends only on the spherical average of the exchange-correlation hole, Thus, the actually important ground-state energy does not depend crucially on details of n_{XC}, which raises hopes that also relatively simple approximations for $n_{\mathrm{XC}}(\mathbf{r},\mathbf{r})$ may yield already realistic estimations for $E_{\mathrm{XC}}[n(\mathbf{r})]$. In order to abbreviate the nomenclature we introduce the exchange-correlation energy per particle $\varepsilon_{\mathrm{XC}}(\mathbf{r})$ and the exchange-correlation potential by setting where the mid-term in the last equality stands for the functional variation of the $E_{\mathrm{XC}}[n(\mathbf{r}]$ with respect to the electron density. Of course, the variational principle holds for any approximation for $\varepsilon_{\mathrm{XC}}$, however, it is not ensured that this certain approximation describes then the correct physics of the Schrödinger equation. Thus, solving Eq. (2.15) can result ground-state energies below the one that would be obtained from the exact solution Eq. (2.2) showing that approximation for the exchange-correlation functional is not systematically improvable. Consequently, the focus has shifted from solving the Schrödinger equation to find a decent approximation for the exchange-correlation energy per electron.

2.4 Common exchange-correlation functionals

Since it is universal, the most straightforward way to approximate the exchange-correlation functional $E_{\mathrm{XC}}[n]$ is simply to calculate it exactly for a special system of low complexity and then apply this solution to the actually interesting systems of high complexity. Such a simple toy-system is the homogeneous electron gas, whose total energy can be represented approximately with the expansions in Eq. (2.14). A numerically exact solution for this problem has been in delivered by Ceperly and Alder [73], which may then serve to provide a parameterization of the total energy for any density in the homogeneous electron gas [74]. The exchange-correlation energy of the complex system reads then

$$E_{\mathrm{XC}}^{\mathrm{LDA}}[n(\mathbf{r})] = \int n(\mathbf{r}) \varepsilon_{\mathrm{XC}}^{\mathrm{Hom.}}[n(\mathbf{r})] \quad , \tag{2.26}$$

where $\varepsilon_{\mathrm{XC}}^{\mathrm{Hom.}}[n(\mathbf{r})]$ is the exchange-correlation energy of the homogeneous electron gas having a density found at the point $\mathbf{r}$ in the system under investigation. The label LDA stands for local density approximation reflecting the fact that only the density at the point $\mathbf{r}$ contributes to the exchange-correlation energy, whereas the exact functional is strictly speaking a function of the entire space as illustrated in Eq. (2.22). Neglecting the modifications due to density inhomogeneities is in fact a serious approximation, but thanks significance of the spherical average of $n_{\mathrm{XC}}(\mathbf{r},\mathbf{r}')$ and the fact that the LDA obeys the relations in Eq. (2.24) [75, 69], it works remarkably well for solids with a rather slowly varying electron density, for instance simple metals. For systems with huge density inhomogeneities such as isolated molecules the LDA fails in most case to provide an accurate description. Typically, the LDA overestimates severely the strength of chemical bonds and underestimates thereby the dimension of lattice constants and bond lengths.

Before proceeding we note that using exclusively the electronic density as the key variable is sufficient only in strictly diamagnetic system, i. e. in absence of any net spin polarization of the system. However, the total electron density itself does not contain any information about the electronic spin, whose effects entered hitherto only implicitly with the behavior of the exchange-correlation functional. Considering para-, ferro- or anti-ferromagnetic systems on the other hand require an explicit treatment of the densities of the spin-up and spin down electrons, because here the spin polarization is an important physical observable. The incorporation of the explicit spin-up and spin-down densities $n_{\uparrow}(\mathbf{r})$ and $n_{\downarrow}(\mathbf{r})$ into the DFT-LDA formalism was introduced by Barth and Hedin and Gunnarson and Lundquist [76, 77] allowing us write the LDA exchange-correlation energy formally as:

$$E_{\mathrm{XC}}^{\mathrm{LSDA}}[n_{\uparrow}(\mathbf{r}), n_{\downarrow}(\mathbf{r})] = \int n(\mathbf{r}) \varepsilon_{\mathrm{XC}}^{\mathrm{Hom.}}[n_{\uparrow}(\mathbf{r}), n_{\downarrow}(\mathbf{r})] \quad , \qquad n(\mathbf{r}) = n_{\uparrow}(\mathbf{r}) + n_{\downarrow}(\mathbf{r}) \quad , \tag{2.27}$$

where LSDA stands for local spin approximation. Within this formulation, minimizing the total energy can be more efficient even for diamagnetic systems, because the degrees of freedom for optimizing the density has effectively doubled. In the following, we will use for the sake of brevity this spin-polarization only when absolutely inevitable,

An intuitive extension of the LDA to surmount at least partly the strict locality is the inclusion

of density gradients into the exchange-correlation [78, 79, 80]. Earliest suggestions date back to Hohenberg and Kohn themselves [70], however, the incorporation of the density gradient does not necessarily improve the results with respect to real physics [81].

The general form of the exhange-change correlation in the generalized gradient approximation (GGA) reads:

$$E_{\mathrm{XC}}^{\mathrm{GGA}}[n(\mathbf{r})] = \int \mathrm{d}r^3 f(n(\mathbf{r}), \nabla n(\mathbf{r})) \quad , \tag{2.28}$$

where the function $f(n(\mathbf{r}), \nabla n(\mathbf{r}))$ needs to be constructed from the knowledge of some limiting cases. For instance, the case of the uniform charge distribution should be at least approximately recovered, i. e. $f(n(\mathbf{r}), 0)) \approxeq n(\mathbf{r}) \varepsilon_{\mathrm{XC}}^{\mathrm{Hom.}}(n(\mathbf{r}))$. Numerically $f(n(\mathbf{r}), \nabla n(\mathbf{r}))$ can then be constructed in the limit of slowly varying density by an expanding the exchange-correlation hole to a power series of second order, which should be cut off for long distances (cf. Eq. (2.23) and Eq. (2.24)) in order to mimic the behavior of the exact exchange-correlation hole. The actual breakthrough for the for the GGA was made by Perdew and Wang when finding an analytic expression satisfying the required criteria and to which is referred commonly since then as the PW91 functional [82]. A simplification of this functional involving only minor changes of lower significance has been published by Perdew *et al.* as the PBE functional, which is arguably one of the most if not the most widely applied flavor of the GGA [83]. The latter two functionals provide a substantially better description for atoms, molecules and solids with significant density inhomogeneities. Contrasting the LDA, GGAs do in most cases underestimate bond-strengths and overestimate in turn geometrical dimensions. However, by construction the GGAs can not comprise an accurate parameterization of the exchange part and provide simultaneously a good description in the limit of the nearly constant electron density [84].

The LDA and GGA are commonly referred to as "semi-local" exchange correlation functionals, because taking into account only density gradients renders the GGA being far from truly non-local. Since they are available in parameterized form, the evaluation of $E_{\mathrm{XC}}[n(\mathbf{r})]$ is quite convenient and adds practically no measurable further computational cost to calculations. Applying these two to the same system and comparing the results allows to estimate the reliability and the accuracy of the approximation for the exchange correlation.

2.5 Plane-wave basis set

So far we did not comment on the practical aspects when solving the Kohn-Sham equations. At first a reasonable basis spanning the Hilbert-space of the problem has to be selected. The best choice depends of course on the exact problem of interest. For isolated atom and molecules, analytically hydrogen-like basis-sets centered and the atomic nuclei are a common choice, because they are not too different from the actually targeted solution, which will eventually be represented as a linear combination of atomic orbitals (LCAO). A disadvantage of this choice is that such localized basis are not strictly orthogonal, when centered at different positions, leading to a superposition error that needs to be taken care of.

Consequently, non-localized basis sets, such as plane-waves spanning the entire Hilbert-space of the problem offer the most systematic representation of the electronic wave-functions, because

they are naturally orthogonal, complete and independent of the actual atomic geometry under consideration. Therefore, plane-waves are also especially suited for geometries exhibiting a high degree of periodicity such as solids, being considered as infinitely extended Bravais lattice one a primitive unit cell. The use of pure plane-waves implies the strict periodicity of the atomic arrangement contained in the super-cell, which is in turn the primitive unit-cell of an artificial Bravais lattice being defined uniquely by three linearly independent lattice vectors. For the case of strictly three-dimensional solids this super-cell be identified directly with the primitive cell of the crystal lattice. Aperiodic systems, such as defects in solids, surfaces or isolated molecules and atoms can be modeled by larger super-cells effectively suppressing possible unphysical interactions between the periodic replica. Further details of this approach can be found in the excellent review by Payne *et al.* [75].

According to the Bloch's theorem we may express the wave-function ψ a single electron in the infinitely extended lattice of the periodically repeated atomic arrangement in the super-cell as product of phase factor and a part being of same periodicity as the entire lattice [85]:

$$\psi_{j,\mathbf{k}}(\mathbf{r}) = u_{j,\mathbf{k}}(\mathbf{r})\, e^{i\mathbf{kr}} \qquad \text{with} \quad u_{j,\mathbf{k}}(\mathbf{r}) = \sum_{\mathbf{G}} A_j(\mathbf{G}+\mathbf{k})\, e^{(i\mathbf{Gr})} \quad , \tag{2.29}$$

where $u_j(\mathbf{r})$ is a function with exactly the same periodicity as the entire lattice, which can also be expressed as the Fourier series expanded in reciprocal lattice vectors $\mathbf{G}$. The reciprocal lattice vector $\mathbf{k}$ is defined only within the Brillouins-zone of the super-cell and j enumerates the single particle wave function. If the Fourier coefficients $A_j(\mathbf{G})$ are known, the electronic wave-functions are obtained by a discrete Fourier transform:

$$\psi_{j,\mathbf{k}}(\mathbf{r}) = \sum_{\mathbf{G}} A_j(\mathbf{k}+\mathbf{G}) \exp\left(i\,(\mathbf{k}+\mathbf{G})\mathbf{r}\right) \quad . \tag{2.30}$$

An analogous transform of the effective potential

$$V_{\mathrm{Eff}}(\mathbf{r}) = \sum_{\mathbf{G}} \tilde{V}_{\mathrm{Eff}}(\mathbf{G})\, e^{i\mathbf{Gr}} \quad , \tag{2.31}$$

can be used to formulate the Kohn-Sham equations in Eq. (2.20) in reciprocal space:

$$\sum_{\mathbf{G}'} \left[\left(\frac{1}{2}(\mathbf{k}+\mathbf{G})^2 - \varepsilon_j \right) \delta_{\mathbf{G}\mathbf{G}'} + \tilde{V}_{\mathrm{Eff}}(\mathbf{G}'-\mathbf{G}) \right] A_j(\mathbf{k}+\mathbf{G}') = 0 \quad . \tag{2.32}$$

Solving this equation numerically exact for infinitely many Fourier components requires to extend the summation over the entire infinite reciprocal lattice, which poses at least substantial technical obstacles. On the other, an infinite summation is not necessary to describe the relevant physics, because extreme large reciprocal lattice vectors correspond to extremely large momenta of the electrons. Because we are focusing on the ground-state anyway in which extremely fast electrons travelling through the super-cell lattice are excluded by construction, the upper bound of all occurring momenta is set by Heisenberg's uncertainty relation. with the inner shell electrons being tightly concentrated in the vicinity to the atomic nuclei. Therefore the number of terms in Eq. (2.32) necessary to describe the essential physics depends on the largest atomic

number of any species in the system under investigation. On the other hand, by definition the reciprocal vectors depend on the size of the super-cell and therefore it is much more convenient to truncate the series for maximum kinetic energy, which is called the cut-off energy

$$E_{\mathrm{Cut}} \leq \frac{1}{2}(\mathbf{k}+\mathbf{G})^2 \quad , \tag{2.33}$$

and which is a technical parameter set before the actual calculation starts. This determines then the maximal reciprocal lattice vector in the summation in Eq. (2.32). This illustrates again the power of plane-waves as basis functions, because increasing E_{Cut} improves systematically the numerical quality of the resulting electronic wave-functions and energetics. However, apart from excitation in X-ray spectroscopy, the inner shell electrons play only a minor role in the overwhelming number of studies in chemistry and solid state physics interesting formation and breaking of chemical bonds. Therefore, replacing the ionic potentials and the inner core electrons with so-called pseudo-potentials lets us reduce the number summands in the series of Eq. (2.32) even further without substantial loss of information.

Before going into detail on that, we introduce at first another purely numerical simplification. The Kohn-Sham equations have to be solved formally at every point in the Brillouins-zone reflecting the fact that the infinite array of super-cell contains infinitely many electrons. This is not acceptable for human with a finite lifetime and therefore, one has to pick a number of **k**-points in the Brillouins-zone being used to form a sum, which approximates eventually integrals as for instance for the charge density:

$$n(\mathbf{r}) = \sum_j \int_{\mathrm{BZ}} \mathrm{d}k^3 \psi^*_{j,\mathbf{k}}(\mathbf{r})\psi_{j,\mathbf{k}}(\mathbf{r}) = \frac{1}{\Omega}\sum_j \sum_{\{\mathbf{k}\}} \sum_{\mathbf{G}} f(\mathbf{k})|A(\mathbf{k}+\mathbf{G})|^2 \quad , \tag{2.34}$$

where Ω stands for the volume of the super-cell. The problem is now to chose a set of **k**-points each being associated with a certain weight $f(\mathbf{k})$ to ensure that the summation indeed approximates the integral well. In the special but frequently occurring case that the corresponding real-space variable can be represented as a real number, the same function transformed to reciprocal space obeys also some simple symmetries with respect to the center of the Brillouins-zone, even if the function is non-symmetric in real-space and which lets us omit immediately some regions on the Brillouins-zone from the explicit summation. If the function is in real-space invariant under certain symmetry operations, the actual necessary integration and summation area in reciprocal-space shrinks even further to the so-called irreducible wedge. Only from this wedge one has to pick **k**-points for performing the sum in Eq. (2.34) and the final result is multiplied accordingly. The acceleration of the computation is being paid by introducing a dependence of the total energy $E[n(\mathbf{r})]$ on the actually employed **k**-point-set. This can be in principle surmounted by the scheme introduced by Monkhorst and Pack, which picks the **k**-points in a way that the integral is the better approximated the larger the **k**-point-set is [86]. The **k**-point-set itself can therefore be considered as a purely technical parameter similar as the plane-wave cut-off energy E_{Cut}.

2.6 Pseudo-potential approximation

The idea of using weak pseudo-potentials and a reduced number of electrons in the system instead of strong full atomic potentials and the full number of electrons exists for quite some time [87, 88, 89]. This is seamlessly integrated in the Kohn-Sham equations simply by replacing the external potential in Eq. (2.15) with the pseudo-potential $V_{\mathrm{Pseudo}}(\mathbf{r})$, which is a superposition of the individual, non-overlapping atomic pseudo-potentials $w_i(\mathbf{r})$

$$V_{\mathrm{Pseudo}}(\mathbf{r}) = \sum_I w_I(\mathbf{r} - \mathbf{R}_I) \quad , \tag{2.35}$$

where $\mathbf{R}_I$ denotes as before the coordinates of the Ith atom. Each atomic pseudo-potential has a certain radius r_{Cut} within which the number of oscillations of the electronics wave-functions should be reduced, because these oscillations can be captured only with high-energy short-wave length contributions of the plane-wave expansions. It is understood that beyond their specific radius r_{Cut} the atomic pseudo-potential should produce wave-functions being identical to their full, all-electron counterparts. It is understood that these two regions need to be connected smoothly, because discontinuities will necessarily require again larger basis sets. Because the self-consistent solution of the Kohn-Sham requires an accurate electron density in the entire super-cell, the charge density produced by the electronic pseudo wave-function within r_{Cut} should therefore also not deviate from the case of the full atomic potential. Pseudo-potentials satisfying these criteria are called "norm-conserving" and have been developed since the 1970's [90, 91, 92, 93, 94, 95]. They have the great advantage of being "transferable" meaning that these pseudo-potentials are capable to describe the valence electrons of the respective atomic species irrespective of the specific environment, which is highly desirable from a methodological point of view. A pseudo-potential becomes "more transferable" the smaller r_{Cut} is, which has to be paid in turn with increased basis sets in the actual calculation. In addition, we mention that so-called local pseudo-potentials depending only on the distance to the respective nuclei do not guarantee unrestrictedly the exact scattering behavior, making it necessary to define then the consequently termed non-local pseudo-potentials, which operate individually on each component of the angular momentum of the electrons.

However, despite their great improvements, norm-conserving pseudo-potentials still require basis-sets prohibitively large for the calculation of extended system comprising some hundred atoms. For this reason we applied within this thesis only Vanderbilt's ultra-soft pseudo-potentials, allowing to reduce the number of plane-waves even further [96, 97]. The essential trick here is to relax the requirement of norm-conservation, thus in the ultra-soft formalism the wave-functions alone do not reproduce the physical charge-density within r_{Cut}, i. e. in the close proximity to the atomic nuclei. The difference between the exact charge density and the pseudo-charge density are called augmentation charge functions $Q^I_{nm}(\mathbf{r})$ and are centered at the Ith atom and strictly confined to within a sphere of r_{Cut}:

$$Q^I_{nm}(\mathbf{r}) = |\varphi_n(\mathbf{r} - \mathbf{R}_I)|^2 - |\phi_n(\mathbf{r} - \mathbf{R}_I)|^2 \qquad \text{and} \quad q^I_{nm} = \int\limits_{|\mathbf{r}| \leq r_{\mathrm{Cut}}} Q^I_{nm}(\mathbf{r}) \mathrm{d}r^3 \quad , \tag{2.36}$$

where $\varphi_n(\mathbf{r})$ stands here for the Kohn-Sham orbital obtained from an all-electron calculation,

whereas $\phi_n(\mathbf{r})$ symbolizes the same orbital with the ultra-soft potential applied instead. The ultra-soft potential is then written as a composite of the a local and a non-local part:

$$w_I^{\mathrm{UPS}} = w_I^{\mathrm{Loc}}(r) + \sum_{nm} D_{nm}^I \left|\beta_n^I\right\rangle \left\langle\beta_m^I\right| \quad . \tag{2.37}$$

Making use of the bracket notion, $\left|\beta_m^{\mathrm{I}}\right\rangle$ denote angular momentum eigen-functions, i. e. essentially spherical harmonics centered at the Ith ion times a radial part letting them vanish beyond r_{Cut}. These and the coefficients of the matrix D_{nm}^I have to be determined for each atomic species specifically. Since the solution of the all-electron Kohn-Sham equation serves as a reference, one needs to do this specifically for each applied approximation of the exchange-correlation in the effective potential. A detailed description of the procedure how to do this practically can be found in the paper by Laasonen *et al.* [97] and we continue with the implications of the scheme. The physical electronic charge density is then decomposed into a "soft" part proportional to the pseudo wave-function $\phi($**r** and a "hard" part localized in the proximity of the atomic cores:

$$n(\mathbf{r}) = \sum_i \left[|\phi_i(\mathbf{r})|^2 + \sum_I \sum_{nm} Q_{nm}^I(\mathbf{r}) \left\langle\phi_i\right| \left.\beta_n^I\right\rangle \left\langle\beta_m^I\right| \left.\phi_i\right\rangle \right] \quad . \tag{2.38}$$

Consequently, the entire calculation has now been decomposed into a part of the atomic core regions and the region of the valence electrons, whose wave-function can be described using only very few short-wave-length components. In turn, much computational effort is saved when sparing the update of the augmentation charges after each SCF-cycle, which is strictly speaking another approximation. The effective potential in the Kohn-Sham equations written in Eq. (2.20) has now been extended with non-local part in Eq. (2.37), complicating the solving algorithm of the Kohn-Sham equations and sacrifices the strict orthogonality of the pseudo-wave functions. We have to be content with

$$\left\langle\phi_i\right| \hat{S} \left|\phi_j\right\rangle = \delta_{ij} \qquad \text{with} \quad \hat{S} = 1 + \sum_I \sum_{mn} q_{nm}^I \left|\beta_n^I\right\rangle \left\langle\beta_m^I\right| \quad , \tag{2.39}$$

defining the hermitian overlap operator or matrix $\hat{S}$. Despite of these complications, within this thesis only ultra-soft potentials have been applied in production calculations, because the substantially decreased number of plane-waves outweighs clearly the disadvantages.

A general drawback of the appliance of pseudo-potentials is the resulting arbitrariness of the total ground-state energy. The removal of the inner-cores makes $E[n(\mathbf{r})]$ also depend on the actual employed flavor of pseudo-potential. Moreover, how many inner-shell electrons are incorporated depends on nothing but the user's reasoning and resources, thus the computed total energies themselves have to be considered as absolutely arbitrary. When interested only in relative energies due to formation and breaking of chemical bonds, this does not form an obstacle, in fact, it is even advantageous, because those energetic differences will be range typically from of 0.1 eV to not more than several eV. In an all-electron calculation total-energies are probably some thousand or ten-thousand eV greater in magnitude, which requires then an accordingly higher relative numerical accuracy.

In the last two section we have introduced some approximations that are unlike the approxima-

tion exchange correlation not of fundamental nature. Artifacts that are only due to the numerics should of course be eliminated from the targeted results. This is best achieved if all total energies contributing to the actually interesting energy difference are computed used exactly the same pseudo-potentials and same set of technical parameters, in particular identical plane-wave cut-off energies and **k**-point-sets. Artifacts due to numerical noise can be avoided rather efficiently, in fact, this cancellation of errors allows very often to use smaller basis and smaller **k**-point-sets than the bare total energies would require.

2.7 Hellmann-Feynman forces

Up to now we have focused only on the total ground-state energy of a given atomic configuration. This covered the electronic subsystem by solving Eq. (2.20) for the set of given atomic species and their positions. The actual ground-state in turn would also require an additional optimization with respect these ionic positions, i. e. a geometry optimization. These geometry optimizations were the bulk actual calculation of this thesis and therefore we briefly comment on them.

Finding the atomic ground-configuration is synonymous to minimizing the forces on the atoms. These can be calculated by means of the Hellmann-Feynman theorem, which states that the derivative of the ground-state energy of any Hamiltonian H_λ with respect to a certain external parameter λ equals the ground-state expectation value of the derivative of the H_λ itself [98]. In a little less literally:

$$\begin{aligned}\frac{\partial E}{\partial \lambda} &= \frac{\partial}{\partial \lambda}\langle\Psi|H_\lambda|\Psi\rangle = \left\langle\frac{\partial\Psi}{\partial\lambda}\middle|H_\lambda|\Psi\right\rangle + \langle\Psi|\frac{\partial H_\lambda}{\partial\lambda}|\Psi\rangle + \langle\Psi|H_\lambda\left|\frac{\partial\Psi}{\partial\lambda}\right\rangle \\ &= \langle\Psi|\frac{\partial H_\lambda}{\partial\lambda}|\Psi\rangle \quad .\end{aligned} \tag{2.40}$$

Since the atomic coordinates R_I are precisely such external parameters, this last formula provides an useful recipe to calculate the ionic forces, which can then be used to optimize energy with respect to the atomic coordinates. In practice, the total force on the Ith atom can be separated a part due to the ion-ion and the ion-electron interactions:

$$\mathbf{F}_I = \mathbf{F}_I^{\text{Ion}} + \mathbf{F}_I^{\text{Elec}} \quad . \tag{2.41}$$

The ionic contribution can be obtained by direct differentiation with respect to the ionic positions and for the electronic part the Hellmann-Feynman theorem applies. The Hamiltonian in Eq. (2.40) has to be understood and the Kohn-Sham Hamiltonian with already applied approximation for the exchange correlation rather than the exact many-body Hamiltonian in Eq. (2.2). However, due to the numerical approximations we introduced in last two sections, we can be almost certain that the obtained ground-state wave-function is flawed by purely numerical errors. In this case all three terms in the upper line of Eq. (2.40) remain and the reliability of resulting forces will be poor. This error can be subdivided again into a part due to the incompleteness of the basis-set and the error, which is introduced by a spurious alteration of the effective Kohn-Sham potential due to the subsequently iterated inaccurate electron density [99] in the self-consistency calculation. These two error contributions are especially vicious if the basis

functions depend on the coordinates of the ions, rendering in this case the numerical derivation of the total energy with respect to the ionic positions favorable [100, 75]. Contrariwise, if the Hilbert space spanned by the basis is independent of the ionic positions such as for instance plane waves, both sources of error vanish exactly and the Hellmann-Feynman theorem can be applied unrestrictedly [99]. This is even the case for not fully converged plane-wave basis sets and thus the numerical error of the ionic forces is determined predominantly by the noise of the coefficients in the Fourier expansion of the Kohn-Sham wave-functions. Therefore, after having obtained the Fourier coefficients $A_j(\mathbf{k}+\mathbf{G})$ in Eq. (2.30), the forces on each ion in the super-cell can be calculated directly without making explicit displacements of the atoms necessary.

With the atomic forces at hand, numerous methods can be employed to optimize the atomic positions and to find consequently the relevant ground-state configuration. In this work we used the Broyden-Fletcher-Goldfarb-Shanno (BFGS) algorithm for this purpose [101].

2.8 Technicalities and extensions

Within this thesis all essential electronic ground-state calculations have been performed using the CASTEP-code [102], which implements the introduced methodology in a very efficient way. There exist many more algorithms for the solution of the Kohn-Sham equations than the direct diagonalization of Eq. (2.32). A direct diagonalization is unfavorable because decent basis sets comprise frequently $10^4 - 10^5$ plane-waves and the diagonalization of $10^4 \times 10^4$ or larger matrices poses technical problems and limits effectively the size number of Kohn-Sham- orbitals and thus the number of atoms in the super-cell.

Alternatively, minimizing directly the ground-state energy in Eq. (2.16) with respect to the wave-functions using conjugate gradient methods is a promising approach [75]. This is much more efficient because the N eigen-states of the N lowest eigen-energies of the Kohn-Sham Hamiltonian in Eq. (2.20) are calculated directly whereas the diagonalization of a $10^4 \times 10^4$ matrix computes all 10^4 wave-functions, of which the largest part is unoccupied and therefore irrelevant. However, this scheme becomes unstable for metallic systems, because many of the occupied highest states lie at the Fermi-level and it is hard to identify, which of the computed wave-functions contributes to the density and which does not. These instabilities are surmounted by introducing an artificial temperature to the electronic subsystem and permitting fractional occupation numbers of the electronic wave-functions [103]. This is being paid with the appearance of an entropy contribution to the total energy, which needs to be taken care of after self-consistency is achieved. Another problem is then the additional dependency of the Kohn-Sham energy, the Kohn-Sham wave-functions and hence the density with the Kohn-Sham-Hamiltonian itself on these occupation numbers. In principle, with sufficiently many internal updates of the wave-functions, the density and the Hamiltonian the variational principle may be maintained, i. e. with each SCF-cycle the total energy decreases further [104]. In principle, this method can be accelerated by omitting many of these costly updates, which leads then to a certain discrepancy between the internally used wave-functions and the used density. When approach self-consistency, this discrepancy should become immaterial, of course. However, this trick being essential for the speed-up of the algorithm reintroduces possible instabilities, which can be remedied in turn by mixing the current electron density in a smart way with the densities

obtained in previous SCF-cycles. This procedure is non-variational, which means that the total energy can also be approached from below, possibly after oscillating for some SCF-cycles and is therefore also potentially unstable. In spite of these problems, different flavors of the last algorithm turn out to be the fastest way to achieve self-consistency of the electronic density, even for non-metallic system. Within this thesis only the latter "density-mixing" method was employed and we refer the reader for further details to the paper of Kresse *et al.* [105] and the references therein.

Having now outlined the DFT-formalism as the methodology for the treatment of electronic structure, we shall comment here on its weaknesses and possible extensions before turning to the actual scope of this thesis. The major drawback of the DFT-formalism is certainly the missing of the truly universal exact exchange-correlation functional. The presented semi-local approaches offer a very good balance between computational cost and accuracy with respect to nature, however there have been attempts to extend. The so-called meta-GGAs incorporate not only gradients of the density but also second derivatives of the density and thus they include terms proportional to the kinetic energy [106, 107]. This leads then to a further complication when constructing the Kohn-Sham effective potential, because this depends then on the specific Kohn-Sham orbitals, leading to the formulation of the optimized effective potential (OEP) formalism [108].

Truly non-local approximations for the exchange-correlation were already formulated by Gunnarson *et al.* in 1979 [109], but due to their increased computational cost it was used only sporadically and it became only recently a serious alternative to the semi-local approach for extended system [110]. The complication arises here due to the splitting of the exchange correlation potential into three parts which are designed to fulfill in combination of the known properties of the true exchange-correlation functional, similar to those in Eq. (2.23). With more powerful computers available, this approach might possibly become applied more frequently for real system's of interest.

Steps into another direction were taken by Becke [111], who proposed to calculate the exchange correlation energy as a weighted sum of the exact Hartree-Fock exchange and the LDA exchange-correlation energy. Several flavors of such "hybrid functional" mixing schemes exist, which differ only in the weights in the sum of the differently approximated exchange-correlation contributions. These weights are chosen either a priori [112] or they have been determined by fitting the results to experimental observations [113]. To some extent this approach can be justified rigorously [114], however, the evaluation of the Slater-determinants is prohibitively costly for large plane-wave sets. On the other hand, localized basis functions require typically smaller basis sets and are therefore much more convenient for hybrid functional calculations.

The last approach corrects in many cases also for the electronic band-gap being severely underestimated by DFT with the standard semi-local functionals applied. For instance, the band gap of silicon, which has been the example material of DFT, is underestimated about 50% by the LDA with respect to experiment and for germanium the same functional does not find a band gap at all letting this semiconductor appear to be a metal [115]. However, it is not clear if this correction due to the mixing of the exact exchange semi-local exchange correlation reflects a real physics or if its just coincidence based on the fact in traditional Hartree-Fock approximation, the electronic band gap is usually overestimated [108]. In addition, it is also not quite clear if pure ground-state theory is able to calculate reliably physical quantities inherently derived from elec-

tronic excitations even if the universally true, universal exchange correlation functional would be known and applicable [108]. On the other hand, the excited states that would be derived from an exact solution of the Schrödinger equation with the Hamiltonian in Eq. (2.2). Therefore, the calculated excited state within DFT can be viewed from the standpoint of a perturbation theory consideration as the approximation of the zeroth order of the electron excitation energies [116].

In fact, reliable band gaps can only be obtained rigorously by using many-body techniques beyond the DFT-formalism, for instance within GW-approximation [62, 117] or the within the couple-cluster method [60]. These techniques are still being far away from applicable for system of interest, which motivated Animosivs *et al.*'s Ansatz in order to mimic a realistic band gap within a semi-local DFT calculation [118, 119]. The idea is to add a Hubbard like repulsion energy U to the effective Kohn-Sham potential for some specific atomic orbitals. This can be also quite helpful when treating transition metals with half-filled d- or f-bands of strongly correlated electrons and it restores at least partly the true exchange correlation functional with its discontinuities in the energy derivative with respect to number of electrons [120]. In practice, one may adjust the "wrong" DFT band gap simply by increasing the U-parameter accordingly. This introduces obviously some arbitrariness into the formalism, despite the fact that the are recent efforts being made to motivate the value of U from higher-level theories [121].

Although the list of advances and recent development in the field could easily be extended we stop we for the sake brevity and turn to the application of the formalism to $SrTiO_3$.

3 Properties of $SrTiO_3$

This chapter introduces the basic characteristics of the of $SrTiO_3$ as well as its (001) surface which will be the relevant one for this work. For the sake of brevity, we restrict ourselves to mention only the different phenomena, detailed information should be taken from the quoted references. Recalculating some of those properties will also serve to explain some practical aspects of the methodology and to verify our approach of modeling the surface of this material.

3.1 Bulk properties

Strontium titanate is a representative of the ternary perovskites with the general form ABO_3, in which A stands for a mono- or divalent metal atom and B for a tetra- or pentavalent metal atom. At room temperature it assumes the cubic ideal perovskite structure with $Pm\bar{3}m$ symmetry and has a lattice constant of 3.905 Å [122]. As schematically illustrated in Figure 3.1 it may be viewed either as a stack of alternating SrO and TiO_2 layers or as an array of TiO_6 octahedra in a cubic arrangement being linked together at the apices by sharing the oxygen atoms. The strontium atoms occupy then the spaces in between the octahedra. The latter picture of the structure is particularly suited when visualizing the low-temperature structure phases of $SrTiO_3$ but also of the entire perosvkite family. Upon lowering the temperature down to 105 K - 110 K, neighboring oxygen octahedra tilt against each other and break thereby the crystal's symmetry from cubic to tetragonal, which leads eventually to an approximate doubling of the unit cell vectors [123, 124, 125, 126, 127]. This converse rotation manifests one of the simplest conceivable and therefore most intensively studied examples of a second-order displacive structure phase transitions, whose investigation in theory as well in experiment has contributed a lot to the concept of "soft-phonons", which in turn play an essential role in structure phase transitions in general [128]. Because this transition at 105 K does clearly not lead to an electric dipole in the material and because it is not anti-ferroelectric it is called anti-ferrodistortive, emphasizing that it is a pure modification of the structure reducing the crystal symmetry [11]. Lowering the temperature further results in additional distorted crystal phases or elastic anomalies at 65 K [129] and 35 K [130], however, even at 0 K a true ferroelectric state is never achieved, because of quantum fluctuations due to the relatively low mass of strontium [131]. Therefore, pure $SrTiO_3$ is like for instance $KTaO_3$ a so-called incipient ferroelectric, and can be brought intriguingly into a true ferroelectric state by manipulating the crystal lattice by means of chemical [132] or isotopic substitution [133] or the appliance of epitaxial stress [134, 135, 136] or mechanic stress [137]. It is interesting to note that replacing strontium with lead or barium yields $PbTiO_3$ or $BaTiO_3$, respectively, two materials having a similar lattice constant in the cubic phase and essentially the same electronic structure like $SrTiO_3$, but which are known to assume ferroelectric phases at room temperature [11, 138, 139]. This illustrates that many physically interesting and techni-

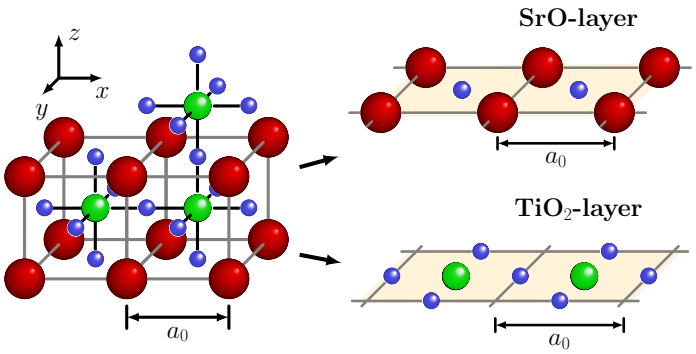

Figure 3.1: Schematic illustration of the bulk structure of $SrTiO_3$ in the undistorted $Pm\bar{3}m$ phase. Color code for this and all consecutive figures: big red (dark) spheres: strontium, big green (bright) spheres: titanium, small blue (bright) spheres: oxygen.

cally potentially important properties of the individual representatives of the perovskite family depend crucially on the ratio of the size and mass of the constituents and which then leads to a very complex interplay of the electronic and crystal structure. This is of course highly material specific and for the sake of brevity we direct the interested reader for further information about the particularities of different perovskite materials to the list compiled by Lines and Glass in their excellent textbook [11].

The temperature dependence of the structure of $SrTiO_3$ lets us face a dilemma. The water and oxygen adsorption on $SrTiO_3$ we want to address with this work take place at elevated temperatures certainly above 110 K, letting us consider $SrTiO_3$ always its the ideal cubic perovskite structure. On the other hand electronic structure calculations are carried out formally at 0 K, which means that we deal with a constraint system being not exactly in its ground state. However, because relevant energetics are always being derived with respect to a reference system, for example the bulk structure or the absorbent-free surface, we have good hope that errors due to the strictly speaking incorrect structure cancel to large extent. On the other hand, for bond lengths calculated within our model of $SrTiO_3$ we have to accept presumably a large error-bar.

3.1.1 Model of bulk $SrTiO_3$

The first step before starting a pseudo-potential DFT calculation is to generate or to pick the respective pseudo-potentials for the different atomic species. This should offer a balance between accuracy and "softness", i. e. the fast convergence of the atomic properties with respect to the size of the basis set. Within this thesis we employed almost exclusively ultra-soft pseudo-potentials from the CASTEP's pseudo-potential library. It is understood, that for each different employed approximation for the electronic exchange correlation a specifically generated pseudo-potential for the respective species was used. Concerning the results presented in this thesis the electronic configuration modeled by the exchange correlation specific pseudo-potentials was the always same, namely $2s^2 2p^4$ for the oxygen, $3s^2 3p^6 4s^2 3d^2$ for the titanium $4s^2 4p^6 5s^2$ for the strontium and unsurprisingly $1s$ for the hydrogen atom. The tests shown in this chapter as well as the results presented in Appendix A and Appendix B may serve as a verification of the reliability of

the employed pseudo-potentials.

Before re-calculating some properties of the material in order to compare to experiment and further published theory data, we have to ensure that the numerical accuracy is guaranteed. This is first and foremost controlled by two quantities: the number plane waves in the used basis set and the number of integration points in Brillouins-zone. These two parameters have to be appropriately in order to provide of course accurate energies and forces, but also and to keep calculations still feasible. As a basic observable we used the formation energy of bulk $SrTiO_3$ at 0 K defined as:

$$E^{\text{Form}}_{\text{SrTiO}_3} = E^{\text{Bulk}}_{\text{SrTiO}_3} - E_{\text{Sr}} - E_{\text{Ti}} - \frac{3}{2}E^{\text{Gas}}_{\text{O}_2} \quad . \tag{3.1}$$

The convergence of this energy with respect to the numerical parameters is shown in Figure 3.2, where for the total energies of $SrTiO_3$, Sr, Ti and the gas phase oxygen molecule on the left hand side of Eq. (3.1) the experimental geometries were used. The calculated data proves indeed that $(8\times8\times8)$-**k**-points and a plane wave basis of 430 eV are well sufficient to ensure a numerical quality of better than ±10 meV of $E^{\text{Form}}_{\text{SrTiO}_3}$ for both functionals, i. e. no substantial improvement of the description of chemical bonding can be expected for using denser **k**-point-meshes or more plane-waves. Clearly, the experimental structures serve only as a first guess and the actual production calculation have to be carried out with the numerically determined lattice constants and bond lengths. These theoretical equilibrium geometries depend on the employed functional and pseudo-potentials, but also on the numerical accuracy of the employed basis set. While the first two of these dependencies can never be really surmounted, the latter should be eliminated. Figure 3.3 shows for the LDA and the PBE functional the lattice constants and the bulk modulus of $SrTiO_3$ as well as the force exerted on one oxygen atom in an oxygen molecule with the experimental oxygen-oxygen bond length. The first two quantities are obtained simply by calculating the total energy of $SrTiO_3$ upon variation of the lattice parameter and fitting the resulting data to the formula of Birch and Murnaghan [140, 141], while the third is taken from the directly from the CASTEP output files as obtained for plotting Figure 3.2. The motivation to monitor these properties is that the lattice constant, the force and the bulk modulus depend on the total energy as well as on its first and second derivative with respect to geometrical parameters. Thus having these quantities numerically converged lends credence to the computed atomic arrangements as well as the resulting energetics.

We ascertain constancy of the lattice constant and the bulk modulus with a range of 2% for a plane wave basis cut-off energy of 380 eV or greater. However, for the PBE-functional, the force on the oxygen molecule is more sensitive with respect to the plane wave basis and requires therefore a slightly increased number of plane waves. Since the bulk of our production calculations in Chapter 4, Chapter 5 and Chapter 6 are geometry optimization requiring reliable forces, all essential calculations reported in this work have been carried out using a plane wave set of corresponding to exactly 430 eV appearing to be a good compromise between numerical accuracy and computational cost.

In Table 3.1 we compare our results to some values reported in previous publications and we find very good agreement for the LDA- as well as the PBE-functional. However, we note that hybrid functionals, such as the HSE- or B3PW-functional [142, 33] seem to give much better agreement with the experiment for the price of increased computational costs. In Appendix A

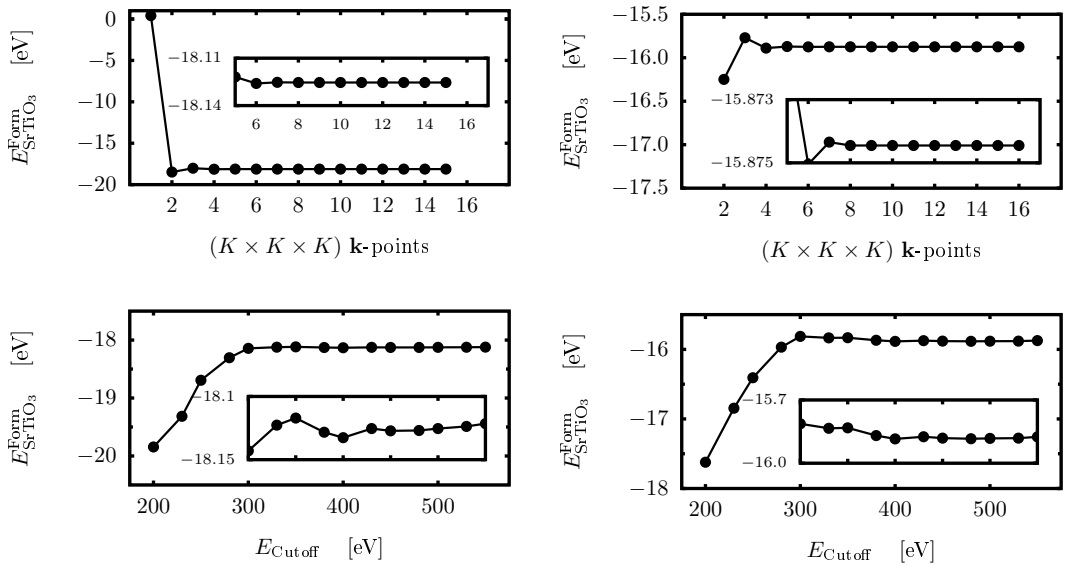

Figure 3.2: Formation energy of bulk $SrTiO_3$ as a function of the **k**-points and the plane-wave basis cutoff energy for the LDA (left side) and PBE (right side) xc functional. For this plot, for $SrTiO_3$, Sr and Ti the experimental lattice constants and for the gas phase oxygen the experimental oxygen-oxygen bond length was used. The insets show the same respective data on a smaller scale. For the energies in the upper panel a plane wave basis corresponding to 430 eV was used, whereas the data in the lower ones was obtained using $(8 \times 8 \times 8)$-**k**-points.

and Appendix B we report the theoretically optimized geometries and energetics of the further species on the right hand side of Eq. 3.1.

3.1.2 Electronic Structure

Pure $SrTiO_3$ is transparent with a high refractive index ranging from 2.3 - 2.5 for visible light at room temperature [146], which was exploited in its historically first major application as a substitute for gem stones in jewelry [16]. At room temperature it has a dielectric constant of approximately 330, which qualifies it for applications in high voltage capacitors, most importantly as a substitute for SiO_2 in CMOS-devices. Upon lowering the temperature the dielectric constant rises proportional to the reciprocal temperature to reach finally its saturation value of approximately 18 000 at 1.4 K [147], albeit it may decrease again on the appliance of large static electric fields [148]. Moreover, below the 110 K phase transition, the dielectric constant unveils its actual tensor-character in mono-domain $SrTiO_3$ samples [129]. In addition we remark, strong electric fields also seem to introduce a lattice distortions, in the cubic high temperature phase illustrating once again the interplay of the electronic and the crystal structure [149].

Doping with different species or oxygen-reducing of $SrTiO_3$ allows to tune this material from an *n*-type to a *p*-type semi-conducting behavior [150, 151, 152], it may exhibit proton conductivity [153, 154] and leads at lowest temperatures below 0.5 K to super-conductance [155, 156, 157]. This temperature dependence of many properties of $SrTiO_3$ shows again, that much of the relevant and interesting physics of $SrTiO_3$ can not be obtained simply by straightforwardly

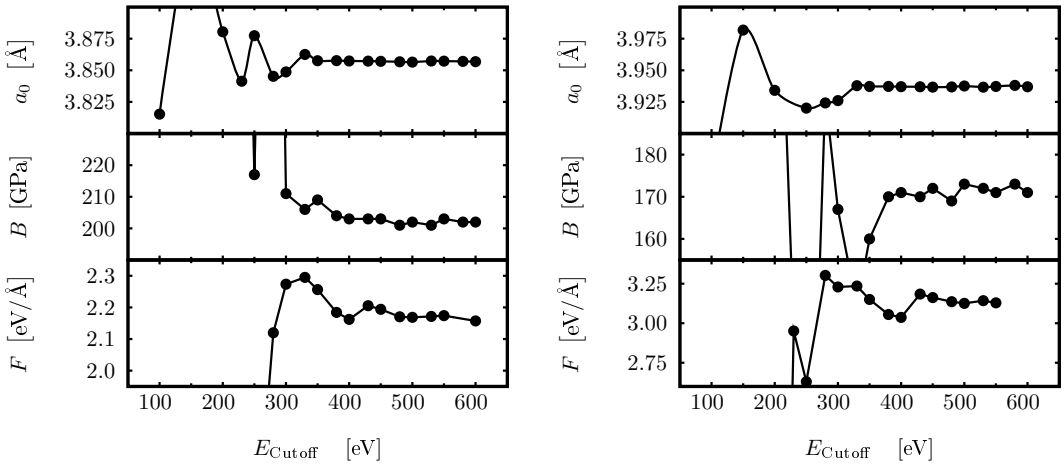

Figure 3.3: Lattice constant a_0 and bulk modulus B and the force exerted on one oxygen atom of oxygen molecule with the experimental bond length of 1.20 Å as function of the plane-wave basis set for the LDA (left side) and the PBE (right side) xc-functional.

Table 3.1: Comparison of our calculated lattice constant and bulk modulus of $SrTiO_3$ to data found in literature.

			a_0 [Å]	B [GPa]
This work	LDA		3.857	202
	PBE		3.938	170
Theory	LDA	[143]	3.865	
	LDA	[32]	3.85	200
	LDA	[144]	3.87	194
	PBE	[142]	3.943	
	PBE	[138]	3.94	169
	HSE	[142]	3.904	
	B3PW	[33]	3.903	
Exp.		[145]	3.905	184

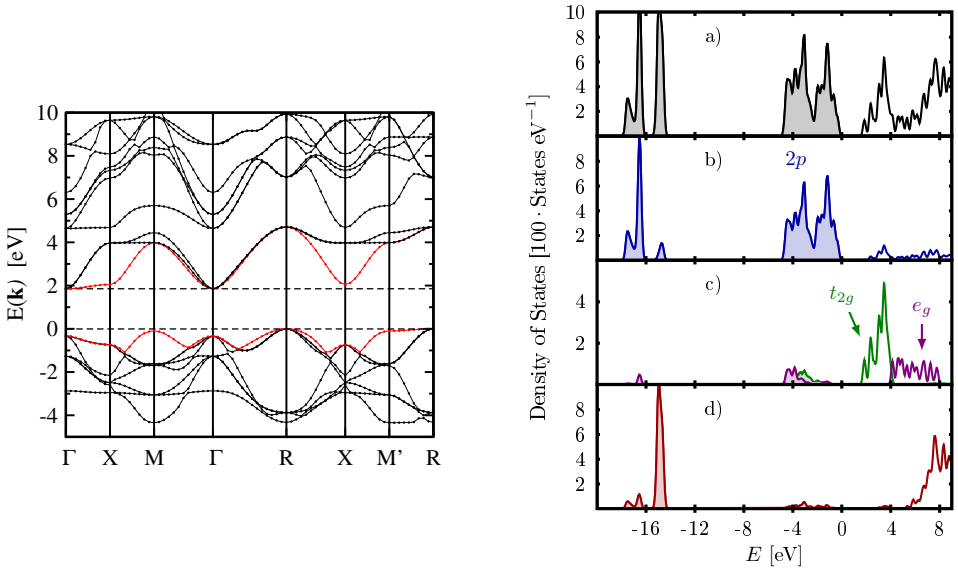

Figure 3.4: Left: Electronic band structure of bulk $SrTiO_3$ calculated in LDA. The topmost states in valence band serving also energetic reference as well as the bottommost in the conduction band are highlighted in red color. Right: Electronic density of states (DOS) of bulk $SrTiO_3$. The (empty) filled curves denote the (un-)occupied states. Panel (a) shows the total DOS, panel (b), (c) and (d) the individual projection on the oxygen, titanium and strontium atoms, respectively.

running ground-state 0 K electronic structure calculations, and we therefore restrict ourselves to the simpler and more general properties.

In the most simplistic picture, $SrTiO_3$ is a purely ionic crystal in which the titanium and strontium atoms donate four and two electrons respectively to the three oxygen atoms in the unit cell. Thus, the two cations are positively charged Ti^{4+}- and Sr^{2+}-species, whereas each oxygen atoms takes up two electrons forming thereby a O^{2-}. This electronic configuration makes $SrTiO_3$ an insulator with an electronic band gap between 3.2 eV and 3.3 eV [146, 158], where the top of the valence band is formed by the O $2p$ electrons, while the bottom of the conduction band consists of the depopulated Ti $3d$ states. Thus, the electronic properties of this material are predominantly controlled by these electronic levels. In Figure 3.4 we present the calculated electronic band structure, which exhibits the principle features reported already in previous theoretical studies [159, 143, 160]. The severe underestimation of the electronic band gap is a trademark of the semi-local functionals and can be therefore expected. However, we note that Heifets *et al.*'s hybrid functional as well as Cappellini *et al.*'s "LDA+simplified *GW*" [161] approach overestimate the band gap with approximately the same error as the traditional LDA and PBE underestimate it and do therefore not provide a clear systematic improvement with respect to the experiment. In addition, we analyze the electronic density of states of $SrTiO_3$ in Figure 3.4 a little bit further. Obviously, the contributions of the strontium atoms to the total eigenvalue spectrum are to too far away from the valance band maximum or conduction band minimum and therefore the strontium atoms can be expected already at this point to play only

Table 3.2: Comparison of direct and the Γ point and minimal, indirect electronic band gaps calculated for different functionals and comparison to values reported in literature.

			$E_{\mathrm{Gap}}(\Gamma)$ [eV]	$E_{\mathrm{Gap}}(R-\Gamma)$ [eV]
This work	LDA		2.18	1.85
	PBE		2.57	2.15
Theory	LDA	[162]	2.22	1.89
	LDA	[161]	2.24	1.90
	LDA+*GW*	[161]	5.42	5.07
	B3PW	[160]	4.43	4.16
Exp.		[162]	3.75	3.25

an indirect role in the formation of chemical bonds on adsorbates on the surface and thus in particular for the growth. In panel (c) of Figure 3.4 on the right hand side, we also present the contribution of the symmetrically inequivalent 3*d* states of the titanium atoms. Typically for octahedral coordination is the splitting of *d*-orbitals into the two groups of e_g and t_{2g} symmetry, respectively [163]. The first ones are linear combinations of the atomic d_{z^2} and $d_{x^2+y^2}$ orbitals pointing directly to the ligands and rendering thereby respective bonding levels lower in energy than those t_{2g} states, which are formed in turn by the d_{xy}-, d_{xz}- and d_{yz}- atomic levels. For the anti-bonding and in $SrTiO_3$ unoccupied 3*d* orbitals, this energetic ordering reverses letting only the t_{2g}-states form the bottom of the conduction band. We note that this electronic structure is extremely similar to the one of TiO_2 [1], which is also responsible for the similar behavior these two materials in many respects [1].

Although it may be useful in some cases as an intuitive picture to rationalize certain phenomena involving charge rearrangements [164], closer inspection of Figure 3.4 casts doubts on the aforementioned simplistic image of the charge rearrangement and pure ionic bonding in $SrTiO_3$. The partial occupation of bonding 3*d* orbitals shows that there exists indeed some covalency in the chemical bonding of the crystal. In the following, we will therefore quantify the ionic charges using Hirshfeld- and the Mulliken charge portioning schemes [165, 166]. The Hirshfeld scheme relies only on a comparison of the electronic density of the composite structure and electronic density of the individual, neutral atoms. In contrast, the Mulliken scheme analyzes the projections of the individual contributions of the atomic wave-functions to the all-electron wave-function of the entire system. The numerical values of these two approaches can not be compared directly, however, in the trends they predict should be similar.

In Table 3.3 we list the Hirshfeld- and Mulliken charges of the oxygen-, titanium and strontium atoms in bulk $SrTiO_3$. Both charge partitioning schemes point at a charge separation between the SrO and TiO_2 planes, which constitute the bulk of $SrTiO_3$. The resulting dipole moment pointing from the TiO_2 to the neighboring SrO planes cancels effectively in the bulk, but it may have severe consequences at the surface. As pointed out already by Goniakowski and Noguera [167], this effective charging of the planes is only due to the partial covalency and symmetry of the

Table 3.3: Calculated Hirshfeld- (Q_H) and Mulliken charges (Q_M) of bulk of the three constituting species of $SrTiO_3$ for the LDA and PBE functional.

		O	Ti	Sr
Q_H $[e]$	LDA	-0.28	0.46	0.39
	PBE	-0.30	0.49	0.41
Q_M $[e]$	LDA	-0.71	0.80	1.32
	PBE	-0.74	0.85	1.38

oxygen-titanium bonds in the bulk.

3.2 Surface of $SrTiO_3$

Experimental studies addressing exclusively the surface of $SrTiO_3$ and its structure have been performed since the 1970's and still many open questions remain, which will be illustrated with only a few examples in the following paragraphs. The bulk of the experimental studies focused on the (001) surfaces, because it has the lowest surface formation energy and is considered to be non-polar on the basis of the purely ionic picture mentioned in the last section. As it can be seen already from Figure 3.1, the $SrTiO_3$(001) surface has two different possibilities for terminating the (001) surface, either with the SrO or the TiO_2 layer. Therefore many experimental studies were concerned with the important question of how to identify and prepare these two kinds of surfaces. In the following paragraphs we will try to illustrate the difficulties of understanding the $SrTiO_3$ surface by outline briefly the most important experimental studies on this issue. For a more detailed overview we refer the reader to the summery given by Deak and the references therein [168].

The experimental techniques used to study the $SrTiO_3$ are mostly standard in surface science and for an introduction to, for instance, ultra-violet photo-emission spectroscopy (UPS), X-ray photo-emission spectroscopy (XPS), low energy electron diffraction (LEED) of reflection high-energy electron diffraction (RHEED) we refer the reader to standard textbooks in surface physics or general experimental physics [169, 170]. Further non-standard techniques are introduced in detail by the cited publications or the references therein. However, because it will be important in Chapter 5 we will briefly comment about the surface imaging techniques with sub-nano-meter resolution, such as the atomic force microscopy (AFM), friction force microscopy (FFM) and scanning tunneling microscopy (STM). The STM was developed historically at first and acquires the topographic information about a surface by observing the tunneling current between a tip and surface a function of the lateral and vertical position of the tip on the sample [171]. This method probes therefore electronic states near the Fermi-level and is therefore not particularly well-suited for insulators such as non-doped, non-reduced pristine $SrTiO_3$. For these cases, the AFM is much more useful, because the surface morphology is here probed by measuring the electrostatic and van-der-Waals forces exerted on the tip. Since these force are directly correlated with the total charge density, mapping the deflection force on the tip-holding

cantilever provides information about the surface topology [172, 173]. Measuring in addition simultaneously but separately the torsion of the cantilever yields also information about the lateral forces, or "friction-forces" exerted on the tip, serving as an indicator for different chemical species on the surface [174, 175]. These and similar methods allow indeed an investigation of surface structures with the sub-nano-meter resolution in real space by moving an atomically sharp tip over the sample using the piezo-electric devices. For further questions referring to the details of this technique we refer the reader to Lüthi *et al.*'s paper [176].

Early studies using LEED report that simple fracturing of the sample yielded a (1×1)-pattern, whose brilliance was significantly improved upon oxygen annealing. Sharp LEED patterns indicated a good periodicity of the surface structure and in ultra-violet photo-emission (UPS) spectra a peak attributed to surface oxygen vacancies disappears [30]. In combination with Auger-electron spectroscopy (AES) the latter work found also evidence that Ar^+ sputtered and subsequently annealed surface would lead to a largely TiO_2 terminated sample. However, as Cord and Courths demonstrated, the sharpness as well as the periodicity of the observed LEED patterns depends on the time of the anneal and on the oxygen pressure, substantiating that the surface morphology depends $SrTiO_3$ crucially on the exact conditions in the environment [177]. This impression is further amplified, when comparing the experimental results using similar sample-treatments, but different measuring techniques. A widely applied surface preparation procedure was established by Kawasaki *et al.* who used buffered NH_4F-HF (BHF) solutions to etch selectively the capping SrO layers to finally obtain $SrTiO_3$ samples terminated exclusively with TiO_2 [178]. Such prepared samples where then used by Kido *et al.* and Nishimura *et al.* to study by means of the medium-energy ion scattering (MEIS) the effects of oxygen annealing on the surface structure [179, 180]. The basic observation is that the fraction of TiO_2 on the surface is reduced to to 88%, i. e. 12% of the surface is terminated with a SrO capping layer. Yoshimoto *et al.* studied the surface of similarly as-received and oxygen annealed $SrTiO_3$ samples using coaxial impact-collision ion scattering spectroscopy (CAICISS) and found in agreement with Kido *et al.* and Nishimura *et al.* that these are predominantly TiO_2 terminated. However upon homo-epitaxial growth, the entire surface of the samples were reported to have mostly SrO stoichiometry [181]. These two works are contrasted by the statement of van der Heide *et al.* mentioning that annealing the sample in oxygen may also in a predominantly SrO terminated sample [182]. On the other hand, annealing the sample in vacuum leads expectedly to the formation of oxygen vacancies by decreasing the oxygen content in the surface layer about 14% [179]. This process is accompanied by a simultaneous reduction of the fraction of the TiO_2 domains on the surface by 5% and results in a LEED pattern with 2×2-periodicity [180, 179], whereas van der Heide finds evidence of Ti-depletion in the topmost atomic layer [182].

The same issue was addressed by Naito and Sato using exclusively RHEED and thus concentrating thereby essentially on possible super-structures on the surface [183]. Polished, untreated samples were assumed to be predominantly TiO_2 terminated and exhibited (1×1) patterns indicating the absence of super-structures on the "terraced" (001) surface, whereas vacuum annealing resulting in a (2×1) reconstruction. Unfortunately, they report only very briefly on the actual surface stoichiometry, but they mention an earlier study also having observed a super-structure with the same periodicity on a SrO terminated sample. Subsequent oxygen annealing led then to the emergence of a two-domain $(\sqrt{13} \times \sqrt{13} - \mathrm{R}33.7^\circ)$ super-structure as well as a centered $\mathrm{c}(6 \times 2)$ structure. The latter was looked upon more closely by Jiang and Zegenhagen,

who found that this formation is extraordinary stable, even in ambient air and was reported to emerge only after a "combination of oxygen and UHV" anneals [184]. In a later study, Jiang and Zegenhagen revisited the subject and reported that not only the exact condition during but also before annealing in UHV influence the resulting surface morphology on the $SrTiO_3$ sample [51]. In addition, a $c(4\times2)$ reconstruction appears after the necessary annealing in hydrogen on the nominally TiO_2 terminated surface. After an additional anneal in oxygen, this formation was replaced with the aforementioned $c(6\times2)$, illustrating that the exact surface structure can hardly be controlled for the principle inevitable presence of hydrogen or aqueous species in relevant applications. Although also using atomic resolution STM and annealing in UHV, none of the latter two experiments reproduced explicitly the $\sqrt{5}\times\sqrt{5}-\mathrm{R}26.6^\circ$ and (2×2) structures reported by Tanaka *et al.* and Matsumoto *et al.* [185, 186]. Furthermore, Jiang and Zegenhagen criticize an early study of Liang and Bonnell, who have observed after annealing their $SrTiO_3$ samples in UHV in contrast to the aforementioned studies a "Sr-rich" surface with SrO-islands [25]. In addition, the authors imply with their suggested formation of Ruddlesden-Popper-phases drastic structural changes in the near-surface region [187, 188, 189]. These crystal phases can be viewed have the stoichiometry of $Sr_{n+1}Ti_nO_{3n+1}$ with the integer number n set to infinity recovering the cubic ideal peroskite structure and $n=0$ corresponds to pure SrO. In fact, the Ruddlesden-Popper phase can also be viewed as layered perovskite structures, emphasizing their close relationship to the cubic perovskite structure, but also to the crystal structures of the layer high-T_C super-conducting cuprates. These findings, however, are strongly supported by Szot and Speier, who observe by means of X-ray diffraction that their $SrTiO_3$ samples are capped by a surface layer of "chemical inhomogeneities" extending several tens of nano-meters into the bulk [26]. Furthermore, the authors find evidence that the "samples treated in the standard manner at elevated temperatures" are not in thermodynamic equilibrium, but the contact with the gas and gas mixtures in the ambient triggers the development of a "continuous chemical heterogeneity" from the surface into the bulk. It is also eye-catching, that authors of the last three experimental studies prefer to talk of "Sr-" or "Ti-rich" surfaces instead of "SrO" or "TiO_2 terminated" surfaces.

This nomenclature has also been adopted by Castell, when studying the development of nanostructured rows that appear on UHV annealing and Ar^+ sputtering on the $c(4\times2)$ reconstructed $SrTiO_3$ samples. However, these nano-rows transform to nano-dots upon extended annealing, implying that these formations are only meta-stable [190]. In another publication the same author presents his STM measurements of BHF etched Nb-doped $SrTiO_3$ samples that have been annealed in UHV, sputtered with Ar^+-ions and then again UHV. Apart from the characterization of many reconstructions, steps of only one lattice constant i. e. $\simeq 4$ Å are detected, substantiating the samples were terminated with only one "Ti-O-rich" layer [191]. The same reconstructions were studied by Erdman and Marks under oxidizing conditions and described them in stark contrast to Szot and Speier as "thermodynamically stable" [192]. In fact, the authors succeeded in reproducing the different reconstructions of TiO_2 stoichiometry and proposed already a temperature depended phase diagram.

Many of the aforementioned experimentally developed pictures of the $SrTiO_3$ surface morphology are inspired by the diffusion of oxygen vacancies or their interplay with an oxygen atmosphere, Kubo and Nozoye proposed a strontium ad-atom model for the $SrTiO_3$ surface physics. In particular they focused on the $(\sqrt{5}\times\sqrt{5}-\mathrm{R}26.6^\circ)$ reconstruction providing an

seemingly consistent picture, which was corroborated by DFT-calculations [27]. However, in a later, more refined DFT study the thermodynamic stability was challenged again from the theory side [193], and criticized by Vonk *et al.* who formulated in turn an unorthodox model of an oxygen ad-layer on the originally TiO_2 terminated surface, which was claimed to be consistent with the X-ray data [194]. On the other hand, the actual formation-mechanisms of such an oxygen over-layer are quite unclear if not counterintuitive and moreover, the results presented in Chapter 4 qualify this surface model as extremely unlikely to occur.

One of the most intensively discussed of all proposed structures on the $SrTiO_3$ surface is the (2×1) reconstruction proposed by Erdman *et al.*, which comprises double-layer of TiO_2 on the $SrTiO_3$ surface [28]. This surface formation has recently been re-confirmed by Herger *et al.* using x-ray diffraction [195, 196]. Making use of the octahedral picture of the $SrTiO_3$ structure, the unreconstructed (1×1) TiO_2 terminated surface may be viewed as an arrangement of halved oxygen TiO_6 units. The TiO_2 double-layer is then created by adding in every second surface unit cell another halved of those oxygen octahedra, sharing unlike in bulk $SrTiO_3$ not the apices, but the sides of the original lattice octahedra. This atomic arrangement results in a "zig-zag"-arrangement of the topmost Ti-atoms being the actual recognition feature of this structure. With this and the resulting remarkable protrusion of one oxygen atom, this structure contains some features reminiscent of the (110) surface of rutile [47], rendering it indeed quite plausible on Ti- and O-rich ambient conditions. However, two independent DFT-studies using the first-principle thermodynamics could not confirm a thermodynamic stability of this reconstruction [32, 33], even in the Ti-O-rich regime. Contrariwise, these two and the work of Liborio *et al.* showed that only the unreconstructed (1×1) surface of $SrTiO_3$ corresponds to the thermodynamic equilibrium. The double-layered structure as proposed by Erdman *et al.* would correspond then, strictly speaking only to meta-stable formations being "trapped". We will go into that in greater detail in Section 4.3, when introducing the formalism of first-principle thermodynamics with the example of the oxygen ad-atom on the $SrTiO_3$ surface.

Any attempt to consider all the experimentally proposed surface formations and reconstructions would leave us helplessly overcharged in our actually interesting subject of the oxygen and water adsorption $SrTiO_3$. On the other hand if the stoichiometry is not to different from that of bulk $SrTiO_3$, one would expect not essential and thus most likely differences smaller than the accuracy of the applied DFT method can provide. We concentrate in the following exclusively on the unreconstructed, defect-free SrO and TiO_2 terminations of $SrTiO_3$, to which we will also refer occasionally as the regular terminations. With these two being the only possible strictly thermodynamically stable surface terminations, we expect our results will contain some validity for surface structures being not too different from these regular terminations as well.

3.2.1 Model of the (001) surface

In principle, periodic boundary conditions are particularly suited for the treatment of practically infinitely continued structures. Aperiodic structures can be modelled only by embedding them into periodically continued super-cell, which should be sufficiently large to suppress interactions between the species. Therefore, one does actually not deal with a single representative, but an infinitely continued array of these aperiodic structures. For instance, when calculating single atoms or molecules as done in Appendix B, monitoring carefully the total energy with the size

of the super-cell ensures complete isolation of the specimen from their periodic artificial replica. Finally, the total energy of one of the representatives in the array should be exactly identical to the one calculated in strict isolation. For clean surfaces without adsorbed species, the periodicity is broken only in the z-direction, i. e. normal to the surface, whereas in the lateral x- and y-direction it is maintained. We model the surface therefore with a number of bulk unit cells piled up to a slab and insert then a region of empty space, i. e. vacuum into the super-cell. These bulk unit cells are dimensioned with the theoretical lattice constants listed in Table 3.1 in order to exclude any strain effects. This concept is nowadays standard and it is explained in detail in the comprehensive review by Payne *et al.* [75]. However, this adds now two additional convergence parameters necessary to observe, i. e. the thickness of the slab and the thickness of the vacuum space, because physically meaningful energetics should not depend on the particularities of the specially chosen surface model.

A further complication arises for the case of the surface of a $SrTiO_3$-sample, which we will consider from now on only as a stack of SrO and TiO_2 planes, which constitute also the two regular terminations of the $SrTiO_3(001)$ surface. However, in Section 3.1 we have seen that the electric charge density distributes differently between the two different types of layers, which would then result in an artificial dipole moment across the super-cell. We surmount this problem by imposing a strict symmetry with respect to the central plane of the symmetrically terminated slab of SrO and TiO_2 layers, which is then strictly speaking not exactly stoichiometric $SrTiO_3$. This mirror symmetry cancels the surface dipole exactly and provides in addition a well defined bulk limit in the center of the surface model, because the atoms in the three central atomic layers can now be kept fixed at their respective bulk positions in geometry optimizations. Admittedly, a bulk limit could also be achieved in the center of an asymmetrically terminated surface model slab, however, at a much increased computational cost. We mention that this approach of symmetrically terminated, and thus non-stoichiometric surface models has also been applied and tested with respect to the asymmetrically ones before for instance by Cheng *et al.* raising hopes that this is provides indeed a consistent and feasible model of the surface [197]. Such a periodically repeated surface model for the two terminations is exemplary illustrated in Figure 3.5. When dealing only with the adsorbate-free and unreconstructed surface it is in principle sufficient to construct the surface model slab by piling up one bulk unit cell of $SrTiO_3$. However, in the next chapters we will consider adsorbed species in the limit of isolation, which is characterized by vanishing interaction with their periodic replica in the lateral x- and y- directions. Consequently, we will have to construct our surface models using more than one stack of bulk unit cells $SrTiO_3$ attached to each other side by side.

Summarizing, we have in principle four numbers characterizing the surface model geometry, namely the vacuum space D_{Vac} measured by the surface-surface distance, the numbers of bulk unit cells N_x and N_y repeated in the lateral x- and y direction and the number of atomic layers, which is odd for symmetrically terminated surface model geometries. In the following we will call a model geometry with N_x and N_y bulk unit cells simply $(N_x \times N_y)$-surface model. Since we will consider only the unreconstructed $SrTiO_3(001)$-surface within this work, the danger of a possible confusion with reported reconstructions is safely excluded. On the other hand, this notation provides a consistent way to define the coverage of adsorbed species, which will be the calculated simply with the number of adsorbed species N_{Species} according to $(N_x N_y)^{-1} N_{\mathrm{Species}}$ and will be given in mono-layers (ML). Attempts to define the coverage with for instance the

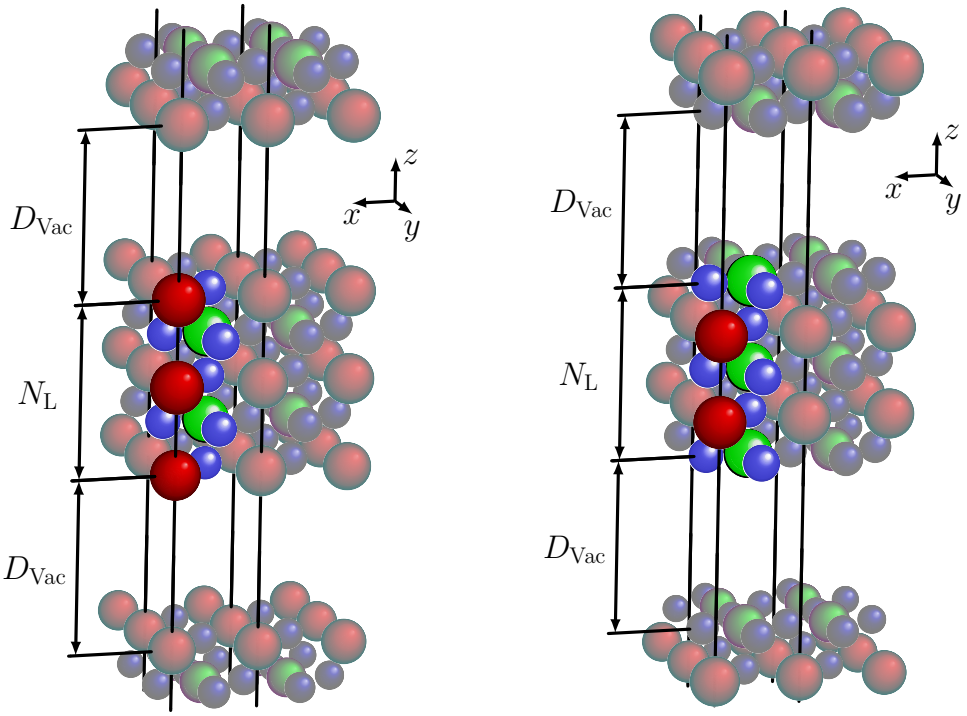

Figure 3.5: Perspective view on a SrO terminated (left) and a TiO_2 terminated (right) (1×1) surface model, each comprising five atomic layers of which the central three layers are held fixed in a geometry optimization. The black vertical lines denote the lateral dimension of the periodically repeated super-cell with the vacuum D_{Vac} and the slab thickness given in the number of layers N_{L}. The atoms in the actual super-cell are highlighted, whereas the shown periodic replica are paled.

number of atoms per surface unit cell is in the case of $SrTiO_3(001)$ quite confusing because the two terminations have a different number of atoms per surface area. A great amount of the work presented in the next chapters will be dealing exactly with the proper convergence of the adsorbates' energetics with respect to these four parameters of characterizing the size of the surface model geometry. However, the one which is most insensitive is the vacuum space allowing us to fix this in advance.

As an example we calculated the binding energy of the hydrogen ad-atom as function of D_{Vac} in Figure 3.6 and find that the empty space between the surface does not need to be greater than three lattice constants of $SrTiO_3$ to ensure a very good separation of the hydrogen atoms adsorbed on the each of the surfaces. However, in order to ensure reliability of our results also in cases where specimen are protruding further from the surface, we employed in all relevant surface calculation a vacuum exceeding 13 Å, i. e. at least 3.5 lattice constants.

In principle, the creation of the surface is accompanied with the formation of broken or dangling bonds, which are distinctly different from the bulk-internal bonds and thus raising the question if the hitherto applied plane-wave-basis sets and **k**-point-grids provide the numerical accuracy to describe them appropriately. The latter was indeed tested for the each individual adsorbed species in this work and the finally used **k**-point-meshes will be given in the respective paragraphs forward below. Since the bulk of the production calculations in the Chapter 4, Chapter 5 and Chapter 6 will be geometry optimizations, we show in Figure 3.7 the convergence of some selected ionic forces as function of the size of the plane wave basis set. Using numerically accurate forces in these optimizations implies already the convergence of energetics and therefore we skip the lengthy presentation of those tests. Because it will be among the adsorbed species, we present in Figure 3.7 also the force on the hydrogen ad-atom. Clearly, the oxygen pseudo-potential is the "hardest", i. e. it demands the biggest plane wave basis-set setting the lower limit for E_{Cutoff} to 430 eV to ensure an accuracy of the all ionic forces better than ± 0.05 Å/eV. This error-bar sets in turn a reasonable stopping criterion when optimizing the geometries. As panels (c) in Figure 3.7 substantiate, the forces on the oxygen atoms fluctuate about this value for larger basis sets and consequently higher resolutions of the forces should not lead to additional physical insight. We remark, that this error-bar has to be distinguished from the noise in the forces due to incomplete self-consistency of the electronic density. In fact, this noise can be systematically decreased simply by performing more SCF-cycles and was in all calculations about one order of magnitude smaller than the stopping criterion for the geometry optimization.

3.2.2 Energetics

With the two terminations it is possible to define an average surface energy, which can be regarded as the energy necessary to create the two differently terminated surfaces from a formally infinitely extended ideal $SrTiO_3$ sample. In order to avoid ambiguities with quantities discussed below we call this energy the "average cleavage energy " labelled E_{Cleav}. It may be calculated as function of the size of the super-cell model and serves therefore as an intuitive test quantity

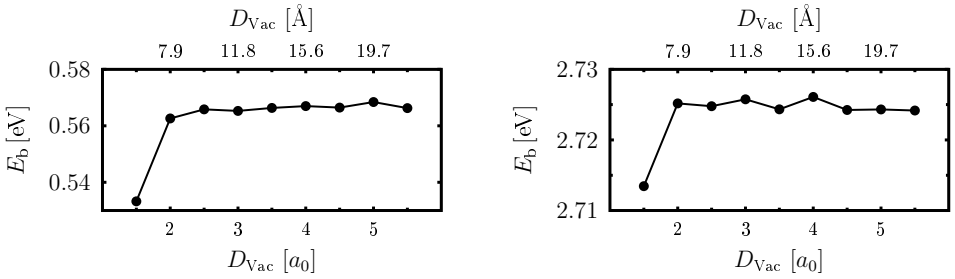

Figure 3.6: Binding energy of the adsorbed hydrogen ad-atom on the SrO- (left) and the TiO_2 termination (right) as function of the vacuum space separating the two surfaces in the surface model geometry. In order to make a fair comparison, the hydrogen ad-atom on the TiO_2 termination is not on the optimized geometry, but it was put approximately 1 Å above the surface, such that its vertical distance to the topmost lattice atoms corresponds to the one on SrO termination. The data was obtained using the PBE functional and (1×1)-surface model with 5 atomic layers, an plane-wave basis of 430 eV and $(12 \times 12 \times 1)$-**k**-points in the Brillouins-zone.

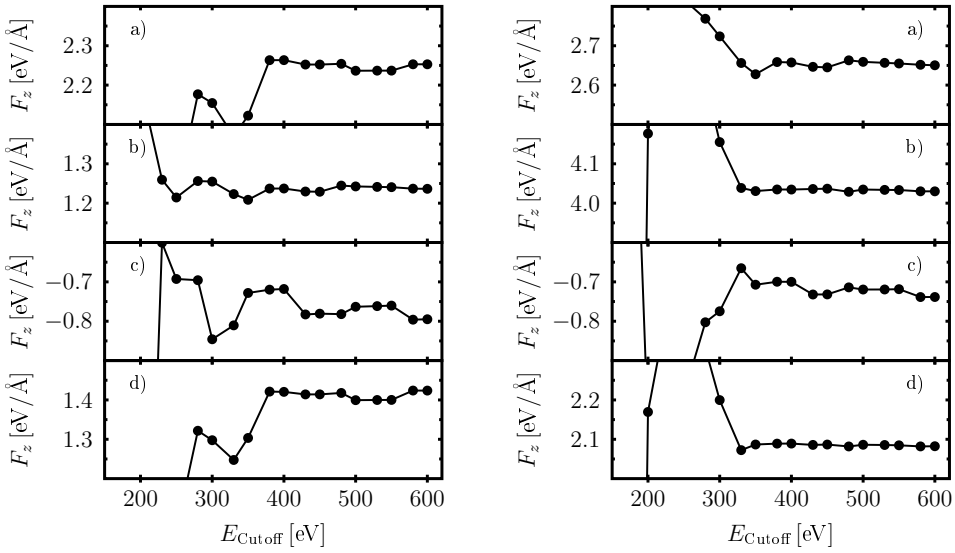

Figure 3.7: Vertical force components before relaxation as a function of the size of the plane wave basis set for (a) the hydrogen ad-atom, (b) the topmost cation on surface with the hydrogen ad-atom, (c) the topmost oxygen atom on the clean surface and (d) the topmost cation on the clean surface. The left side refers to the SrO, the right to the TiO_2 termination. In both case (1×1) surface models with five atomic layers were employed and the PBE functional was used for the electronic exchange-correlation.

to probe the reliability of for instance a (1×1)-surface model:

$$E_{\text{Cleav}}(N_{\text{L}}) = \frac{1}{2}\left[E_{\text{SrO-term.}}(N_{\text{L}}) + E_{\text{TiO}_2\text{-term.}}(N_{\text{L}}) - 2N_{\text{L}}E^{\text{Bulk}}_{\text{SrTiO}_3}\right] \quad , \tag{3.2}$$

where the first two terms represent the total energies of the two differently terminated slab models and the $E^{\text{Bulk}}_{\text{SrTiO}_3}$ is the total energy of one formula unit $SrTiO_3$ computed in the ideal, undistorted perovskite structure. The factor of two accounts for the two surfaces of each slab geometry. It is clear that the stability of solid $SrTiO_3$ requires E_{Cleav} to be strictly positive.

Comparing surface models with different number of layers yields information about the adhesion of the topmost terminating layer to the supporting bulk material. This may be defined for instance for the SrO termination and a (1×1)-surface model as:

$$E^{\text{SrO-term.}}_{\text{Ad}}(N_{\text{L}}) = \frac{1}{2}\left[E_{\text{SrO-term.}}(N_{\text{L}}) - E_{\text{TiO}_2\text{-term.}}(N_{\text{L}}-2)\right] - E^{\text{Bulk}}_{\text{SrO}} \quad , \tag{3.3}$$

where the $E^{\text{Bulk}}_{\text{SrO}}$ is total energy per formula unit of bulk strontium oxide. For the TiO_2 termination, the corresponding definition is shaped in complete analogy. The calculation of the total energies of bulk SrO and TiO_2 is outlined in Appendix A.

Figure 3.8 shows these three energies for different geometry set-ups and substantiates that the energetics of the clean $SrTiO_3(001)$ can be calculated reliably only with seven or more atomic layers in the model geometry. Here and in similar convergence test with respect to the geometric set-up presented the following chapters, we always re-used the information of "thiner" surface models "thicker" ones by simply by splitting up the fully relaxed structures and then inserting a new bulk-like layer of $SrTiO_3$. With re-adjusting then the constraints on the ionic positions and an enlargement of the vacuum space D_{Vac} about one lattice constant one obtains an extremely good basis for the optimization of the atomic positions in surface models with many atomic layers. Admittedly, this procedure does not allow a straightforward comparison to the "relaxation energies" given by some authors. However, since only the structures with minimal ionic forces are the thermodynamic relevant ones, we feel that this disadvantage is more than outweighed by the substantial gain of computational efficiency.

Our geometry-converged LDA value for the average cleavage energy of 1.24 Å per (1×1)-surface unit cell agrees quite well to data published in literature ranging from 1.19 eV to 1.26 eV [32, 197, 198]. The adhesion energies for the two different termination layers also suggests that their bond strength to the underlying bulk is quite different. The topmost SrO layer sticks per surface unit cell with about -1.2 eV and -1.0 eV to the surface for the two tested functionals, whereas the adhesion of the terminating TiO_2 layer is with -0.18 eV much higher, indicating that this capping layer may be removed much more easily from the surface than the other. This has to be rationalized with the fact that the removal of the terminating SrO layer destroys the energetically favorable octahedral coordination of the subsurface Ti-atom. In addition to this oxygen-titanium bond the Sr-cations assumes a bridging position above the subsurface oxygen anion providing besides the oxygen-titanium bonding also substantial electrostatic attraction to the second atomic layer. Contrariwise, detaching the topmost TiO_2 layer does not destroy a complete oxygen octahedron in the $SrTiO_3$ sample. This different binding of the topmost layers has of course direct consequences for the thermodynamic stability of the

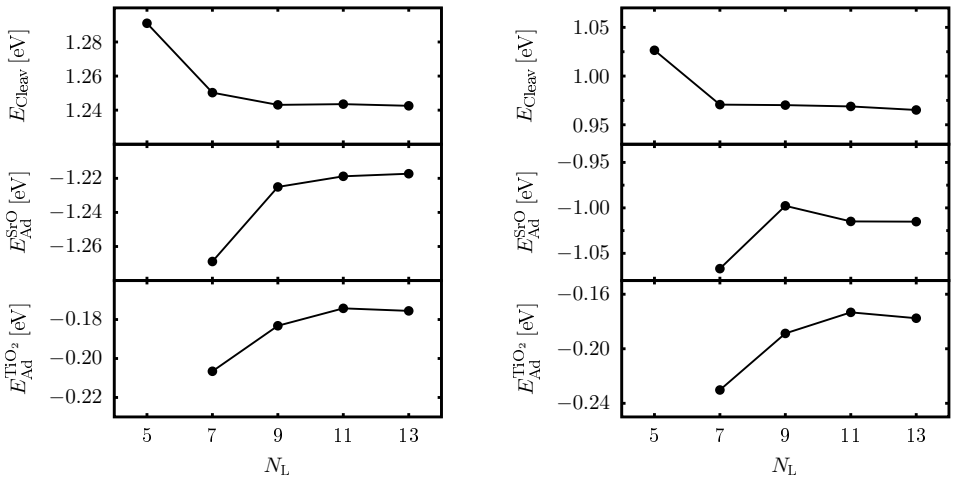

Figure 3.8: Average cleavage energy (top panel), adhesion of the topmost SrO layer (middle panel) and adhesion of the topmost TiO_2 layer as a function of atomic layers N_{L} in the (1×1)-surface model. The data on the left and right side was calculated within the LDA and the PBE functional for the exchange correlation, respectively.

two terminations, which will be discussed in detail in Section 4.3 in the context of the oxygen ad-atom.

3.2.3 Geometry

The relaxation of the $SrTiO_3(001)(1\times1)$ surface was subject of several recent first principle studies [197, 199, 200, 33]. It is found that the topmost layers do not simply relax, i. e. move towards the bulk, also a layer-internal deformation is observed. In the outermost layer the oxygen atoms are lifted with respect to the cations, whereas in the subsurface layer, they move inwards. In the third layer, the oxygen atoms move again outwards, such that in total an oscillation pattern emerges, i. e. in every odd-number atomic layer the oxygen atoms are lifted into the vacuum and in the even-numbered they move into the bulk. The amplitude of the vertical shifts decreases of course with increasing distance from the surface. The parameters characterizing these deformations are conventionally the change of the vertical distance $\Delta d_{i(i+1)}$ between the two cations on the ith the subsequent atomic layer with respect to its value in the bulk and lifting s_i of the oxygen atom with respect to those in-plane neighboring cations in the ith layer. The latter shifts are called “rumplings” or “puckerings”.

In Table 3.4 we compare the numerical values of these parameters to those obtained in other theoretical as well as experimental studies. Our data is fits quite well to the results of the preceding works, but we also note a substantial spreading of the entire data. In fact, the experimental side seems to disagree about the sign of the change of the first-layer-distance for SrO terminations, while the trend observed for Δd_{12} for the TiO_2 termination disagrees with all theoretical studies. Moreover, the deviations of the theoretically obtained numbers do not seem to depend too much on the different functionals as initially anticipated, but other technicalities, for instance pseudo-potentials and employed basis-sets. These two issues and the fact that the hitherto em-

ployed (1×1)-surface models do not account properly for possible lateral relaxations cast doubt on the usefulness of comparing exclusively vertical displacement parameters to the experimental observations. In fact, the definition of the parameters neglects possible lateral movements of the surface atoms and thus it excludes implicitly already real physics. However, for benchmarking different theoretical methods observing these parameters may still be advisable.

3.2.4 Electronic properties

Studying the different electronic structures of two terminations is essential for the understanding possible different behaviors with respect to chemical bonding of absorbents on the surface. As aforementioned, the dipoles between the differently charge SrO and the TiO_2 layers make the $SrTiO_3$(001)-surface in terms of Tasker's popular classification-scheme [205] a so-called Tasker-III-surface, i. e. it has a dipole moment, which needs to be compensated either by charge-rearrangements on the topmost layers or surface reconstructions. Goniakowski and Noguera pointed out already that in case of $SrTiO_3$(001) it is charge-rearrangements that compensate the layer-to-layer dipole and resolve the otherwise arising instabilities [167]. We recover their argumentation by analyzing again the computed Hirshfeld- and Mulliken charges in Table 3.5. Comparing to the charges listed in Table 3.3 we realize that already in the third layer the charge state of the individual atoms is already equivalent to one of the analogues in the bulk. Summing up these calculated individual charges we may estimate the total layer charge σ held by one unit cell of each layer and we obtain for the SrO termination a sequences for σ : +0.10e -0.17e +0.10e -0.11e and +0.43e -0.71e +61e -0.63e from the Hirshfeld- and Mulliken-scheme, respectively. Similarly we obtain for the TiO_2 terminated surfaces -0.07e +0.11e -0.10e +0.11e and -0.35e +0.62e -0.61e +0.64e with applying the two schemes. As aforementioned, the absolute values should not be taken too serious and numerical accuracy is certainly not better than $\pm 0.02e$, but in the in the latter case of the TiO_2 termination, both schemes yield in the topmost layer an approximately halved layer charge, which is necessary in order to cancel the internal electrostatic field and to stabilize thereby the surface [167]. In the case of SrO-termination the two topmost layers are involved in this charge rearrangement. Both schemes indicate that the subsurface TiO_2 layer becomes more negative, while they differ about the behavior of the topmost layer, whose averaged charge computes the Hirshfeld-scheme to be nearly unchanged with respect to the SrO layer in bulk, whereas the Mulliken-scheme predicts an increase by almost 40%. However, the numbers in Table 3.5 indicate that the charge state of the topmost strontium and oxygen atom are more ionic with respect to the bulk, only the sum of their charges stays nearly constant. Thus, regardless of the applied partitioning scheme, we note that the charge state of the surface or subsurface TiO_2 layer is different from a TiO_2 in bulk-like $SrTiO_3$. As termination layer it is more positive, i. e. electrons are re-directed into the bulk upon cleavage of the bulk. As a subsurface layer of a SrO terminated domain it accumulates charge density, such that it halves in combination with the terminating again the average layer charge per surface unit cell.

As already illustrated by the numbers in Table 3.3, the purely ionic model of $SrTiO_3$ is certainly too simple to give a reliable picture of $SrTiO_3$. For its surface, however, where to formation of an Ti^{3+} would be predicted, this concept seems to disagree completely with the data in Table 3.5. In fact, within our model the charge of the Ti-cation in the topmost layer becomes

Table 3.4: Rumpling parameters s_i and the change of the vertical cation-cation distances Δd_{ij} with respect to its bulk value calculated in (1×1)-surface models for different approximations for the electronic exchange correlation in the underlying electronic structure.

SrO-term.			Δd_{12} [%]	Δd_{23} [%]	Δd_{34} [%]	s_1 [Å]	s_2 [Å]
This work	LDA		-14	+5	-3	0.23	-0.05
	PBE		-15	+5	-5	0.22	-0.05
Theory	LDA	[197]	-17	+7	-4	0.30	-0.06
	LDA	[198]	-14	+5		0.22	
	PBE	[201]	-14	+6		0.23	
	PBE	[199]	-12			0.22	
	HF-GGA	[199]	-9	+4		0.18	
	B3PW	[202]	-13	+4		0.22	
Exp.	LEED	[203]	-10	+4		0.16	
	RHEED	[204]	+5	+ 3		0.16	
TiO_2-term.			Δd_{12} [%]	Δd_{23} [%]	Δd_{34} [%]	s_1 [Å]	s_2 [Å]
This work	LDA		-9	+7	-3	0.07	-0.12
	PBE		-13	+9	-2	0.09	-0.14
Theory	LDA	[197]	-13	+9	-2	0.07	-0.15
	LDA	[198]	-7	+3		0.07	
	PBE	[201]	-11	+6		0.08	
	PBE	[199]	-9			0.05	
	HF-GGA	[199]	-10			0.05	
	B3PW	[202]	-12	+7		0.08	
Exp.	LEED	[203]	+2	-2		0.08	
	RHEED	[204]	+4	+3		0.10	
	MEIS	[179]	+5			0.06	

Table 3.5: Hirshfeld- and Mulliken charges of the individual atoms on the two terminations of the $SrTiO_3(001)$ surface calculated using the PBE functional for the electronic exchange correlation.

	Top layer		Second layer		Third layer		Fourth layer	
SrO-term.	O	Sr	O	Ti	O	Sr	O	Ti
Q_H $[e]$	-0.40	0.52	-0.31	0.45	-0.31	0.41	-0.30	0.49
Q_M $[e]$	-0.83	1.25	-0.77	0.83	-0.76	1.37	-0.74	0.85
TiO_2-term.	O	Ti	O	Sr	O	Ti	O	Sr
Q_H $[e]$	-0.33	0.59	-0.29	0.40	-0.30	0.50	-0.30	0.41
Q_M $[e]$	-0.73	1.11	-0.73	1.35	-0.74	0.87	-0.74	1.38

even more positive with respect to a bulk titanium atom. Admittedly, this could also be in principle an artifact due to the employed pseudo-potentials, exchange-correlation functionals etc., but it should be noted that Goniakowski and Nogueras arguments are based solely on electrostatics. Having accepted that the TiO_2 layer bears in total a negative charge due to the partly covalent character of the titanium-oxygen bonds, it *must* become more positive on the surface to prevent the divergence of the electrostatic potential. If the topmost titanium atom would form a Ti^{+3}-species, which is clearly less positively charged than a Ti^{4+}, either the topmost oxygen atoms would have to suffer an enormous loss of electronic density or more complex charge rearrangements involving the second layer would have to take place.

Due to the destroyed periodicity at the surface, new electronic states may appear in the spectrum, which can in turn play an important role in chemical surface reactions. These states are detected in the electronic density of states being shown for the SrO and the TiO_2 terminated surface in Figure 3.9 On the SrO termination the O $2p$ valence band at the surface exhibits a slight shift towards lower energies with respect to bulk, which is in line with the decreased electrostatic potential detected by the enhanced polarity of the atoms in the topmost SrO layer. In turn, as indicated by the ionic charges in Table 3.5, the titanium atoms in the second layer becomes slightly less positively charged with respect to the titanium atoms in the bulk, lowering thereby due to the then amplified coulomb attraction the threshold for excited electrons to occupy exactly these atomic orbitals in the subsurface layer. This mechanism leads to the emergence of narrow band of unoccupied surface states below the conduction band minimum, which is restricted exclusively to the second atomic layer of the SrO terminated surface. Contrariwise, on the TiO_2 termination the formation of occupied electronic surface states directly on top of the valance band is observed. Monitoring the density of states at the bottom of the conduction band for different atomic layers detects slight tendency position to be shifted towards higher energies for the terminating TiO_2 layer in spite of the obvious depletion of the electronic density next to its titanium atoms. We rationalize this again with the argumentation of Goniakowski and Noguera [167]. A further occupation with electrons of the topmost layer would even decrease the its average charge, which computes in both the Hirshfeld- and the Mulliken-scheme already slightly below its actually demanded half of the average charge of a TiO_2 layer in bulk $SrTiO_3$. Thus, the additional population of the titanium orbital at the surface would increase the overall

surface formation or cleavage energy due to the unfavorable electrostatics and therefore the population excited states in the more bulk-like TiO_2 layers is energetically more attractive for the entire system.

These findings agree in principle with the results of preceding studies [144, 198, 160], i. e. we find the electronic band gap nearly constant for the SrO termination with respect to its bulk value, whereas for the TiO_2 termination, the band gap clearly shrinks. Within the LDA and using practically identical setting as Padilla and Vanderbilt [198], we computed the electronic band gap for the SrO and TiO_2 termination to 1.85 eV and 1.20 eV, where the preceding work arrived at 1.86 eV and 1.13 eV, respectively. However, we note that the employed the surface model consisted of only seven atomic layers, using in turn more layers and surface unit cell the electronic band gap exhibits variations of ± 200 meV, substantiating that it is much more sensitive towards the geometric set-up than the total energy. This is indeed quite comprehensible, because having numerically converged total energies does not imply that the individual eigenvalues have the same numerical quality. Because within this study we are only interested in the qualitative features of the electronic structure, we have to accept such a large error bar in which no substantial difference between the LDA and PBE arise for the electronic band gap.

In this chapter we have essentially re-computed the essential bulk and surface properties of $SrTiO_3$ as done already in previous studies. So far, we have employed both the LDA and the PBE functional for the exchange-correlation, because we could then directly compare to the already published data. However, in the following chapters in which we will present the actual subject of this study we use only the PBE-functional. Previous studies on the structural properties of bulk ferroelectrics such as for instance $BaTiO_3$ and $KNbO_3$ [206, 207] could not clearly establish a significant disadvantage for the PBE functional with respect to the LDA, however, there exists a notion that gradient-corrected functionals do improve adsorption energies with respect to the LDA when comparing to experiment. This is strongly corroborated by unsystematic tests, where we re-computed some of the subsequently discussed adsorption energetics within LDA leading to essentially identical geometries but to a substantially increased bond-strengths. In fact, with our numerical set-up, the energetics of the gas-phase molecules listed in Appendix B are computed much more realistically using the PBE-functional than within the pure LDA. Therefore we will focus exclusively in the following chapters only on the results obtained with the PBE-functional for the electronic exchange-correlation.

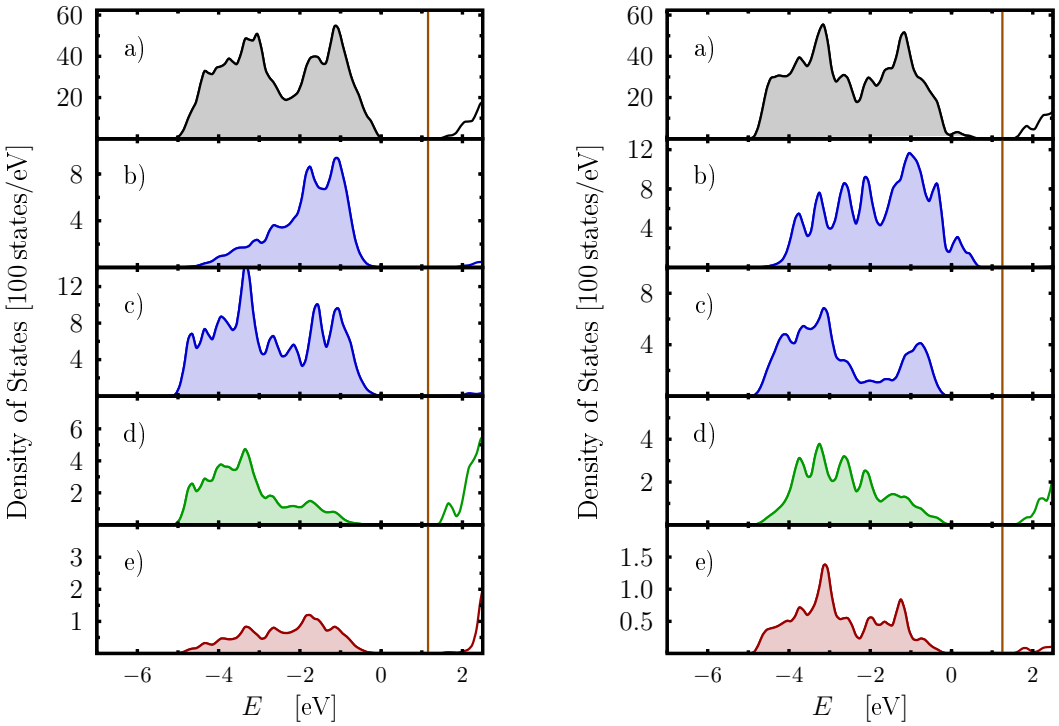

Figure 3.9: Electronic density of states of the SrO and the TiO_2 termination one the left and right side, respectively. On both sides, panel (a) shows total density of density of states of the entire surface model and panels (b) and (c) display the projections on the oxygen atoms integrated over in first and second layer, respectively. Panels (d) and (e) on the left side shows the contribution of the subsurface titanium and topmost strontium atoms to total spectrum, whereas on the right side, the same panels show the same projection on the first-layer titanium and second-layer strontium atoms, respectively. The original eigenvalue spectra have been convoluted with a Gaussian of 0.1 width and is reference here to the valence band maximum of the eigenvalue projection on the three innermost atomic layers of the 13-layer surface model, serving as approximation for the upper edge of valence band in bulk. The orange vertical line denotes the computed Fermi-energy, the filled curves mark the occupied, the empty curves the unoccupied states. The presented spectra have been calculated using the PBE functional for the exchange correlation.

4 Oxygen adsorption on $SrTiO_3(001)$

This chapter analyzes the adsorption of atomic oxygen on $SrTiO_3(001)$ in the limit of low coverages and the therewith accompanied formation of a peroxide ion on both terminations. Because the same subject has been discussed in a first-principles study using a hybrid-functional [208] for the electronic exchange correlation, we are able to demonstrate directly the reliability of the semi-local approximation not only for the pristine surface, but also for the case oxygen adsorption. In addition to that, we will be able to show that the size of the surface model plays a crucial role for the obtained energetics of the adsorbed oxygen atom.

The essential results of the first two sections of this chapter addressing the energetic and electric properties of the oxygen ad-atom have been published already in Ref. [209]. In Section 4.3 we will use the presented energetics of the ad-atom in order to to introduce the formalism of first-principles thermodynamics, which allows in principle to establish contact between theory and experiment. Since it has been suggested from the experimental as well as the theory side [1, 208] that the defect- and step-free $SrTiO_3(001)$ surface is de-facto inert with respect to adsorption of molecular oxygen, we will not go into detail about this issue here and direct the reader to Chapter 6, where the molecular adsorption of oxygen due to the presence of surface hydroxyl-groups is being discussed.

4.1 Energetics and geometry

The essential quantity characterizing the bonding to the surface is certainly the binding energy being defined as:

$$E_{\mathrm{b}} = \frac{1}{2}\left[E_{\mathrm{O@Surf}} - E_{\mathrm{Surf}} - E_{\mathrm{O_2}}^{\mathrm{Gas}}\right] \quad , \tag{4.1}$$

with $E_{\mathrm{O@Surf}}$ and E_{Surf} being the total energies of the surface with and without the oxygen ad-atom and $E_{\mathrm{O_2}}^{\mathrm{Gas}}$ being the total energy of the gas phase molecule. The factor of 1/2 is accounts for the double-sided adsorption in our surface model. Unlike the practical independence of the surface's energetics with respect to the actual size of the surface model, which was discussed in the previous chapter, the binding energy of the oxygen ad-atom decreases notably. The data in Table 4.1 illustrates that a proper convergence of the energetics within 50 meV require for the SrO and the TiO_2 termination at least (3×3)-surface unit cells with eleven and seven atomic layers, respectively. As aforementioned and as demonstrated forward below, the oxygen ad-atom forms a peroxide ion bearing a significant negative charge and protruding from the surface on both terminations being schematically illustrated in Figure 4.1. Thus, it is tempting to assign the decreasing binding energy to the coulomb repulsion of the adsorbed species with their periodic images. However, this would not account for the change of the binding energy due to the number

Table 4.1: Binding energies of the oxygen ad-atom on both terminations for some specific geometric set-ups. The binding energies E_b^{IA} and E_b^{IB} refer to the adsorption geometries "IA" and "IB" for the SrO and TiO_2 termination, respectively, which are shown in Figure 4.1. For the surface model of (4×4)-surface unit cells only the one shown **k**-point was used for summations in the Brillouins-zone.

Surface	**k**-points	N_L	E_b^{IA} [eV]	E_b^{IB} [eV]
(1×1)	$(7\times7\times1)$	7	0.28	0.69
		9	0.28	0.69
		11	0.27	0.70
(2×2)	$(4\times4\times1)$	7	-0.10	0.54
		9	-0.11	0.45
		11	-0.13	0.38
(3×3)	$(2\times2\times1)$	7	-0.10	0.33
		9	-0.15	0.30
		11	-0.20	0.29
		13	-0.22	—
(4×4)	$(\frac{1}{4},\frac{1}{4},0)$	7	—	0.30

of atomic layers and would in turn result in a similarly decreasing behavior for both terminations, which can not be derived from the data in Table 4.1. Therefore, it is much more likely that this behavior is predominantly due to the relaxations in the substrate, which have also been reported in another recent first-principles study addressing oxygen defects and the bulk and on the surface of $SrTiO_3$ [210]. Regarding the actual values of the binding energies, we find a clear preference of adsorption at the SrO termination of about 0.5 eV compared to the TiO_2 termination. At the latter the binding of the oxygen ad-atom is positive indicating an endothermic adsorption process with respect to the gas phase oxygen molecule. Thus, on the TiO_2 termination oxygen ad-atoms are thermodynamically unstable and will therefore recombine and desorb rather than populating the surface to a large extent. On the SrO termination the binding energy is slightly negative, denoting a weak exothermic adsorption. However, the value of -0.20 eV indicates only a too weak preference over the state of the gas phase oxygen molecule and therefore the obtained binding energies exhibit already that single oxygen ad-atoms are unlikely to represent a major species on both terminations on relevant experimental conditions.

Figure 4.1 presents the calculated ground-state configuration of the adsorbed oxygen ad-atom. Clearly visible is the formation of the bond between the oxygen ad-atom O_{Ad} and the lattice oxygen atom O(1) measuring 1.52 Å and 1.47 Å on the SrO and TiO_2 termination, which is indeed very close to the typical peroxide bond length varying around 1.50 Å for its different realizations such in, for instance hydrogen peroxide (H_2O_2), strontium peroxide (SrO_2) and many more [211, 212]. As already anticipated from the inspection of binding energies in Table 4.1, the impact of the ad-atom on the structure of the substrate system is different for each termination. On the SrO termination (cf. IA in Figure 4.1), the oxygen ad-atom O_{Ad} pulls the lattice

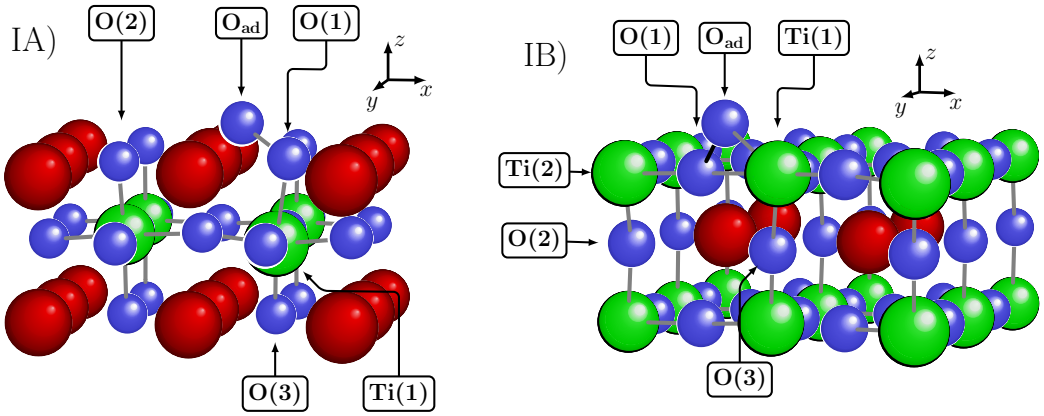

Figure 4.1: Schematic illustration of the most favorable adsorption geometry of the oxygen ad-atom at both terminations of $SrTiO_3(001)$.

oxygen atom O(1) at the binding site into the vacuum, whereas the subsurface Ti(1) relaxed into the bulk. As a result, the bond length O(1)–Ti(1) has stretched from 1.97 Å to 2.20 Å, giving rise to an effective weakening of the binding of the topmost SrO unit at the adsorption site to the subsurface Ti(1) atom due to oxygen adsorption. The surprisingly drastic decrease of the binding energy due to the number of atomic layers has to be explained with the oxygen ad-atom induced distortions of the surface perpendicular to the surface, being directly spotted by the shrinking of the bond of Ti(1) to the adjacent oxygen atom O(3) in the third atomic layer from 2.00 Å to 1.85 Å. Contrariwise, the most notable individual distortion in lateral direction is the small displacement of the adjacent surface lattice oxygen atom O(2), most likely due to the coulomb repulsion between this ion and the ad-atom. The further changes in the bond lengths of neighboring surface unit cell have to be classified individually as small, however, as illustrated by the data in Table 4.1, all together, they contribute remarkably to the binding energy, if fully developed in sufficiently large surface models. With the angle of 120° enclosed by the bonds Ti(1)–O(1) and O(1)–O_{Ad}, the configuration IA is reminiscent of the geometry found by Kantorovich and Gillian for the case of atomic oxygen adsorption on MgO(001) [213] and may be understood in terms of an "end-on" configuration of the dioxygen moiety with respect to the subsurface Ti(1) atom [212, 214].

For the adsorption configuration IB on the TiO_2 termination shown in Figure 4.1 in the right panel, the dependence on the number of layers is comparably weak, which is quite comprehensible because here the oxygen ad-atom is not directly coordinated to the subsurface layer. The dioxygen moiety is tilted towards one of its neighboring titanium atoms Ti(1), such that the bonds O_{Ad}–O(1) and O(1)–Ti(1) form an angle of 62°. In turn, the titanium atom Ti(1) is lifted somewhat from the surface, such that the bond length to the subsurface oxygen atom O(2) is stretched from 1.85 Å to 2.00 Å. Such bond lengths and angles are similar to the corresponding ones found in peroxo-titanium complexes [215] and may be categorized as "doubly-bridged" η^2-configurations and which are usually expected in dioxygen-metal complexes [216]. Simultaneously, the oxygen atom at the adsorption site O(1) is pressed a little below its original position into the bulk resulting in the extension of the distances O(1)–Ti(1) and O(1)–Ti(2) to 2.00 Å

and 2.13 Å, respectively. This mainly lateral distortion of the surface structure is the most notable one in configuration IB and requires a description in models of at least (3×3) surface unit cells, as indicated by the binding energies in Table 4.1. Contrariwise, the nearly unchanged bond length between the adjacent titanium atom to its subsurface oxygen neighbor O(2) of 1.84 Å, substantiates indeed that possible relaxations perpendicular to the surface do not play a major role for atomic oxygen adsorption on the TiO_2 termination.

The formation of an covalent oxygen-oxygen bond on the surface is initially rather unexpected, because the perovskite structure of bulk-$SrTiO_3$ does not comprise such a bond. This raises the question for the mobility of the adsorbed oxygen ad-atoms and stability of the oxygen-oxygen bond in comparison to alternative adsorption sites, because during the crystallization process of $SrTiO_3$ such possibly existent bonds should be removed. It is well understood that the actual removal is most likely a very complex process, which can not be assessed here. On the other hand, such processes can be expected to become more likely, the higher the mobility of the oxygen ad-atoms is. Consequently we have investigated in a more detailed way the energetics of the O_{Ad} by calculating the potential energy surface (PES) for its lateral motion on surface. This was accomplished in a straightforward way by optimizing the geometry with the lateral (x, y)-coordinates of the oxygen ad-atom being constraint to the respective position on the surface, while all other surface lattice atoms were completely free to relax. The resulting binding energies can be plotted as a two-dimensional function of x and y, representing then the targeted PES. Mapping this function in too small model systems, shown that also the its corrugation requires letting us explore the PES using the geometrically converged surface models as apparent from Table 4.1. The thereby calculated PES is presented in Figure 4.2 and reflects that its positions of the minima being represented by the spacious blue basins are located indeed at off-lattice positions of low symmetry. The initially anticipated, adsorption site at high-symmetry positions actually represent a saddle-point and a local maximum in the energetic landscape for the SrO and TiO_2 termination, respectively. For both terminations the resulting motion of the oxygen ad-atom can be categorized into two distinctive types. The first one is a dangling motion of the dioxygen species, in which the oxygen-oxygen bond is not broken. On the SrO termination this corresponds to a rotation of the dioxygen moiety about the z-axis, whereas in IB the oxygen-oxygen bond changes its orientation from pointing towards Ti(1) to Ti(2), i. e. it is essentially a "flipping". The respective barriers directly extracted from the PES are for this type of motion similarly small, i. e. 0.2 eV and 0.3 eV for the SrO and TiO_2 termination, respectively. More interesting are the barriers for breaking and re-formation of the oxygen-oxygen bond, i. e. for an elementary hopping process during diffusion. In units of the lattice constant a_0, the corresponding transition states are located at $(x,y) = (0.5, 0.0)$ as well as its symmetrically equivalents and poses a quite substantial barriers of $\Delta E = 0.81$ eV. On the TiO_2 termination the respective transition state is detected at $(x,y) = (0.27, 27)$ representing with an energetic level of 0.67 eV above the minimum only a slightly smaller obstacle for the oxygen ad-atom motion.

Using classical transition-state theory as a first, but for our purposes sufficiently accurate approximation, these barriers are the main ingredients for obtaining the temperature depended rate-constants ν from a simple Arrhenius-type equation [217]:

$$\nu = \nu_0 \exp\left(-\frac{\Delta E}{k_B T}\right) \quad , \tag{4.2}$$

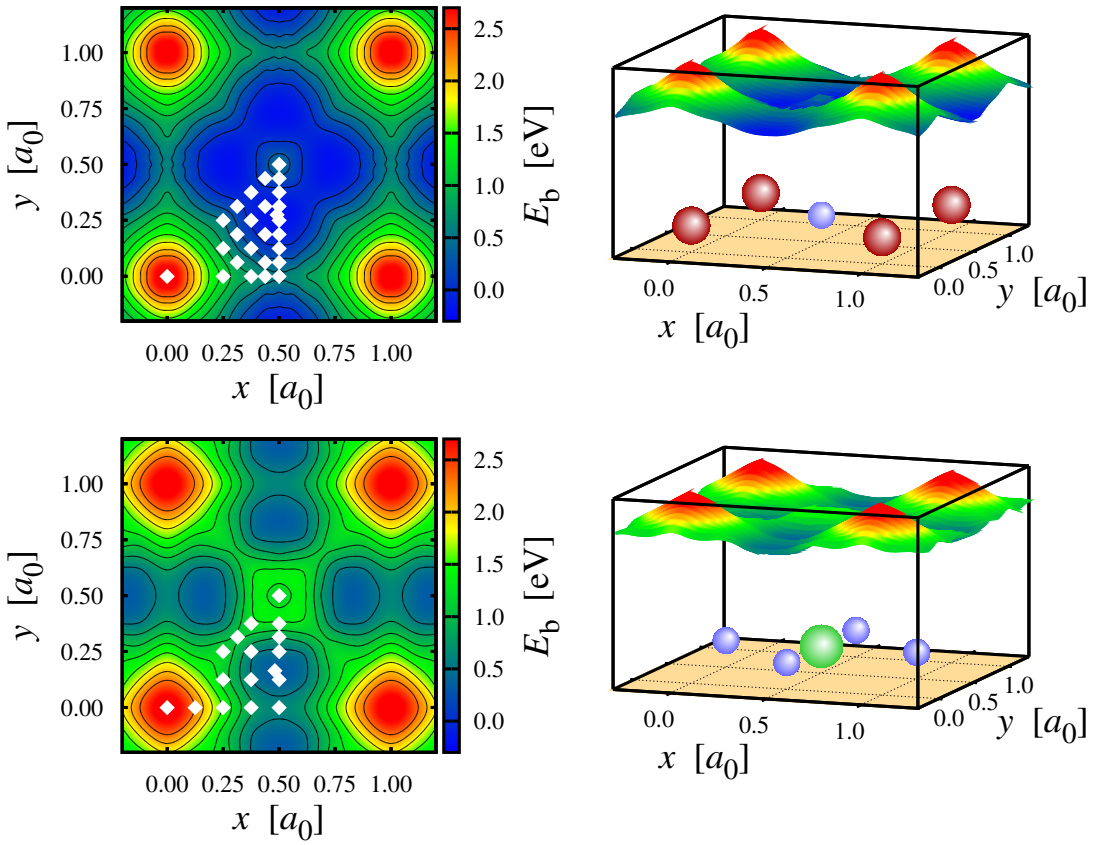

Figure 4.2: Two-dimensional potential energy surface (PES) for the lateral motion of the oxygen adatom on the SrO termination (upper panel) and the TiO_2 termination (bottom panel). The lateral coordinates x and y are given in units of the bulk lattice constant $a_0 = 3.938$ Å with the shown range for each termination corresponding to e on unit cell for contour plots on the left side. Thus, the position $(0,0)$ is directly atop of the Sr-atom on the SrO termination, while at the TiO_2 termination the position $(1/2,1/2)$ is atop of the Ti-atom. The white diamonds denote the actually calculated points within the irreducible wedge of the surface unit cell and neighboring isolines correspond to a difference of 0.25 eV.

where k_B and T are Boltzmann's' constant and the temperature. In principle, the pre-factor ν_0 can be derived from the PES numerically by evaluating straightforwardly the expression given by Vineyard [218]. However, having boiled down the dynamics to only two degrees of freedom, we have completely neglected the vibrations of the substrate atoms, which are required for a high-accuracy calculation of the pre-factor. Consequently, rate pre-factors calculated from the only two-dimensional PES should be considered only as a rough estimates letting us not follow this direction further. Therefore , we rely on the usual approximation for the pre-factor simply as the value of $\nu_0 \simeq 10^{13}\mathrm{s}^{-1}$, assumed to be constant for all configurations and all temperatures. This may be justified, due to the uncertainty of the energetic barriers, which enter as arguments of the exponential in Eq. (4.2), i. e. possible errors will have a much larger impact on the assessed rate than the errors introduced in the estimation of the vibrionic frequencies of the atoms.

Inserting the obtained energetic barriers for relevant temperatures in Eq. (4.2) reveals quickly that the aforementioned dangling of the oxygen-oxygen bonds is much faster than the elementary bond-breaking diffusion hop, i. e. the typical time-scales characterizing these motions differ by orders of magnitude, letting us consider only the diffusion hops as essential for the dynamics of the oxygen ad-atom on the surface. The actual binding energy at the transition states is clearly positive for both terminations, suggesting that, whenever two of such diffusing oxygen ad-atoms collide, they will most likely recombine to a neutral gas phase oxygen atom rather than populating the surface.

Due to cancellation of errors we may expect the corrugation of the PES is not too much affected by the semi-local approximation of the exchange-correlation for the underlying electronic structure of our surface model. However, for the stability of the ad-atom the *absolute* value of the binding energies is essential. In that respect it is quite gratifying that Piskunov *et al.* used in their aforementioned preceding study the "hybrid" B3PW functional for the electronic exchange correlation [208]. As aforementioned in Section 2.8, such "hybrid" functionals are employed for solids and surfaces to correct the pure semi-local functionals for their severest drawbacks, namely the underestimation of the electronic band gap of semiconductors and insulators. In combination with optimized basis-sets, the B3PW functional offers a sophisticated representation of the underlying electronic structure and provides description being especially fitted to the bulk properties of $SrTiO_3$. Therefore the authors considered it to be superior compared to our, more common approach [138]. However, as seen in Section 3.1.2 the improvement does not appear to be systematic which in turn challenges the justification its extensive computational costs In fact, these immense computational costs seem to be the primary reason, why Piskunov *et al.* were not able to address systematically finite-super-cell effects and why they were also not able to optimize all ionic positions unrestrictedly. Imposing certain, artificial symmetry constraints on their geometries and forces poses a clear obstacle to identify rigorously the correct ground-state adsorption geometries and thus the strictly correct binding energies. On the other hand, for the TiO_2 termination, they report a binding energy of 0.66 eV, with geometrical parameters very close to ours. Redoing their calculation using the same surface model, i. e., (2×2) surface unit cells and seven layers, we arrive at a binding energy of 0.60 eV, which is 60 meV greater than the correct binding energy listed in Table 4.1 and only 60 meV smaller than the value given by Piskunov *et al.*. This agreement can be considered as excellent agreement between these two different treatments for the underlying electronic structure. With the insight provide by the data of Table 4.1, accounting properly for the long-range-relaxation of the substrate seems to

have a stronger effect on the actually interesting binding energies than an certainly more accurate, but involved description of the underlying electronic structure. Furthermore, believe that the advantage of the relatively cheap semi-local functionals of allowing a thorough exploration of the PES has direct consequences for the comparison of the results of the SrO termination. Within the understanding of the PES topology shown in Figure 4.2 it appears that the restricted testing of the three possible high-symmetry adsorption sites has misled Piskunov *et al.* to identify erroneously the transition-state for the rotational-motion of the dioxygen moiety about the z-axis as the energetically most favorable adsorption site, while the energetic landscape was not scanned in the regions of lower symmetry and lower energy. Recalculating again this transition state in the corresponding geometry set-up, we obtain once again excellent agreement with the hybrid-functional, which fortifies eventually our confidence in the binding energies presented in Table 4.1.

4.2 Electronic properties

The interpretation of the dioxygen species as a peroxide anion is finally confirmed by analyzing in greater detail the electronic structure of the ground state configurations shown in Figure 4.1. Inspecting the adsorbate induced change of the charge density in Figure 4.3, shows that on both terminations the electronic structure of the surface is changed remarkably only at the close to the oxygen ad-atom and its partner atom O(1). This "difference electron density" is obtained by subtracting from the charge density of the surface with the oxygen ad-atom the charge densities of the "clean" surface and the charge density of the isolated atom. With positions of the respective atoms being the same, such a charge density difference highlights indeed nicely the occupation of the anti-bonding π^*-orbitals taking indeed as indicative for the formation of a dioxygen moiety. Calculating the Hirshfeld- and Mulliken-charges of the ions lets us quantify these charge-rearrangements further. Upon adsorption, both schemes yield for all surface ions practically the unchanged respective charges, except for the partner atom O(1), whose Hirshfeld-(Mulliken) -charge diminishes from -0.33e (-0.73e) to -0.16e (-0.38e) on the TiO_2 termination, while the same quantity changes simultaneously to -0.16e (-0.38e) for the initially neutral ad-atom. Thus, approximately half of the charge of the lattice oxygen atom O(1) is transfered to the ad-atom. At the SrO termination, the corresponding numbers at for the lattice oxygen atom O(1) are -0.38e (-0.83e) before and -0.20e (-0.50e) after the adsorption as well as -0.38e (-0.58e) for the oxygen ad-atom. This corroborates indeed the viewpoint provided by Figure 4.3 that the charge of two electrons, which is assigned formally to O(1) is basically shared O_{Ad} and O(1) after the adsorption. In combination with the absent spin moment and the bond length this allows only the interpretation as a peroxide anion O_2^{2-}.

The resulting electronic spectrum is analyzed in Figure 4.4, showing that the atomic oxygen adsorption leads on both terminations to an additional peak following up directly on top of the O $2p$ valence band. By mean of projection on the atomic orbitals, this electronic level can be directly associated with the anti-bonding π^* orbital of the oxygen peroxide species. Because it is not located far in band gap a possible interference with the erroneously to low calculated excited states as an artifact of the semi-local functionals can be ruled out here completely, which in turn is responsible for the excellent performance of the GGA-PBE-functional, concerning the

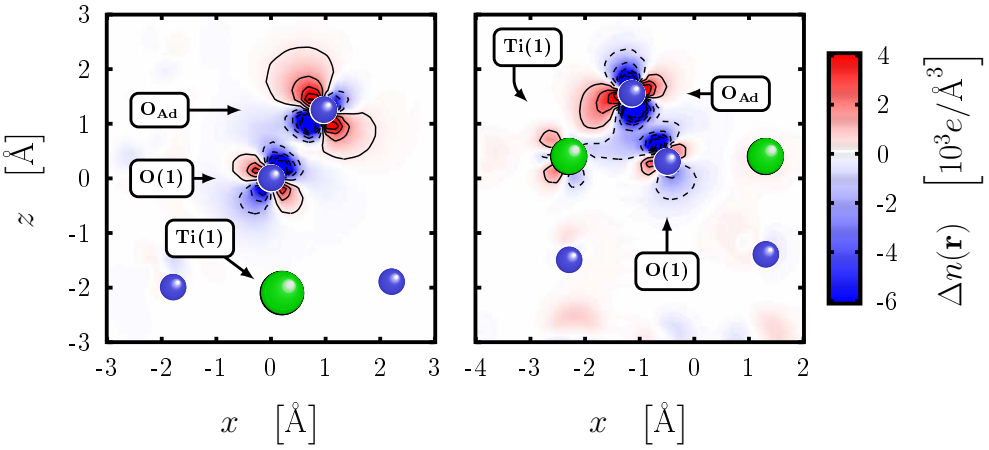

Figure 4.3: Difference electron density $\Delta n(\mathbf{r})$ plot highlighting the formation of the dioxygen moiety on the SrO and TiO_2 termination, left and right panel, respectively. Shown is the charge rearrangement in the plane defined by the oxygen ad-atom O_{Ad}, the directly coordinated lattice oxygen atom and the surface normal vector. The red (blue) areas with solid (dashed) isolines denote regions of charge accumulation (depletion). Neighboring isolines denote differences of $10^{-3}e/\text{Å}^3$. The superimposed spheres mark the positions of atoms within the plane.

interesting energetics, when compare the to the hybrid functional approach o Piskunov *et al.*.

In addition to the hints given by the analysis of the charge-density rearrangement, Figure 4.4 illustrates nicely the emergence of the molecular levels of the dioxygen species in the spectrum. At approximately -20 eV and -15 eV two very sharp peaks appear upon oxygen adsorption, which consist almost exclusively of contribution from the O 2*s* electrons of the O_{Ad} and O(1). The obvious interpretation is the hybridization of these states to the molecular bonding σ and anti-bonding σ^* orbital. Furthermore, the bonding O 2σ molecular orbital may be identified with the pronounced peak at -5 eV and -7 eV for the SrO termination and TiO_2 termination, respectively. In combination with the peak denoting the anti-bonding molecular orbital on top of the valence band, the eigenvalue spectra eventually confirm the clearly molecular state of to oxygen atoms. Qualitative differences between the two terminations can be spotted only for the bonding π-states, which are extensively overlapping with the 3*d*-orbitals of the adjacent Ti(1) atom and therefore substantially broadened for the SrO termination, while for on the TiO_2 termination a series of minor peaks appear. This indicates that these states are mostly responsible for the binding to the surface, and the differences can be attributed directly to the different coordination of the peroxide ion in configuration IA and IB.

4.3 Thermodynamic stability

For estimating the relevance of the calculated ground-state configurations under experimental conditions, the first-principles thermodynamics provide a nowadays standard tool [219, 220]. The general, rigorous formulation would be in principle possible, however, a demonstration using the energetics from the previous section as a concrete example seems to be more illustrative.

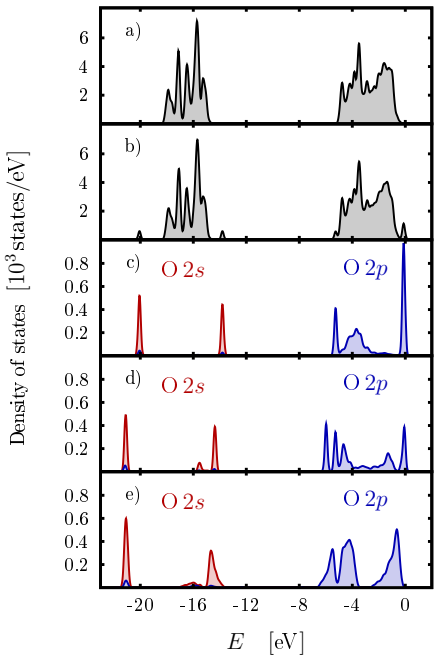

Figure 4.4: Density of states (DOS) analysis corroborating the interpretation in terms of the formation of a molecular peroxide species. The topmost panels show the total DOS of the topmost two layers of the SrO termination (a) before and (b) after oxygen adsorption. The next two panels show the DOS projected on the 2*s*-(red line) and the 2*p*-states (blue line) of the adsorbed oxygen atom and its directly coordinated parter oxygen atom for the SrO (c) and the TiO_2 termination (d), identifying the two sharply peaked states above and below the O2*s* group as fingerprints of the formed dioxygen moiety. (e) The same projected DOS of bulk SrO_2, exhibiting essentially the same characteristics. The top of the bulk valence band in the three central layers approximating the bulk is taken as zero-reference in all shown panels.

4.3.1 Formalism

We consider the $SrTiO_3$ sample in thermodynamic equilibrium with a reservoir system, which should also allow the addition or removal of particles from the atomic scale system. Consequently the Gibbs free energy of the $SrTiO_3$ sample G is intuitively the most convenient thermodynamic potential to describe the situation:

$$G = U - TS + pV \quad , \tag{4.3}$$

where U, S, T, p and V are the internal energy, the entropy, the temperature, the pressure and the volume, i. e. these are the quantities that can be provided in principle from the calculation on *ab-initio* level. Regarding the typical dimension of $\sim$ Å^3 of the interesting systems on atomic scale and the experimentally relevant pressures of certainly less than 10^7 Pa lets us estimate the contribution of the pV-term to the Gibbs free energy to less than 1 meV [220], which is already in smaller than the numerical error of the calculated total energies. Thus, the pV-term will be neglected in the following. The remaining terms $U - TS$ represent the Helmholtz free energy F, which can be evaluated, if the partition function $Z_{\{N_i\}}(T,V)$ of the system is known of given set of numbers of different specimen $\{N_i\}$:

$$F_{\{N_i\}}(V,T) = -\frac{\partial}{\partial\beta} \ln\left[Z_{\{N_i\}}(T,V)\right] \quad , \tag{4.4}$$

with the abbreviation of $\beta = (k_B T)^{-1}$ for the reciprocal value of product of the temperature and Boltzmann's constant. Obviously, the explicit evaluation of the last expression is very tedious of atomic systems we are currently interested in, if it is possible at all. Therefore, we approximate the Helmholtz free energy of a certain, stable atomic configuration with two terms

$$F = F^{\mathrm{Conf}} + F^{\mathrm{Vib}} \quad , \tag{4.5}$$

The first term stands for the contributions specific for each configuration and using the standard thermodynamic relations it may be written as $F^{\mathrm{Conf}} = U^{\mathrm{Conf}} - TS^{\mathrm{Conf}}$. The internal energy U^{Conf} comprises certainly the energy gain due to chemical bonding and therefore it may be identified with the total energy obtained directly from a first-principles calculation. As usual, in a pure thermodynamic treatment, only stable configurations with necessarily vanishing ionic forces play a role. Transitions between them and the corresponding transition times are not addressed at all within this formalism. We simply stipulate them to be "sufficiently fast", such that a practical immediate relaxation into the thermodynamic equilibrium upon a perturbation of the system is always guaranteed. However, it is quite comprehensible that a certain atomic "motif" can be realized in many, symmetrically equivalent configurations, which is then taken into account by the entropy S^{Conf}. With the number W of such energetically degenerate realizations, the corresponding entropy contribution is then calculated using Boltzmann's formula $S^{\mathrm{Conf}} = k_B \ln[W]$. A concrete example in the present context would be the number of possible adsorption sites for the oxygen atom in and possible rotations and "flips" of the newly formed peroxide ion shown in Figure 4.1. The second contribution in Eq. (4.5) accounts for the vibrations in the system and

is conveniently obtained within the harmonic approximation of the energetic landscape at the energetic minimum of the atomic arrangement and results in the following expression [221]:

$$F^{\mathrm{Vib}}(T) = \sum_{\alpha} \left[\frac{\hbar\omega_{\alpha}}{2} + \ln\left[1 - \exp\left(-\frac{\hbar\omega_{\alpha}}{k_{\mathrm{B}}T} \right) \right] \right] \quad , \tag{4.6}$$

where the index α runs over all the $3N-3$ different eigenmodes with the frequency ω_{α}, if N atoms are present in the model system. Thus, Eq. (4.5) may be viewed in terms of a second order expansion of the Helmholtz free energy, which may be extended further on without any principle problems if necessary. The Gibbs free energy of the $SrTiO_3$ sample can be subdivided into a part due to the bulk $G^{\mathrm{Bulk}}_{\mathrm{SrTiO_3}}$ and the surface, which is proportional to the surface area A of the sample:

$$G = G^{\mathrm{Bulk}}_{\mathrm{SrTiO_3}} + \gamma A \quad , \tag{4.7}$$

in which the surface formation energy γ plays the role of the proportionality factor. This factor must be necessarily positive, otherwise the sample would spontaneously disintegrate. The Gibbs free energy of the bulk refers here to the defect free bulk of the $SrTiO_3$ sample in the perovskite $Pm\bar{3}m$ phase and serves a thermodynamic reference. The thermodynamically most favorable atomic configuration at the surface with the Gibbs free energy G will then minimize γ, which is therefore the key observable in the first-principles thermodynamics formalism. For the sake of completeness, we mention that this concept not restricted only to surfaces, but it can be easily extended to the formation of for instance defects or alloys.

Having now specified the Gibbs free energy of the $SrTiO_3$ sample, we may use the Gibbs-Duhem relation [221] and write the macroscopic Gibbs free energy as a sum of the contributions of the individual reservoir systems, which are in our case strontium, titanium and gas phase oxygen:

$$G_{\mathrm{Macro}} = N_{\mathrm{Sr}}\mu_{\mathrm{Sr}} + N_{\mathrm{Ti}}\mu_{\mathrm{Ti}} + N_{\mathrm{O}}\mu_{\mathrm{O}} \quad . \tag{4.8}$$

Here, N_i and μ_i stand for the respective chemical potential and number of species. The stipulated strict independence of the reservoirs allows to treat them singly. This assumption guarantees the mutual independence of the chemical potentials, and has its direct correspondence in the experiment with principle possibility to adjust the partial pressures of the different species individually. Because of the thermodynamic equilibrium condition, this macroscopic Gibbs free energy should equal the thermodynamic reference of the system $G^{\mathrm{Bulk}}_{\mathrm{SrTiO_3}}$ and thus we can calculate the surface formation energy for a certain atomic configuration simply by rearranging Eq. (4.7) and inserting Eq. (4.7)

$$\gamma = \frac{1}{A}\left[F^{\mathrm{Conf}} + F^{\mathrm{Vib}} - \mu_{\mathrm{Sr}}N_{\mathrm{Sr}} - N_{\mathrm{Ti}}\mu_{\mathrm{Ti}} - N_{\mathrm{O}}\mu_{\mathrm{O}} \right] \quad . \tag{4.9}$$

The previous chapters emphasized that the calculation of the total energies involves many approximations, which are reasonable in this context, but which also prohibit an unambiguous evaluation of the numerical value of the total energy and thus the free Helmholtz energy. Consequently, the actual value taken by γ is not too important and it is more illustrative to compare the

surface formation energy of different atomic configurations, because this lets us estimate, which of them is the actual relevant under certain experimental conditions. Therefore, monitoring only relative surface formation energies allows a further simplification of Eq. (4.9). Firstly, the configurational entropy can be neglected here, because we are primarily interested in the adsorption of single atoms and molecules. Thus, the number of the individual realizations and thus the term TS^{Conf} for non-equivalent configurations will be very similar and does therefore not change the relative position of γ for different atomic configurations. In addition, for singly adsorbed atoms or molecules the number of possible realizations should be proportional to the number of surface unit cells in the surface model, leading also to no noticeable relative changes in γ, even for in very large model systems. However, if the interactions of the different specimen on the surface are to be studied explicitly, the number of possible, energetically equivalent configurations can increase quickly and lead to a substantial contribution to the surface formation energy.

Within this work we had also to neglect the vibrionic part of the Helmholtz free energy. Adsorption on the surface leads to the formation of only a very few new bonds per adsorbed specimen, which can be assumed to have only a very small impact on the vibration frequencies of the majority of the atoms in the surface model. Comparing adsorption geometries with similar stoichiometry, will lead to the formation of similar bonds with similar frequencies, which again results in only small relative changes of the surface formation energies. When comparing adsorption geometries with different stoichiometry, the different chemical bonds will result in very different bonding energies, which will in turn govern the relative changes of γ. The vibrionic contribution F^{Vib} may be regarded as a correction, being important under certain circumstances, but we will neglect them in the following. In addition, we want to emphasize that for our case the calculation of this correction would be rather tedious. As mentioned in Chapter 3, $SrTiO_3$ does not assume at 0 K the ideal perovskite structure we have used for our model. A brute-force calculation of the phonon-dispersion is therefore seriously hampered by soft-modes. On the other hand, fixing the all atoms in the substrate and taking into account only the vibrations of the adsorbed species does seem to be justified at first glance when facing substantial lattice distortions due to adsorption. Thus, we admit proceeding into that direction would be appealing for its fundamental interest, but in the present context it would cause a non-acceptable delay and we therefore approximate the Gibbs free energy in Eq. (4.3) directly with the total energy of the atomic configuration and rewrite Eq. (4.9):

$$\gamma = \frac{1}{A}\left[E^{\mathrm{Conf}}_{\mathrm{Total}} - \mu_{\mathrm{Sr}}N_{\mathrm{Sr}} - N_{\mathrm{Ti}}\mu_{\mathrm{Ti}} - N_{\mathrm{O}}\mu_{\mathrm{O}}\right] \quad . \tag{4.10}$$

In the following, the chemical potentials shall be referenced to the total energy per atom in their respective thermodynamic reservoir system. As reference states we chose those which are assumed by the pure species under standard conditions, i. e. room temperature and atmospheric pressure and we define accordingly the difference chemical potentials:

$$\Delta\mu_{\mathrm{Sr}} = \mu_{\mathrm{Sr}} - E^{\mathrm{Bulk}}_{\mathrm{Sr}} \qquad \Delta\mu_{\mathrm{Ti}} = \mu_{\mathrm{Ti}} - E^{\mathrm{Bulk}}_{\mathrm{Ti}} \qquad \Delta\mu_{\mathrm{O}} = \mu_{\mathrm{O}} - E^{\mathrm{Gas}}_{\mathrm{O}} \quad , \tag{4.11}$$

which shall characterize from now on completely the thermodynamic state of the ambient reservoir system. The calculation of the total energies on the right hand sides in Eq. (4.11) is described in detail in Appendix A and Appendix B. Rewriting the equilibrium condition again for one for-

mula unit $SrTiO_3$ allows to eliminate the explicit dependence on one arbitrarily chosen chemical potential, which shall be μ_{Ti} in following:

$$g^{Bulk}_{SrTiO_3} = \mu_{Sr} + \mu_{Ti} + 3\mu_O \quad , \tag{4.12}$$

with $g^{Bulk}_{SrTiO_3}$ being the Gibbs free energy of one bulk unit cell in the $SrTiO_3$ sample. Strictly speaking, $g^{Bulk}_{SrTiO_3}$ comprises contributions similar to Eq. (4.5), however with the same arguments as before, we approximate the latter correspondingly only with the respective total energy $E^{Bulk}_{SrTiO_3}$. In combination with the last equations we rewrite Eq. (4.10) once more:

$$\gamma = \Phi^{Conf} - \Gamma^{Conf}_{Sr}\Delta\mu_{Sr} - \Gamma^{Conf}_{Ti}\Delta\mu_O \tag{4.13}$$

where we have define the excesses Γ:

$$\Gamma^{Conf}_{Sr} = \frac{1}{A}\left[N_{Sr} - N_{Ti}\right] \qquad \Gamma^{Conf}_{O} = \frac{1}{A}\left[N_O - 3N_{Ti}\right] \quad , \tag{4.14}$$

and the constant Φ:

$$\Phi^{Conf} = \frac{1}{A}\left[E^{Conf}_{Total} - N_{Ti}(E^{Bulk}_{SrTiO_3} - E^{Bulk}_{Ti}) - \Gamma^{Conf}_{Sr}E^{Bulk}_{Sr} - \Gamma^{Conf}_{O}E^{Gas}_{O}\right] \quad . \tag{4.15}$$

The superscript "Conf" will be omitted in the following, because using the introduced formalism, quantities of the atomic and the reservoir system can not be confused anymore. The constant Φ contains obviously all energetic contributions obtained from first-principle methods, and is obviously the constant term of γ, which has the shape of a plane in the two-dimensional space spanned by $\Delta\mu_{Sr}$ and $\Delta\mu_O$. The excesses Γ account only for the stoichiometry of different atomic configurations, and represent the slopes of the aforementioned plane. Contrariwise, the properties of the reservoir system are characterized exclusively by the difference chemical potentials, which is, of course, due to the complete neglect of all entropic contributions. In fact, a re-inclusion of these entropic terms would make Φ a function of temperature. How to establish finally contact with the experimentally adjustable quantities such as temperature and pressure using the chemical potentials will be elucidated forward below for the case of gas phase species.

4.3.2 Chemical potentials

Before applying the developed formalism to the oxygen adsorption at the $SrTiO_3$ surface, we feel it is instructive to show at this point how to establish the connection between chemical difference potentials and the respective, adjustable conditions in the experiment. Concerning the metal ions, it is not quite clear how to define exactly the quantities $\Delta\mu_{Sr}$ and $\Delta\mu_{Ti}$, because little is known, about how these species actually arrive at the surface.

In order to avoid speculations, we simply consider $\Delta\mu_{Sr}$ and $\Delta\mu_{Ti}$, simply as numerical parameters, which have to be associated with the "availability" of the Sr- and Ti- atoms at the surface system, i. e. high values indicate Sr- and Ti- rich conditions, whereas lower values stand for the depletion of these species in the system.

Fortunately, the case of oxygen is much more obvious. Oxygen arrives in practice at the

surface in its gaseous state, which can be treated in good approximation as an ideal gas and which in turn lets us calculate now the oxygen chemical potential explicitly. The key quantity is here the canonical partition function $Z_N(T,V)$ of N oxygen molecules at a temperature T in the volume V, which may be written as product of the partition function of the center of mass motion of the oxygen molecule as well as partition function of their internal coordinates:

$$Z_N(T,V) = Z_N^{\mathrm{COM}}(T,V)\,\left(Z_{\mathrm{Int}}(T)\right)^N \quad . \tag{4.16}$$

For the center of mass motion, the partition function is simply the well-known textbook result [221]:

$$Z_N^{\mathrm{COM}}(T,V) = \frac{1}{N!}\left[\frac{V}{V_{\mathrm{Q}}(T)}\right]^N \qquad \text{with} \quad V_{\mathrm{Q}}(T) = \left[\frac{1}{h}\sqrt{2\pi m_{\mathrm{O}_2} k_{\mathrm{B}} T}\right]^3 \quad , \tag{4.17}$$

where h is Planck's constant and m_{O_2} stands for the oxygen molecules' mass. The hereby introduced quantum volume $V_{\mathrm{Q}}(T)$ of the oxygen molecules is obviously only a function of the temperature. Variation of the particle number N suggests a weighted summation of the respective canonical partition functions, which defines the grand canonical partition function $\tilde{Z}$:

$$\tilde{Z}_\mu(T,V) = \sum_{N=0}^{\infty} Z_N(T,V)\exp\left(\frac{N\mu}{k_{\mathrm{B}}T}\right) \quad , \tag{4.18}$$

with μ being the chemical potential. For an ideal gas $\tilde{Z}$ can be evaluated directly:

$$\tilde{Z}_\mu(T,V) = \exp\left[\frac{V}{V_{\mathrm{Q}}(T)} Z_{\mathrm{Int}}(T)\exp\left(\frac{\mu}{k_{\mathrm{B}}T}\right)\right] \quad . \tag{4.19}$$

The logarithm of grand-canonical partition-function $\tilde{Z}$ corresponds to the average particle number, which equals in case for the ideal gas the product of pressure and volume divided by $k_{\mathbf{B}}T$. This in combination with the latter equation and the energetic shift according to Eq. (4.11) lets us finally calculate the atomic oxygen chemical potential as:

$$\mu_{\mathrm{O}} = E_{\mathrm{O}}^{\mathrm{Gas}} + \frac{1}{2}k_{\mathrm{B}}T\left(\ln\left[\frac{p_0 V_{\mathrm{Q}}(T)}{k_{\mathrm{B}}T}\right] - \ln\left[Z_{\mathrm{Int}}(T)\right]\right) + \frac{1}{2}k_{\mathrm{B}}T\ln\left[\frac{p_{\mathrm{O}_2}}{p_0}\right] \quad , \tag{4.20}$$

where the factor of 1/2 divides the terms on the right hand side, which have to be calculated clearly only for oxygen molecules. For convenience, we have introduced a reference pressure p_0, allowing to write the dependence in the oxygen pressure p_{O_2} separately. The value of p_0 shall be in the following the atmospheric pressure of $1.01 \cdot 10^5$ Pa. Apart from the mass of the oxygen molecule, we have not made any specifications towards oxygen so far. These shall be introduced now by assuming the vibrating dumbbell to model the internal degrees of freedom. The corresponding Hamiltonians read for the rotational and the vibrionic part [222]

$$H_{\mathrm{Rot}} = \frac{h^2 l(l+1)}{4\pi^2 m_{\mathrm{O}_2} R_{\mathrm{O}_2}} \qquad H_{\mathrm{Vib}} = h\nu\left(n+\frac{1}{2}\right) \quad , \tag{4.21}$$

where l is the quantum number of the angular momentum, ν is the stretching frequency and R_{O_2} is oxygen-oxygen bond-length of the oxygen molecule. The partition function of rotations is calculated in practice straightforward by performing the sum numerically:

$$Z_{\mathrm{Rot}} = \sum_{l=0}^{\infty} (2l+1) \exp\left(-\frac{hl(l+1)}{2\pi m k_{\mathrm{B}} T}\right) \quad , \tag{4.22}$$

whereas the partition function of the harmonic oscillator can be evaluated analytically:

$$Z_{\mathrm{Vib}} = \sum_{n=0}^{\infty} \exp\left[-\frac{h\nu}{k_{\mathbf{B}} T}\left(n+\frac{1}{2}\right)\right] = \frac{\exp\left(-\frac{h\nu}{2k_{\mathbf{B}}T}\right)}{1-\exp\left(-\frac{h\nu}{k_{\mathbf{B}}T}\right)} \quad . \tag{4.23}$$

Inserting of into Eq. (4.20) yields then the interesting difference chemical potential for oxygen $\Delta\mu_{\mathrm{O}}$ as function of the temperature and the pressure of the oxygen gas. On the other hand, the enthalpy $H(T, p_0)$ and entropy $S(T, p_0)$ of oxygen gas have been experimentally measured, and can be looked up for instance in Ref. [223]. Using this data in combination with thermodynamic relation $G = H - TS$, we may compute $\Delta\mu_{\mathrm{O}}(T, p)$ directly [220]:

$$\Delta\mu_{\mathrm{O}}(T,p) = \frac{1}{2}\left[\left[H(T,p_0) - H(T_0,p_0)\right] - T\left[S(T,p_0) - S(T_0,p_0)\right] + k_{\mathrm{B}} T \ln\left(\frac{p_{\mathrm{O}_2}}{p_0}\right)\right] \quad , \tag{4.24}$$

where the enthalpy and entropy at T_0 stand here for the respective extrapolation to 0 K. In Figure 4.5 $\Delta\mu_{\mathrm{O}}$ has been calculated using the two different approaches of Eq. (4.20) and Eq. (4.24) and shows indeed the very good agreement even at elevated temperatures. At 1200 K for instance, the two lines do not differ more than 20 meV. In the following however, we will rely on Eq. (4.24) for the calculation of the chemical potential. For diatomic molecules this does not play a role at all, but in Chapter 5, we will apply the formalism to the adsorption of water molecules, whose internal motions can certainly not be described using modest model of Eq. (4.21). In this case, employing only the data of the thermodynamic tables is much more efficient.

In the last paragraphs we have demonstrated for the case of oxygen how to the experimentally adjustable, macroscopic quantities are coupled via the difference chemical potentials to the actually interesting surface formation free energies γ in Eq (4.13). Within these steps the capability of the introduced formalism is ultimately manifested.

4.3.3 Phase diagram

Employing now the energetics obtained in the Section 4.1 in combination with Eq. (4.13) lets us determine the surface morphology as a function of the experimental conditions. Obviously the existence of $SrTiO_3$ is restricted to certain domains in the space of the chemical difference potentials $\Delta\mu_{\mathrm{O}}$ and $\Delta\mu_{\mathrm{Sr}}$. The upper limits can be determined quickly from Eq. (4.11). If any of the difference chemical potentials is zero the surface system under investigation would be in thermodynamics equilibrium with the respective bath system, which restricts the interesting domains of the difference chemical potentials to strictly negative values. In addition, there are

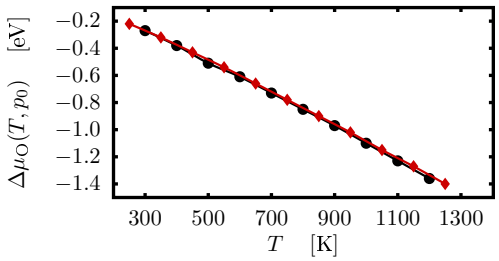

Figure 4.5: Oxygen difference chemical potential calculated at atmospheric pressure p_0 using the tabulated data (black circles) and Eq. (4.20) with the model of a vibrating dumbbell for the molecular internal degrees of freedom (red diamonds), being specified in Eq. (4.21).

still other materials, which can be created from oxygen, titanium or strontium. For instance, for its stability, it is clear that bulk TiO_2 will be formed under oxygen-rich and titanium-rich and thus strontium-poor conditions . This restricts the difference chemical potentials below the Gibbs-free energy per formula unit $G^{\text{Bulk}}_{TiO_2}$ of bulk TiO_2:

$$G^{\text{Bulk}}_{TiO_2} - E^{\text{Bulk}}_{Ti} - 2E^{\text{Gas}}_{O} > \Delta\mu_{Ti} + 2\Delta\mu_{O} \tag{4.25}$$

With the same arguments as before we approximate $G^{\text{Bulk}}_{TiO_2} \approx E^{\text{Bulk}}_{TiO_2}$ with the total energy. The left side of the last equation defines then the formation energy of bulk TiO_2. Under titanium-poor, i. e. strontium-rich conditions, the formation of strontium oxide and strontium peroxide is expected, which puts further constraints on the difference chemical potentials:

$$\begin{aligned} G^{\text{Bulk}}_{SrO} - E^{\text{Bulk}}_{Sr} - E^{\text{Gas}}_{O} &> \Delta\mu_{Sr} + \Delta\mu_{O} \\ G^{\text{Bulk}}_{SrO_2} - E^{\text{Bulk}}_{Sr} - 2E^{\text{Gas}}_{O} &> \Delta\mu_{Sr} + 2\Delta\mu_{O} \quad , \end{aligned} \tag{4.26}$$

where the Gibbs-free energies on the left hand sides are approximated again in the same manner as in Eq. (4.25).

Figure 4.6 presents the resulting phase diagram. The stable region of $SrTiO_3$ is marked with a thick white line and represents only a stripe across the space spanned by $\Delta\mu_O$ and $\Delta\mu_{Sr}$. As already pointed out atomic oxygen adsorption results in strict thermodynamic stability only on the SrO termination under oxygen-rich conditions. The region in which the TiO_2 termination represents the thermodynamic equilibrium of the $SrTiO_3$-sample, is only a very narrow stripe, colored in dark green in Figure 4.6. This suggests strongly that its preparation would be difficult, because only a slight change of the conditions in the surfaces environment would stabilize either the SrO termination or would lead to the formation of bulk TiO_2. We emphasize that this result does not seem to depend on the applied semi-local electronic exchange-correlation, pseudopotentials or similar, because in two further studies using the LDA [32] or the aforementioned hybrid approach [33] have found essentially the same. This result has led to discussions about the surface morphology of $SrTiO_3$ between the experimental and the theory side, because many surface preparation techniques are reported to lead to predominantly TiO_2-terminated samples. However, in a recent experiment it was shown that upon sufficiently long and sufficiently intensive heating initially TiO_2 terminated samples exhibit large SrO terminated domains [224].

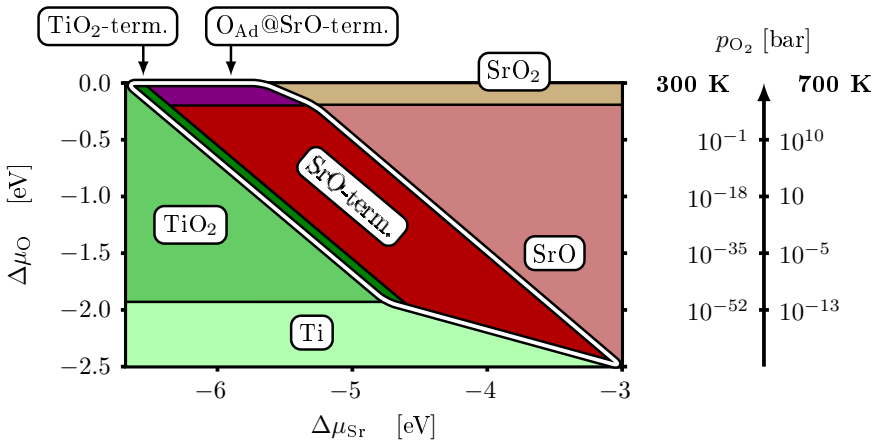

Figure 4.6: Phase diagram of $SrTiO_3$ as a function of $\Delta\mu_O$ and $\Delta\mu_{Sr}$. The encircled area marks the stable the region of $SrTiO_3$. On the right side, the oxygen difference chemical potential has been converted to oxygen pressures scales for two exemplary temperatures. Low values of the strontium difference chemical potential are to identified with titanium-rich and strontium-poor conditions, while increase values stand for a strontium-rich and titanium-poor environment.

After 72 h of annealing the sample at 1300°C, the entire sample appeared to be completely SrO terminated. In fact, the ratio of the SrO and TiO_2 domains on the surface appear to change monotonically with time, allowing to create samples with an arbitrary proportion of the two different terminations. This observation is completely in line with the notion that the different TiO_2 rich reconstructions and formations reported on the $SrTiO_3$ surface do not represent the strict thermodynamic equilibrium [195, 32]. They can be regarded as states being "trapped" by large barriers and thus hindering the full equilibration of the system. On the other hand, large barriers and extremely long relaxation times ensure a "local" equilibrium, justifying a thermodynamic description constraint to a subset of possible and rationally comparable candidate configurations. Such a subset is defined in the most efficient way simply by basic intuition in combination with an estimation of the energetic barriers in the connecting path in the potential energy landscape.

As visible in Figure 4.6 and already suspected before, oxygen ad-atoms are too weakly bound to the surface to represent a major species on experimental conditions. However, the configurations IA and IB in Figure 4.1 indicate that oxygen ad-atom may be created by molecular oxygen adsorption into oxygen vacancies. The latter are known to be F-centers and recent calculations have shown that their presence induces an occupied level in deep in the band-gap making effectively charge highly available [210, 225]. Oxygen molecules in turn have a negative electron affinity, i. e. the formation the reaction $O_2 + e^- \rightarrow O_2^-$ is exothermic with -0.44 eV [212] making this mechanism of defect annealing by molecular adsorption extremely probable. According to our obtained energetics, the resulting oxygen ad-atoms will then recombine and depart eventually from the surface. On the other hand, Irvine *et al.* pointed out that similar to oxygen defects, hydroxyls, super-oxide and peroxide anions may be well incorporated into complex perovskite material [226]. Consequently, the upper bound for the growth rate of a possibly defect-free complex oxide film deposited on $SrTiO_3$ is set by the rate of the recombination of the oxygen

ad-atoms. However, because of the complexity of such a process, it would be naive to derive such a rate for the removal of the described peroxide species only on the basis of the energetics presented in Section 4.1.

5 Water adsorption on $SrTiO_3(001)$

Using the techniques presented in the previous chapters, we now turn to the adsorption of water on $SrTiO_3(001)$. Similar to the case of oxygen we are focusing primarily on the interaction of water and the surface in the dilute limit, such that possible interactions of the adsorbed H_2O-species on the surface are treated only implicitly due to the imposed periodic boundary conditions. Section 5.1 focuses the adsorption process itself and the resulting ground-state configurations. In Section 5.2 we will extend the first-principles thermodynamics formalism in order to analyze the stability of the obtained conformations, which will turn out to rationalize the experimental results of Iwahori *et al.* [38]. Then, in Section 5.3, we try to relate our results to further experiments reported in literature. Finally, in Section 5.4 we will address the actual dissociation and further decomposition of the adsorbed water species on the surface. The results presented in this chapter have been published already in condensed form in a recent publication [227].

5.1 Initial stages of adsorption

Similar to the previous chapter, convergence with respect to the size of the surface model is controlled by monitoring the binding energy of the water molecule, which is defined as:

$$E_{\mathrm{b}} = \frac{1}{2}\left[E_{\mathrm{H_2O@Surf}} - E_{\mathrm{Surf}} - 2E^{\mathrm{Gas}}_{\mathrm{H_2O}}\right] \quad , \tag{5.1}$$

where the factors of 1/2 and 2 account for the double sided adsorption in our surface model. For convenience, we refer the binding energy to the total energy of the water molecule in gas phase $E^{\mathrm{Gas}}_{\mathrm{H_2O}}$, whose calculation is described in detail in Appendix B. Although water may also well exist under relevant conditions in condensed form, the description on *ab initio* level of the interaction of water molecules and thus of liquid and solid water is still subject of ongoing research [228]. Therefore, we consider water only in its vapor phase hereafter. Test geometries were the ones presented in Figure 5.1, Figure 5.3 and Figure 5.5, which will be discussed in detail forward below. They have also been considered in different recent studies using either different methods for the description of the underlying electronic structure [34] or different basis sets [35, 229, 230]. However, none of these studies compared all three adsorption structures with each other, nor were the resulting energetics checked with respect to different sizes of the surface model.

The data in Table 5.1 confirms that (1×1) surface models do not describe singly adsorbed molecule appropriately in the dilute limit and illustrates that the testing the thickness can lead to wrong conclusions, when neglecting the lateral extension of surface model. Similar to the case of the oxygen ad-atom in the previous chapter, eleven atomic layers are required to shrink the error-bar due to finiteness of the surface model below 50 meV. For comparable geometric

Table 5.1: Binding energies of the adsorbed water molecule the configurations (IIA1), (IIB1) and (IIB2) for some specific geometric set-ups as well as a comparison to the values published in literature. The configurations (IIA1), (IIB1) and (IIB2) are shown in Figure 5.1, Figure 5.3 and Figure 5.5. All energies are given in eV.

	Surface	k-points	N_{layer}	$E_{\text{b}}^{\text{IIA1}}$	$E_{\text{b}}^{\text{IIB1}}$	$E_{\text{b}}^{\text{IIB2}}$
	(1×1)	$(7\times7\times1)$	7	-0.83	-0.77	-0.58
			9	-0.84	-0.78	-0.58
			11	-0.83	-0.78	-0.59
	(2×2)	$(4\times4\times1)$	7	-1.18	-0.74	-0.85
			9	-1.24	-0.73	-0.92
			11	-1.28	-0.73	-0.95
			13	-1.31	—	—
	(3×3)	$(2\times2\times1)$	7	-1.22	-0.71	-0.90
			9	-1.30	-0.72	-0.97
			11	-1.35	-0.72	-0.99
			13	-1.38	—	—
Ref. [34]	(1×1)		7	-0.79	-0.73	-0.63[a]
Ref. [35]	(1×1)		7	-0.81	-0.73	—
Ref. [35]	(2×2)		7	-1.10	-0.74	—
Ref. [230]	(2×2)		7	—	-0.83	-0.92
Ref. [229]				—	-0.83	—

[a] The value includes the correction of 0.12 eV of basis superposition error as estimate by the authors.

set-ups however, the data shows an overall good agreement with the aforementioned preceding works, corroborating our surmise that studying adsorption of on the $SrTiO_3(001)$ surface requires a treatment of the electronic exchange correlation permitting to investigate systematically the effects of the finiteness of the surface model. The numbers given by Lin *et al.* [230] and Wang *et al.* [229] in seem to display a systematic shift of ≈ -100 meV compared to to ours, which may be explained by their use of the PW91 exchange-correlation functional. On the other hand, the energetic difference between the two configurations IIB1 and IIB2 on the TiO_2 termination (cf. Table 5.1) is only marginally affected and therefore pointing rather at a different reference energy of the gas phase water molecule than at a deviant description of the surface.

5.1.1 SrO termination

In accord with the results of Baniecki *et al.* [35] we find the direct dissociation of the water molecule upon adsorption, which leads in combination with a lattice oxygen atom to the formation of two hydroxyl-groups assuming finally the configuration (IIA1) depicted in Figure 5.1. Visual inspection of this atomic arrangement as well as the numerical values for some selected bond lengths in Table 5.2 testifies indeed drastic structural changes, to which we assign the major responsibility of the drastic dependency of the energetics on the super-cell-size. Similar to

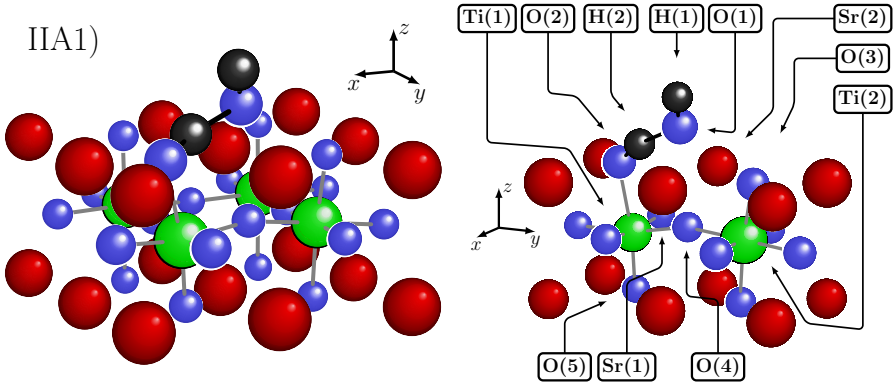

Figure 5.1: Schematic illustration of the equilibrium configuration of the adsorbed water molecule on the SrO termination. Color code: Big red (dark) spheres: strontium, big green (bright) spheres: titanium small blue (bright) spheres: oxygen, small black spheres: hydrogen.

the case of the oxygen ad-atom, the structural deformations are more pronounced in the vertical than in the lateral direction. The distance of the lattice oxygen atom at the adsorption site to the subsurface titanium atom O(2)–Ti(1) is elongated by almost 19 % upon adsorption, while the bond to the underlying oxygen atom in the third layer O(5)–Ti(1) shrinks simultaneously about 25%. This strong deformation perpendicular to the surface in combination with the smaller stretching and tilting of the oxygen-titanium bonds in the second layer indicates the deformation and tilting of the respective TiO_6 octahedron below the adsorption site, which is contrasted by the virtually unchanged position of the strontium atoms in the topmost layer.

The actual adsorption process is looked upon more closely in Figure 5.2 with plotting the energy, the relevant internal bond length of the water molecule and the change of the Hirshfeld-charges [165] as a function of the water molecule's distance to the surface. The absence of extrema in the energy graph shows that the water molecule decomposes without any energetic barrier. Therefore, a precursor molecular adsorption state on this termination as found by Evarestov *et al.* [34] with same binding energy as the corresponding configuration IIA1 on (1×1) surface models can not be confirmed. As the increase of the bond length O(1)–H(2) indicates in the middle panel of Figure 5.2, the actual decomposition take place when the water molecule has approached the surface smaller to a distance smaller than 0.5 Å. At this position also the essential part of the charge transfer from the surface to water molecule sets in, which comprises mostly the contributions of the individual the atoms O(2) and the subsurface Ti(1) at the adsorption site. Interestingly, the charge density close to the adjacent cations Sr(1) and Sr(2) is nearly unchanged during the entire process. This Hirshfeld-charge transfer is in line with the picture of water acting as a Lewis-acid and the surface playing the role of a Lewis-base, which is commonly expected for dissociative adsorption of water [231, 232]. We mention, that we avoid here the usual terminology of Lewis acid and base "sites", because the detailed Hirshfeld-analysis showed that the charge density located around the oxygen and titanium atoms is modified to some minor extent in the entire two surface layers.

Then, having finally arrived at the ground state position IIA1 shown in Figure 5.1 the hy-

Table 5.2: Characteristic bond lengths in the ground state configuration (IIA1) of the adsorbed water molecule on the SrO-termination. The quantity Δd denotes the change in percent of the respective bond due to adsorption of the H_2O-molecule. The atomic labeling is defined in Figure 5.1.

IIA1	$d\,[\text{Å}]$	$\Delta d\,[\%]$		$d\,[\text{Å}]$	$\Delta d\,[\%]$
H(1) — O(1)	0.97	-1	O(1) — O(3)	3.04	—
H(2) — O(1)	1.60	+60	O(2) — Sr(1)	3.24	+12
H(2) — O(2)	1.01	+ 2	O(2) — Sr(2)	3.20	+3
H(2) — O(2)	1.01	—	O(2) — Ti(1)	2.28	+19
O(1) — Sr(1)	2.59	—	O(4) — Ti(2)	2.04	+6
O(1) — Sr(2)	2.55	—	Ti(1) — O(5)	1.82	-25

drogen atom H(2) is split off the water molecule and forms a hydroxyl-group with the surface lattice oxygen atom O(2). The topmost hydroxyl-group O(1)H(1) is stabilized essentially by the electrostatic attraction to the adjacent Sr(1) and Sr(2) cations and the hydrogen bond O(1)–H(2), measuring 1.6 Å and emphasizing the persistent interrelation of the two hydroxyl-groups on the surface. Atomic arrangements, where two hydroxyl-groups form an entity by means of such a hydrogen-bond have also been reported recently for the water adsorption on the (001)-surface of the alkaline-oxides MgO and BaO [233] and points therefore at a possibly general feature of oxide surface with the similar geometry. Therefore, we adopt the nomenclature of the latter study and refer to the two hydroxyl-groups in Figure 5.1 as "ion-pair" or "hydroxyl-pair". Interestingly, the position of the topmost hydroxyl's oxygen atom is very close to the oxygen's position in the assumed continued perovskite lattice, whereas the results in Chapter 4 showed that the singly adsorbed oxygen atom forms a covalent oxygen-oxygen bond on the surface.

5.1.2 TiO_2 termination

In agreement with the preceding works [34, 35, 230] we find that water molecules may adsorb on the TiO_2 termination without dissociation assuming configuration IIB1 depicted in Figure 5.3. The increase of the binding energy up to approximately -0.73 eV in (2×2) and (3×3) surface models is traced back to the attractive interaction of the intact water molecule with its periodic image in the case of the small (1×1) surface models. Obviously, this non-dissociative adsorption mode does not inflict larger lattice distortions, being illustrated by the only very subtle changes of the bond lengths due to adsorption in Table 5.3 and which is also reflected in the binding energies listed in Table 5.1 being practically constant with respect to the number of atomic layers in the surface model.

The binding to the surface is driven by the electrostatic attraction of the surface Ti(1) atom and the oxygen atom O(1) of the water molecule as well as between the surface oxygen atom O(2) and the hydrogen atom H(2). In addition, Figure 5.4 displays that the adsorption process is accompanied by a transfer of charge density, most notably from the proximity of H(2) into the region of the bond O(1)–Ti(1), while the electronic density near H(1) remains virtually un-

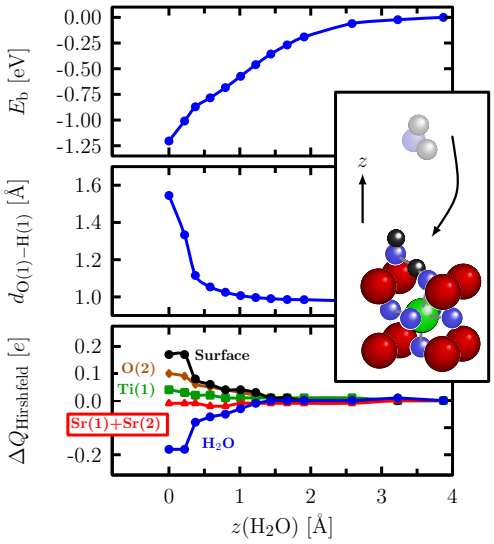

Figure 5.2: Energy, internal bond length. and change of the Hirshfeld charges as a function of the z-coordinate of the water molecule's center of mass. The latter quantity is referenced to their respective values prior to adsorption. The data plotted here has been obtained from a seven layer (2×2)-surface model with constraint geometry optimizations for the individual values of $z(H_2O)$. The atomic labeling is defined in Figure 5.1.

changed. The non-equivalent electronic states of the two hydrogen atoms is also reflected in the very different distances to their respective neighboring surface oxygen atoms (cf. O(2) – H(2), O(3) – H(1) in Table 5.3). Applying the Hirshfeld charge partitioning scheme [165] allows the interpretation of the charge accumulation between Ti(1) and O(1) during the adsorption as a small effective charge transfer from the water molecule to the surface, illustrated in Figure 5.6 on the left side by the simultaneous converse change of the individual Hirshfeld-charges as a function of the water molecule's distance to the surface. Thus, the assignment of the water molecule as a the Lewis acid and the surface as a Lewis base is obviously reverted here with respect to the previously discussed adsorption on the SrO termination.

Table 5.3: Characteristic bond lengths in the ground state non-dissociated configuration (IIB1) of the adsorbed water molecule on the TiO_2 termination. The quantity Δd denotes the change in percent of the respective bond due to adsorption of the H_2O-molecule. The atomic labeling is defined in Figure 5.3.

IIB1	d [Å]	Δd [%]		d [Å]	Δd [%]
H(1) — O(1)	0.98	-1	Ti(1) — O(1)	2.21	–
H(2) — O(1)	1.01	+2	Ti(1) — O(2)	2.24	+8
H(2) — O(2)	1.73	–	Ti(1) — O(4)	1.81	-2
H(1) — O(3)	2.85	–	Ti(1) — O(5)	1.94	+5

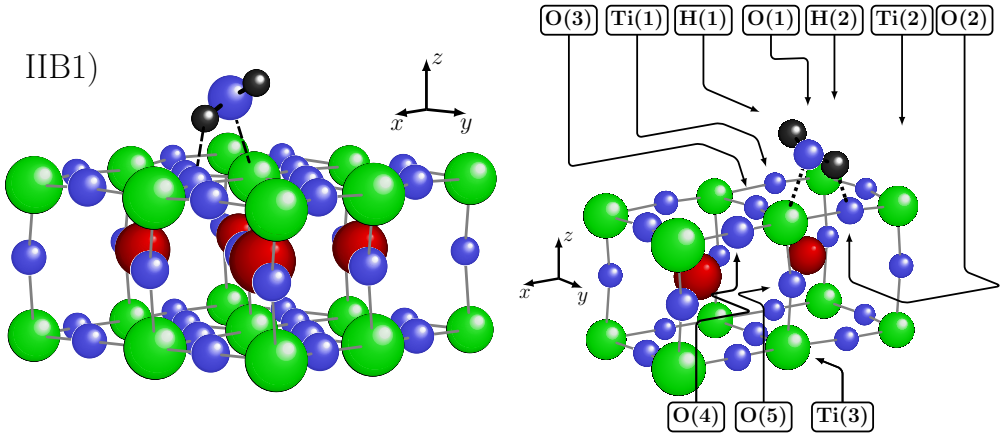

Figure 5.3: Schematic illustration of the adsorbed water molecule on the TiO_2 termination in the non-dissociated state (IIB1). Color code: Big red (dark) spheres: strontium, big green (bright) spheres: titanium small blue (bright) spheres: oxygen, small black spheres: hydrogen.

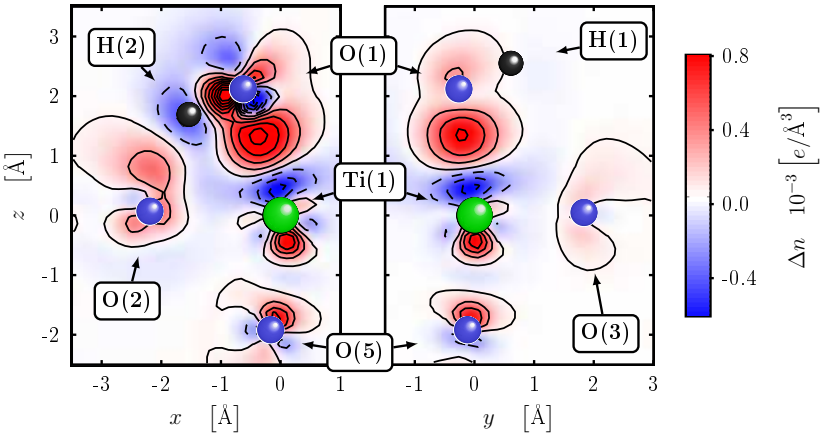

Figure 5.4: Charge density difference $\Delta n(\mathbf{r})$ of the molecularly adsorbed H_2O on the TiO_2 termination surface, which has been calculated here analogously to Section 4.2. The charge accumulation between the water molecules' oxygen atom and the surface Ti(1) is clearly visible in both planes. The atomic labeling is the same as in Figure 5.3.

As shown forward below, boosting of the strength of bond Ti(1)–O(1) on the expense of the oxygen-hydrogen bond O(1)–H(2) promotes the disintegration of the water molecule substantially. The resulting configuration IIB2 is presented in Figure 5.5 and displays unsurprisingly the formation of two hydroxyl-groups. The oxygen atom of the topmost hydroxyl O(1)H(1) is directly coordinated to the surface titanium atom Ti(1) with a distance of 1.84 Å, which is even shorter than the titanium oxygen bond length in bulk $SrTiO_3$ suggesting thereby a quite substantial gain in bond strength between these two atoms. The axis of the topmost hydroxyl-group and the bond O(1)–Ti(1) enclose an angle of 120° such that it lies approximately in the plane defined by the titanium atom Ti(1), the adjacent surface lattice oxygen atom O(3), and the vector normal to the surface. The second hydroxyl-group is formed by the split-off hydrogen atom and the surface oxygen atom O(2) such that its axis is approximately parallel to the axis of the topmost hydroxyl-group O(1)H(1), i. e. it is also tilted about 120° with respect to the z-direction.

This configuration IIB2 is energetically favored over the molecularly adsorption configuration IIB1 for surface models comprising more than (2×2) surface unit cells, because here the lateral relaxations in the topmost layer can properly develop. Table 5.4 quantifies these distortions further, of which the lifting of the Ti(1) towards the vacuum and the increase of the bond Ti(1)–O(2) by approximately 20% are the most prominent ones. The latter seems to originate from the coulomb repulsion of the two hydroxyl-groups.

Similar to the case of the oxygen ad-atom and in contrast to the water adsorption on the SrO termination, the induced lattice deformations have a rather a lateral than a perpendicular character, which is also reflected in faster convergence of the binding energy with respect to the number of atomic layers as seen already in Table 5.1. For the sake of completeness we remark that the topmost hydroxyl-group O(1)H(1) in Figure 5.5 may be rotated 180° about the z-axis resulting in a slightly different yet energetically equivalent geometry making a further distinction unnecessary.

Intuitively, the configuration IIB2 may only be achieved, if the water molecule in IIB2 dissociates. This dissociation process is analyzed in greater detail in Figure 5.6 on the right side. The obtained minimum energy path (MEP) of this reaction was calculated using "nudged-elastic-band" (NEB)-method [234] in the implementation of the "Atomic Simulation Environment" (ASE) [235]. In order to guarantee the dilute limit, a (3×3) surface model with seven unit cells with seven atomic layers was employed. Checking the equivalent MEPs of in (2×2)-surface models for different numbers of atomic layers verified that the thickness of the slab model affects only marginally the interesting dissociation barrier. As reaction coordinate for the MEPs shown in Figure 5.6 and forward below, we used the path in the hyper-dimensional space spanned by the all atomic coordinates, which were scaled with the square root of the respective mass. For the sake of clarity, we normalized the shown path lengths to unity.

From the presented energy profile a dissociation barrier of only 90 meV is derived. This value is approximately half of the value given by Lin *et al.*, which we have reproduced before when using equivalent geometry set-ups with (2×2) surface models [230]. This small energetic barrier renders the molecular adsorption geometry IIB1 for coverages lower than 0.25 ML even at lowest temperatures extraordinary short-lived at low coverages. Analyzing the change of the Hirshfeld-charges suggests the interpretation of an effective charge transfer to the adsorbed species during the dissociation process, especially to the topmost hydroxyl-group O(1)H(1), whereas the Hirshfeld-charge of Ti(1) is does not differ between the initial IIB1 and finally

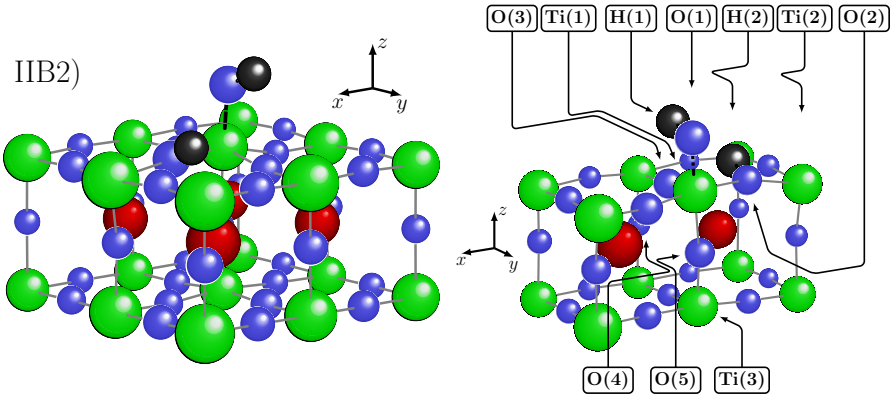

Figure 5.5: Schematic illustration of the adsorbed water molecule on the TiO_2 termination in the dissociated state (IIB2). Color code: Big red (dark) spheres: strontium, big green (bright) spheres: titanium small blue (bright) spheres: oxygen, small black spheres: hydrogen.

Table 5.4: Characteristic bond lengths in the dissociated ground state configuration (IIB2) of the adsorbed water molecule on the TiO_2 termination. The quantity Δd denotes the change in percent of the respective bond due to adsorption of the H_2O-molecule. The atomic labeling is defined in Figure 5.5.

IIB2	d [Å]	Δd [%]		d [Å]	Δd [%]
H(1) — O(1)	0.98	-1	Ti(1) — O(2)	2.24	+21
H(2) — O(2)	0.98	-1	Ti(1) — O(3)	2.17	+3
H(1) — O(3)	2.84	–	Ti(1) — O(5)	2.29	+24
H(2) — O(3)	2.34	–	Ti(2) — O(2)	2.08	+12
Ti(1) — O(1)	1.84	–	Ti(3) — O(5)	1.86	-7

dissociated state IIB2. The transferred electron density is supplied predominantly by the adjacent lattice oxygen atom O(2), but similarly to the adsorption process on the TiO_2 termination all substrate ions contribute to some extent. This is in line with the reduction of the energy barrier for smaller coverages. Assuming that the absolute amount of transferred charge being necessary to triggering the dissociation is independent of the water coverage and for each molecule the same, at lower coverages the surface atoms in the vicinity of the adsorption site have to provide individually less charge at low densities than at dense packings. Thus, at lower coverages the electronic structure of the surface gets less perturbed by the dissociation of the molecule, which becomes therefore more likely.

It is noteworthy that a recent DFT-study confirmed the existence of the same adsorption configurations on $BaTiO_3$, although it is unfortunately likewise the aforementioned preceding studies for $SrTiO_3$ confined to most likely to too small model systems [236]. With background of the data in Table 5.1, the conclusions drawn from the energetics of the water molecule on $BaTiO_3$ can not be unconditionally trusted, however, apparently the substitution of the Sr with the Ba atom seems to boost the relative stability of the corresponding dissociated configuration

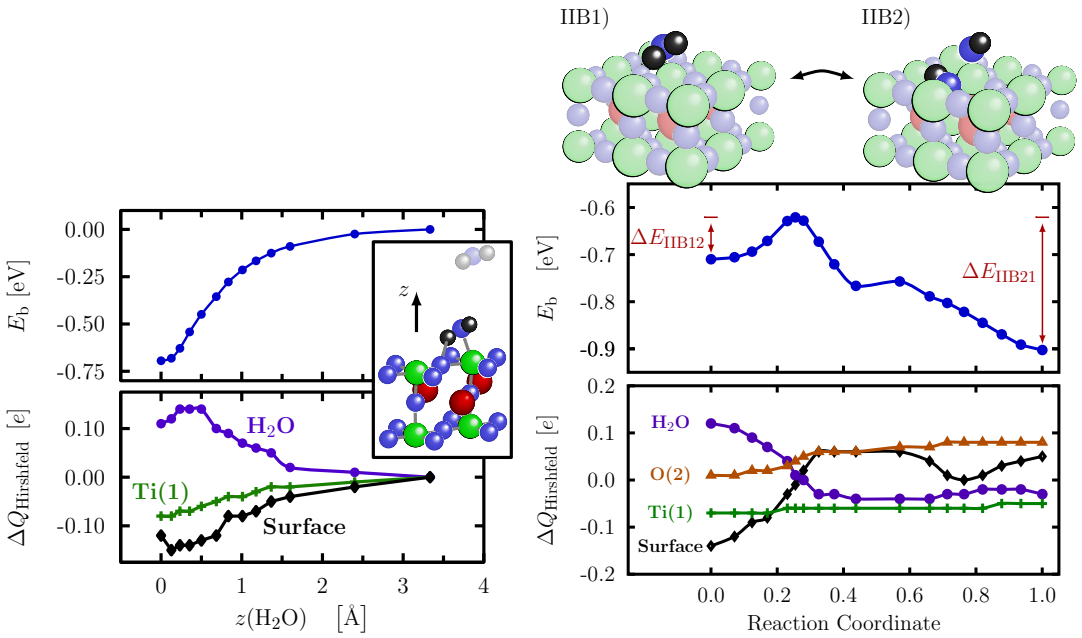

Figure 5.6: Left side: Binding energy and charge rearrangement of the water molecule, the Ti(1) atom as well as the entire topmost surface layer as a function of the z coordinate of the water molecule's center of mass during adsorption on the TiO_2-termination. Right side: Binding energy and charge rearrangement of the water molecule during the ensuing dissociation on the TiO_2 termination. The bottom panel displays the change of the Hirshfeld-charges of the entire water molecule, of the adjacent Ti(1) and O(2) atoms as well as the entire surface during the dissociation. On both sides. the charges have been referenced to their value prior to adsorption. In order to save computational resources, the data presented in the left and right panel has been calculated using seven layer surface models comprising (2×2) and (3×3) surface unit cells, respectively. The atomic labeling is defined in Figure 5.3.

IIB2 with respect to IIB1. We also mention here that the picture of the coverage dependent adsorption mode water adsorption on the TiO_2 is very reminiscent to the situation found for the α-$Al_2O_3(0001)$ surface, where first principles studies also predict the initial molecular water adsorption at the surface cation followed at lower water coverages by the molecules' dissociation thanks to a negligible energetic barrier [237, 238].

5.2 Thermodynamic stability

For the analysis of the thermodynamic stability the formalism developed in Section 4.3 has to be extended. The inclusion of hydrogen atoms in the system can be accounted for simply by adding an appropriate term to Eq. (4.13):

$$\gamma = \Phi - \Gamma_{Sr}\Delta\mu_{Sr} - \Gamma_{Ti}\Delta\mu_{O} - \Gamma_{H}\Delta\mu_{H} \tag{5.2}$$

where μ_H is the atomic hydrogen chemical, which can be calculated in the same way as for the of oxygen in Eq. (4.20) and Eq. (4.24). Because hydrogen is not contained in the employed reference bulk system of ideal perovskite $SrTiO_3$, Γ_H is here basically the number of hydrogen atoms in the surface model. This reference is of course no longer reliable if the sample contains already hydrogen impurities to a large extent. However, at this point we are primarily interested in the adsorption on pristine $SrTiO_3$ and we will therefore not pursue in this direction any further.

5.2.1 Water chemical potential

In principle, the last equation would be completely sufficient to explore the relative stability of the atomic conformations discussed in Section 5.1. However, in the following paragraphs we consider the adsorption of whole water molecules and therefore it is more instructive to use water vapor as the source and reference for hydrogen atoms in the gas phase. In equilibrium the chemical potential of water should be the stoichiometric combination of the chemical potentials of gas phase oxygen and gas phase hydrogen:

$$\mu_{H_2O} = 2\mu_H + \mu_O \quad . \tag{5.3}$$

As above in Section 4.3, both μ_O and μ_H are normalized to one atom. Defining now the difference chemical potential for water in full analogy to Eq. (4.11) and in combination with the dissociation energy $E_{Dis(H_2O}$ of the water molecule in the gas phase:

$$E_{Dis}(H_2O) = E^{Gas}_{H_2O} - E^{Gas}_{H_2} - E^{Gas}_{O} \quad , \tag{5.4}$$

we are able to rewrite the important surface formation energy referenced to water vapor instead of hydrogen gas:

$$\gamma = \Phi - \Gamma_{Sr}\Delta\mu_{Sr} - \Delta\mu_{O}\left[\Gamma_O - \frac{1}{2}\Gamma_H\right] - \frac{1}{2}\Gamma_H\left[\Delta\mu_{H_2O} + E_{Dis}(H_2O)\right] \quad . \tag{5.5}$$

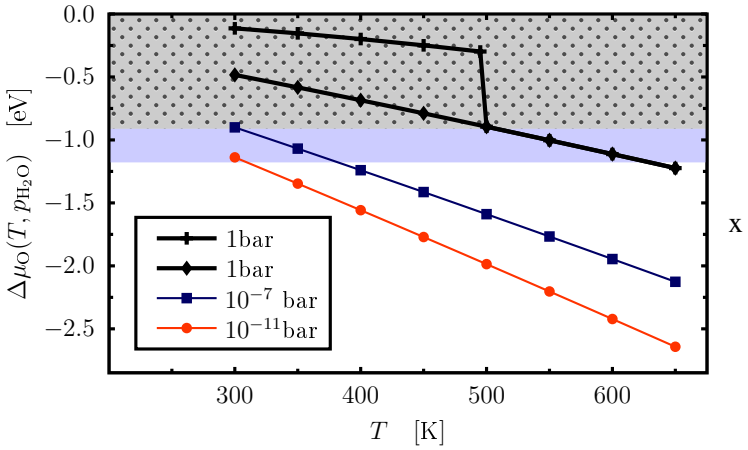

Figure 5.7: Difference chemical potential of water $\Delta\mu_{H_2O}$ as a function of temperature for different pressures calculated using the tabulated experimental measure thermodynamics quantities from Ref [223]. The gray freckled and the plain blue box mark the high-pressure region above the critical point of water and the range of $\Delta\mu_{H_2O}$ scanned in the experiment of Iwahori *et al.*, respectively (see forward below). The black thick lines denote $\Delta\mu_{H_2O}$ at the reference pressure, firstly for the physically correct parameterization ("+") exhibiting the phase transition with the discontinuity at 500 K and secondly for the gas phase parameterization extrapolated to temperatures below 500 K (diamonds). Focusing primarily on the low-pressure region, the latter was used throughout to calculate $\Delta\mu_{H_2O}$ in following.

The calculation of the dissociation energy $E_{Dis}(H_2O)$ is presented in Appendix B. The change for the factor of $\Delta\mu_O$ is due to the oxygen atom of the water molecule. Upon adsorption of two hydrogen atoms, one oxygen atom is delivered to the surface without any additional energetic expense, i. e. it comes "for free". In turn, removing this oxygen atom from the surface requires then an effective lowering of the partial oxygen pressure in the ambient gas atmosphere.

The essential problem with using water vapor as reference is that it might well exist in relevant condition in condensed and vapor form. It is obvious that such a simple relation like Eq. (5.5) and the crude approximations made in its derivation in Section 4.3 do not account for this properly. The exclusion of condensed water is guaranteed, if the $\Delta\mu_{H_2O}$ takes values smaller than the critical difference chemical potential $\Delta\mu^{Crit}_{H_2O} = -0.91$ eV corresponding to the critical point of water [239]. Consequently, this will define the range of $\Delta\mu_{H_2O}$ for the strict applicability of Eq. (5.5) and we may calculate $\Delta\mu_{H_2O}$ using the data taken from the thermo-chemical tables [223] in combination with Eq. (4.24). Of course, in the latter formula the factor of 1/2 has to be omitted, because it reflects only that oxygen is a diatomic species. Conventionally, the data in the thermo-chemical tables was measured as a function of temperature at atmospheric pressure. For water this yields the well known liquid-gas phase transition at $\approx 500°C$, which is indicated by the discontinuity of the entropy, enthalpy and eventually $\Delta\mu_{H_2O}$ presented in Figure 5.7. Restricting ourselves to the gas phase of water, will we avoid the ambiguity by using only the parameterization for the gas phase, which will also be valid for lower temperatures and pressures below atmospheric pressure.

Before proceeding, we note that the neglect of vibrionic contributions to the surface formation

energy in presence of OH-bonds may be indeed be a serious approximation [239]. However, we do not incorporate them for the reasons given in Section 4.3 and because we are interested primarily in low coverages of adsorbed water species, such that the vibrionic contribution will be rather small anyway. In contrast, focusing on the precise description of very high coverages, these entropic terms can be expected to play a much more important role and should definitely be taken into account.

5.2.2 Comparison to the experiment

Interestingly, the hydroxilation of $SrTiO_3$ in this low-pressure regime has also been probed by a recent experiment conducted by Iwahori *et al.* [38]. They explored the $SrTiO_3$ surface using the FFM-technique, allowing the to monitor the change of the friction force upon water exposure specifically for differently terminated domains on their samples.

In order to prepare the surface, Iwahori *et al.* annealed their samples after initial cleaning for 2 h in oxygen ambient at 1000°C. This produces quasi defect-free surfaces of single atomic steps and atomically flat terraces, which can be distinguished by their different width and the different friction force they exert on the tip. The narrower terraces showing larger friction forces are assumed to be the SrO terminated domains, whereas the wider terraces with smaller forces are identified with the TiO_2 terminated regions. The correctness of this assignment was verified in earlier experiments [240, 241]. The actual AFM/FFM scans were carried out at room temperature at a nominal partial water pressures of 10^{-6} Pa up to 10^{-2} Pa, which translates exactly into the range of $\Delta\mu_{H_2O}$ being accessible with the first-principles thermodynamics formalism. Iwahori *et al.* were thus able to monitor the friction force for the two differently terminated domains separately as a function of partial water pressure and consequently their work has be considered as a key experiment regarding the interaction of water with $SrTiO_3$. On the SrO terminated domains they observed an increase of the friction force with the partial water pressure, indicating the hydroxilation of these areas. Contrariwise, no remarkable change of the frictional force was observed on the TiO_2 terminated domains for the whole investigated pressure range, strongly suggesting that water molecules can not be stabilized on these areas on these ambient conditions. In Figure 5.8 we compare directly the experimental result to the adsorption free energies computed straightforward by insertion of the energetics obtained in Section 5.1 into Eq. (5.5). The qualitative and also the quantitative agreement is noteworthy. Our calculation predict indeed the hydroxylation on the SrO terminated surface at even a lower humidity Iwahori *et al.* were able to probe in their measurements. Keeping in mind that the FFM-technique is especially sensitive towards organic and aqueous species, our results are in line with the interpretation that the increased friction force measured on the nominally clean surface on the SrO terminated domains is indeed due to residual hydroxyl-pairs on these areas. In contrast, our results indicate that on the TiO_2 termination water molecules can be stabilized only at increased partial water pressures. The respective threshold chemical potential for the water adsorption here lies less than 100 meV below the $\mu^{\mathrm{Crit}}_{H_2O}$, marking the upper bound of the low-pressure regime. We recall that 100 meV is certainly within the range of systematic errors due to the approximation made in the description of the underlying electronic structure. In addition, in the range of $\Delta\mu_{H_2O} \approx -1.0 \cdots -0.91$ eV the actual adsorption free energies for the small coverages are hard to distinguish from that of the clean TiO_2 terminated surface. Therefore, we consider also for the case of the TiO_2 termination

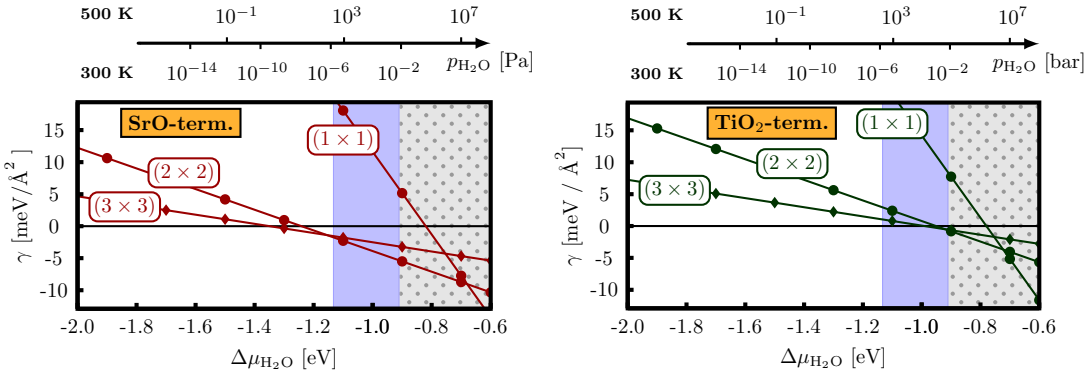

Figure 5.8: Adsorption free energy as a function of the water difference chemical potential $\Delta\mu_{H_2O}$ for different coverages of adsorbed H_2O species on both terminations. The data has been referenced to the respective regular termination, which eliminates the dependence on the $\Delta\mu_{Sr}$ and $\Delta\mu_O$ in Eq. (5.5). Thus, the adsorption free energies only smaller than zero denote water adsorption. As in Figure 5.7, the plain blue background box marks the range explored by Iwahori *et al.*, whereas the gray freckled background box marks the region above the critical point of water.

our results are in excellent agreement with the experimentally measured date.

Apparently very high packings of water molecules on both terminations can not be achieved within the low-pressure regime. Moreover, Figure 5.8 illustrates nicely that reproducing the experimentally observed different water affinities of both termination requires the careful elimination of effects due to the finite size of the surface model. Similar to the case of atomic oxygen in Chapter 5, the more sophisticated treatment of the underlying electronic structure as performed by Evarestov *et al.* does not allow to make contact to experimental observations, if the energetics can not be converged with respect to the super-cell size [34].

In addition to Iwahori *et al.*'s experiment, Kato *et al.* carried out a complementary FFM-study, focusing on the water adsorption on $SrTiO_3(001)$ at room temperature in the high pressure regime [242]. The essential observation is a drastic increase of the friction force at 10^3 Pa which is being attributed to an increased water reactivity. Converting this data again to the difference chemical potential, we obtain $\Delta = -0.6$ eV, which is intriguingly only about 0.1 eV above the difference chemical potential where our calculated energetics would predict the stabilization of the one mono-layer water coverages for both terminations. Note that this situation corresponds to a steady coexistence of dissociated and intact water molecules on the surface at rather high packings, whereas in Iwahori *et al.*'s experiment we would expect only a very few dissociated water molecules on the TiO_2 terminated domains. Stipulating that the concept of the difference chemical potential is still somehow valid beyond the critical point of water and the observed increased reactivity and proposed formation of an liquid water over-layer is the actually monitored with the force friction, our results are also fully consistent with Kato *et al.*'s observations.

5.2.3 Global phase diagram

It is possible to extend the analysis of the global thermodynamic stability in Section 4.3 with respect to the water chemical potential in Eq. (5.5) and derive a phase diagram analog to the one shown Figure 4.6. With the same arguments as in Section 4.3 we have to define the upper and lower limits for the stability of $SrTiO_3$ with respect to $\Delta\mu_{H_2O}$. Because our reference was chosen to be pure $SrTiO_3$, the range $\Delta\mu_{H_2O}$ extends to negative infinity,denoting the complete absence of water in the thermodynamic system. Since we want to restrict this analysis to the low-pressure regime below the critical point, the upper boundary of $\Delta\mu_{H_2O}$ is still $\Delta\mu_{H_2O}^{Crit} = -0.91$ eV. There are several forms of multiple hydrated strontium hydroxides known [243], we expect in the strontium-rich and water-rich regime the crystallization of these. Intuitively, these partly highly multiply hydrated compounds such as the recently studied strontium hydroxide octahydrate $Sr(OH)_2 \cdot 8H_2O$ [244, 245], are expected to form only under extreme water-rich conditions. Since we address here only the low-pressure regime of water, it would be sufficient to restrict ourselves only to the non-hydrated strontium oxide $Sr(OH)_2$. However, because its structure is not known completely from experiment [246], we have to determine the energetically minimum structure, which is explained in detail in Appendix A. We also included strontium hydroxide monohydrate $Sr(OH)_2 \cdot H_2O$ as an additional upper limit in the strontium- and water-rich limit, because all atomic positions of this material are tabulated [247, 248]. These additional limits for the chemical difference potentials are expressed similar to Eq. (4.26) in the following inequalities, which have to be fulfilled by the chemical difference potentials:

$$G_{Sr(OH)_2} > \mu_{Sr} + \mu_{H_2O} + \mu_O \tag{5.6}$$

$$G_{Sr(OH)_2 \cdot H_2O} > \mu_{Sr} + 2\mu_{H_2O} + \mu_O \quad . \tag{5.7}$$

Because of the numerous OH-bonds in these materials the vibrionic entropy forms certainly a substantial contribution to the Gibbs free energies on the left hand side. However, we are interested here in a coarse estimate of the stability of $SrTiO_3$ and a high quality description is of these materials is therefore beyond the scope of this work. Thus, $G_{Sr(OH)_2}$ and $G_{Sr(OH)_2 \cdot H_2O}$ are again approximated only with the respective total energies.

Contrariwise, in the titanium-rich region in the phase diagram, we do not consider a further destabilization of the $SrTiO_3$ due to precipitation of a hypothesized "titanium hydroxide", even if such a material existed at all. We have seen in Figure 5.8 and from Iwahori *et al.*'s experiment that water molecules practically do not adsorb on the TiO_2 terminated surface for water chemical potentials below the critical point. Thus, we may expect that titanium dioxide will precipitate on the sample independently humidity in the environment, unless the condition expressed in Eq. (4.25) holds.

Apparently, the addition of water to thermodynamic system requires the addition of a third coordinate axis to the two dimensional phase diagram shown and discussed in Section 4.3. Due to the comprehensible difficulties of visualizing such a three dimensional phase diagram properly, we restrict ourselves in Figure 5.9 to show the projection on the plane corresponding to $\Delta\mu_O = -1.5$ eV. Inspection of Figure 4.6 reveals that this belongs to the broad region of oxygen difference potential $\Delta\mu_O$ from -1.8 eV to -0.4 eV where $SrTiO_3$ is stable. Possible modifications will only arise for extreme "oxygen-rich" or "oxygen-poor" conditions. In addition, we do not

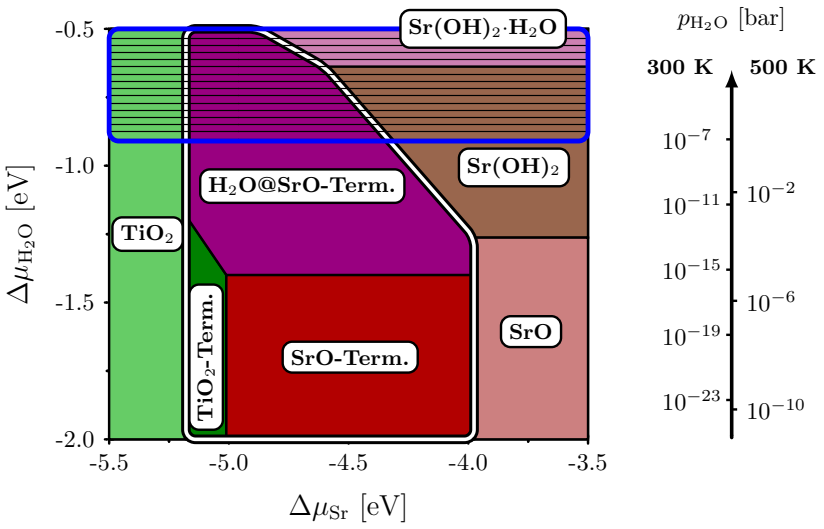

Figure 5.9: Phase diagram of the $SrTiO_3(001)$-surface upon exposure to water vapor for the oxygen difference potential of $\Delta\mu_O = -1.5$ eV. The encircled area marks the stable region of $SrTiO_3$. The region beyond the critical point of water is marked here with blue horizontal lines.

address here adsorption geometries comprising different mixtures of one or more Ti-, Sr-, O- and H-ad-atoms, such that the shape of Eq. (5.5) indicates already that the lines separating the different regions of stability will be parallel and perpendicular to the axes of the variables $\Delta\mu_{Sr}$ and $\Delta\mu_O$. Of course, the precipitation surface of the oxides in the full three dimensional phase diagram is not collinear with the respect to the $\Delta\mu_O$-axis, but so is the region of stability of $SrTiO_3$. Thus, the relative position of the phase boundaries of for of $Sr(OH)_2$, $Sr(OH)_2 \cdot H_2O$ and $SrTiO_3$ do not change in this range of medium oxygen chemical potentials and plotting Figure 5.9 will differ only in the numerical values of $\Delta\mu_{Sr}$. Because the latter is used only as an adjustable parameter anyway, this two dimensional projection provides already the same information as the full three dimensional phase diagram for the structures under consideration.

A noteworthy feature of this phase diagram presented in Figure 5.9 is the further destabilization of the TiO_2 termination. In the global thermodynamic equilibrium, this termination would exist at room temperature only in extremely dry conditions. Because water and hydrogen can realistically never be really eliminated and the TiO_2 termination or Ti-rich surfaces are frequently prepared in experiment, this phase diagram corroborates our earlier surmise that the actual surface morphology is crucially dependent on probably complex reaction pathways, which may be blocked or opened under different conditions in the ambient of the sample. However, a complete picture of the $SrTiO_3(001)$ surface would comprise these reaction paths and would hopefully reproduce many of the observed surface formations is certainly out of reach. On the other hand, if the way to precise thermodynamics equilibrium is blocked by insurmountable energetic barriers, we may treat each of those formation and reconstructions in local equilibrium, which eventually justifies the approach in the previous section.

5.3 Relation to further experiments

In the previous Section we have demonstrated by applying fundamental thermodynamic arguments that our results can rationalize the different affinity of the two terminations towards water, which has been explicitly observed Iwahori *et al.*'s experiment. For the sake of completeness we will now briefly report about further experiments subjected to the interaction of water and $SrTiO_3$, using techniques other than the AFM and FFM. If it is appropriate, we will also try to rationalize these observations in order to strengthen the validity of the picture of the water adsorption on $SrTiO_3$ provided by the result in Section 5.1.

Temperature-programmed desorption

Temperature programmed desorption (TPD) or temperature programmed reaction (TPR) is a useful tool to study experimentally the kinetics of surface processes [249]. Before recording such a TPD-spectrum, the gas or the mixture of gases is dosed in defined quantities to the surface, which has been cooled down to low temperatures beforehand allowing thereby the adsorption of even weakly bonded species in adjustable coverages. Subsequent heating of the sample with a constant heating rate activates possibly complex surface reactions which may be accompanied with the desorption of one or more of its products. Analyzing the kind as well as the number of evaporated species in dependence of the temperature of the sample for different initial coverages allows then to record the temperature desorption spectrum, i. e. the desorption rate of the individual species as a function of temperature. The position and shape of the peaks in this spectrum yields eventually detailed information about the kinetics of these reactions on the surface [249, 250].

Wang *et al.* performed such a TPD-study addressing the interaction of water with the predominantly stoichiometric as well as with the sputtered, i. e. oxygen-reduced $SrTiO_3$ surfaces [37]. The presented TPD-spectra display a prominent peak at 160 K for very high exposures, which indicates the desorption of a weakly bonded second water or ice over-layer. The spectrum recorded from the nominally defect-free samples exhibits at the increased temperatures essentially two features. At low water exposures in the range of 0.05 L to 0.3 L and consequently at low coverages, a broadened feature extending from 200 K to 300 K is assigned to "chemisorbed molecular" water, whereas the clearly more pronounced peak appearing for higher exposures from 0.4 L to 1.5 L below 200 K is identified with "more weakly bound" water on the surface. Based on these results and referring to the surmises of previous experimental studies, the authors suggest non-dissociative water adsorption on the stoichiometric, non-defective $SrTiO_3(001)$-surfaces. Because of the well-developed (1×1)-LEED-patterns and the results obtained by Yoshimoto *et al.* [181] using a similar preparation procedure, the authors concluded, that their samples are predominantly TiO_2 terminated. On the other hand, referring to the works of Kawasaki *et al.* [178] and the theoretical study of Padilla and Vanderbilt [198], the authors admit to have also to some extent Sr-atoms at surface. Indeed, later and more refined theoretical studies [32, 33] as well as our own analysis in Section 4.3 disable the authors arguments and uncover that the exact surface morphology is largely unknown to the authors. Despite these uncertainties and although the authors admit that they were able to calibrate the usual relation between initial water exposure and resulting water coverage only approximately, the measured TPD-spectrum shown in Ref. [37] fits qualitatively quite well to our results. Manifestly, the

repulsive interaction of the adsorbed water molecules is displayed and which is also nicely reflected in the binding energies listed in Table 5.1 for both terminations. Using the approximate formula given by Redhead [250]:

$$\frac{E_A}{k_B T} = \ln\left(\frac{\nu_0 T}{\alpha}\right) - 3.64 \tag{5.8}$$

allows in a simplified, but convenient way the derivation of the approximate activation energy E_A for a desorption process from the temperature T of a peak maximum in the TPD-spectrum, if the frequency factor ν_0 and the heating rate α of the sample are known. In Wang *et al.*'s experiment the heating rate was 1 Ks^{-1} and the frequency factor is usually assumed to be in the order of $10^{13}s^{-1}$. Inserting instead a value of 10^{18} for the ratio $\frac{\nu_0}{\alpha}$ in Eq. (5.8) yields the activation energies of 0.74 eV and 0.97 eV for the measured peaks at 200 K and 260 K corresponding to 1.0 L and 0.05 L of initial water dosages, respectively. Intriguingly, these two values recover indeed the binding energies for the water molecule at the TiO_2 termination presented in Table 5.1, if we make use of the rule of thumb, that 1 L of water exposure corresponds to 1 ML coverage. Checking on the binding energy on the SrO termination for low coverages (-1.38 eV), we expect an additional peak in Wang *et al.*'s spectrum at approximately 370 K, which is clearly missing. These two indications are completely in line with Wang *et al.*s initial conjecture that their samples were indeed mostly TiO_2 terminated and would suggest in turn the identification of the "chemisorbed water" as the dissociated molecule shown in Figure 5.5.

High resolution electron energy loss spectroscopy

A method especially sensitive towards vibronic modes of adsorbed species on the surface is the high resolution electron energy loss spectroscopy (HREELS). Cox *et al.* [36] observed in their HREELS experiment at 100 K the immediate adsorption of water on $SrTiO_3(001)$. After initial cleaning and annealing in oxygen the samples were annealed in a hydrogen atmosphere of $1.3 \cdot 10^2$ Pa in order to induce carriers into the material. Subsequent UPS/XPS measurements confirmed uncontaminated, defect free $SrTiO_3(001)$-surfaces on the samples. Under 4 L water exposure, two peaks in the spectrum at 209 meV (1686 cm^{-1}) and 454 meV (3662 cm^{-1}), which are being identified with the symmetric bending and scissor frequencies of molecularly adsorbed water molecules. However, due to a "poor signal-to-noise ratio", the anti-symmetric stretch could not be detected. At higher exposures up to 114 L, a broadened loss feature indicates O-H-stretch modes, which is being assigned to the already formed ice over-layer. Confirmation for the non-dissociative adsorption of water is derived from the emergence of three peaks at 11 eV, 14 eV and 17 eV in the UPS spectrum and which are being identified with the a_1, b_1, and b_2 orbitals of the molecularly adsorbed water molecules on the surface. Presumably, this from other works differing assignment of the three water fingerprint states is most likely due to a different energy reference during recording the spectra.

Photo-emission spectroscopy

Ultraviolet and X-ray photo-emission spectroscopy (UPS/XPS) studies subjected to the adsorption of water at exposures ranging from 0.5 L up to reported extreme 10^8 L with stoichiometric, defective, i. e. ion-bombarded and stepped $SrTiO_3(001)$ surfaces and have been performed by Henrich *et al.* [251], Webb and Lichtensteiger [252], Eriksen *et al.* [253] and Owen *et al.* [254].

Because the second two works could demonstrate some limitations of the historically first attempt of Henrich *et al.* [251] on the subject and which were also later being acknowledged by one of the authors [1], we will be content with simply mentioning it. Webb and Lichtensteiger on the other hand studied only defective surfaces and although their interpretation differs, their results essentially agree with the findings of Eriksen *et al.* and Owen *et al.*, letting us concentrate primarily on the results of the latter works.

For the oxygen-annealed and thus nominally defect-free surfaces Eriksen *et al.*, observed two peaks emerging below the O $2p$ valence band at approximately 11 eV and 14 eV in the spectra after exposing the sample to 2 L of water. The authors assign these peaks to the a_1 and b_2-orbitals of molecular water, while the b_1-orbital is suspected to be hidden beneath the oxygen O $2p$ valence band of $SrTiO_3$. Consequently, they suggest pure molecular adsorption of water on this surface. For the defective surfaces the authors find essentially the same features at higher exposures of 10 L , except that the second peak at 14 eV is somewhat less pronounced than the first one at 11 eV. Moreover, upon heating up the sample the second peak disappears, which is taken as evidence for removing of the water molecules from the surface. The remaining first peak at 11 eV is now attributed to the σ-molecular orbitals of hydroxyl-groups on the surface, which coincide energetically with the a_1-orbitals of molecular water. This interpretation is significantly supported by the work of Owen *et al.* [254], who were able to resolve the UPS-spectra as well as the difference spectra at 150 K for even lower exposures of 0.5 L. We mention that problems due to the normalization of the original spectra, difference spectra may lead to misinterpretations, which has been criticized by Eriksen *et al.* as well as Webb and Lichtensteiger. However, due to the clearness of their figures we assume that the authors succeeded in overcoming these problems and we reproduce their recorded spectra of Owen *et al.* in Figure 5.10 on the right side. The $SrTiO_3$-samples were prepared by Ar^+-bombardment and subsequent annealing in oxygen atmosphere, which resulted in clean, unreconstructed surfaces. Unfortunately, the authors do not comment on the exact surface morphology, but we may assume that it is predominantly TiO_2 terminated such as reported by other studies using similar preparation procedures. The difference spectra for the planar surface shown in the bottom panel on the right side of Figure 5.10 as graph (b) displays essentially three peaks, which are agreeing with Eriksen *et al.* being directly assigned to the fingerprint states of the water molecule. For the stepped surface (same panel, graph (a)), the results correspond essentially to the of Eriksen *et al.* for the oxygen defective surface, i. e. only one feature below and one peak hidden beneath the O $2p$ valence band, being indicative for the presence of hydroxyls. By analyzing the calculated eigenvalue spectra of configuration (IIA1), (IIB1) and (IIB2) in Figure 5.10 on the left side, we are able to confirm this point of view. Summing up the obtained total electronic density of states projected onto the topmost two layers shall be taken as a coarse approximation for simulating a "clean" $SrTiO_3(001)$-surface, but with some uncertainty about the actual termination. The resulting projected density of states (PDOS) is shown in the right side of Figure 5.10 in panel (a), and exhibits clearly a first broadened feature right below the oxygen O $2p$-valence band and a second smaller peak approximately 3 eV further below. Looking at the contribution of only the hydroxyls of configuration (IIA1) and (IIB2) in panel (b) and (d) shows that their σ-orbitals contribute substantially to the to the first, broadened feature, but not to the second one. The pronounced splitting of the two hydroxyl-σ - peaks in panel (b) in case of the SrO termination reflects the qualitative diversity of the two specimen being bound together as the hydroxyl-pair

in configuration (IIA1). Contrariwise, the nearly degenerate peaks around -5 eV in panel (d) reproduce the similarity of the two hydroxyl-groups as ligands of the six-fold coordinated surface Ti-atom in configuration (IIB2) on the TiO_2 termination. Apparently, the π-orbitals of the hydroxyl overlap in both cases drastically with the O $2p$-bands, resulting in an extended features from -4 eV to $\sim$ -0.5 eV and making the difficulties mentioned by the other studies in resolving this feature in experimental practice quite comprehensible. Panel (e) and panel (f) in Figure 5.10 display the water projected DOS in configuration (IIB1) and the total density of states of the isolated water molecule. The assignment of the water fingerprint states is obvious, however, we note that the b_1 orbital is broadened, indicating that the bonding to the surface is mostly accomplished by its overlap with the O $2p$ band, which as also been suspected in earlier studies [36]. Panel (c) in Figure 5.10 shows the sum of the PDOS of the hydroxyls and the water molecules on the TiO_2 termination, i. e. basically the sum of the graphs in panel (d) and panel (e). The resulting graph demonstrates that in presence of water molecules, the spectrum needs to be recorded analyzed with an extreme, most likely unrealistically high precision in order to detect the contribution of the hydroxyl-groups, even for equal numbers of dissociated and intact water molecules. Obviously, the ratio of water molecules and hydroxyl groups on the surface controls the ratio of the height of the two peaks below the valence band. Turning back to the difference spectra of Owen *et al.* in bottom panel on the right side of Figure 5.10 for the planar surface, i. e. graph (b) we note that the three fingerprint states have a very different height. Because of the problems for the difference spectra and their overlap with the lattice O $2p$-band, we do not comment on the amplitude of the b_1-peak. Having in mind that this spectrum was recorded at relatively low exposures and low temperatures of only 150 K, is seem quite reasonable that intact and dissociated water molecules were simultaneously present on the surface. On the other hand, the effective equal height of the corresponding peaks in the spectra measured by Eriksen *et al.* at higher exposures of 2 L, supports indeed our surmise that the fraction of the intact and dissociated water molecules in this mixture should depend on the water coverage. Of course, the different height of the first peak in the spectrum measured by Owens *et al.* could also originate from hydroxylated SrO terminated domains on the $SrTiO_3$ sample, which would again be consistent with our results.

Thus, the absence of the second peak in spectrum below the valence band is therefore essential for detecting molecular water, and corroborate thereby the hydroxylation of the "clean" $SrTiO_3(111)$ surface reported by Ferrer and Somorjai [255]. Interestingly, Webb and Lichtensteiger mentioned that contemporary research grade oxygen contained 5 ppm water, which would explain the findings of Ferrer and Somorjai and which would also not only seriously hamper oxygen adsorption studies such as performed earlier by Henrich *et al.* [256].

In summary, focusing on rather high density of water molecules, the experimental studies mentioned here led to a prevalent notion, that water molecules would dissociate on $SrTiO_3(001)$ only at defects or step edges [257]. Because we could demonstrate in the last two sections full consistency of our results with actual data presented in these experimental studies, the picture of the interaction of water molecules with the $SrTiO_3(001)$ surface presented in Section 5.1 seems to makes an extension of those former interpretations necessary, namely that water molecules dissociate indeed on both terminations due to very small energetic barriers. Only at dense packings on the TiO_2 termination, OH-bonds are formed between neighboring water molecules, which are capable of stabilizing molecular adsorption mode. It is quite possible that in inter-

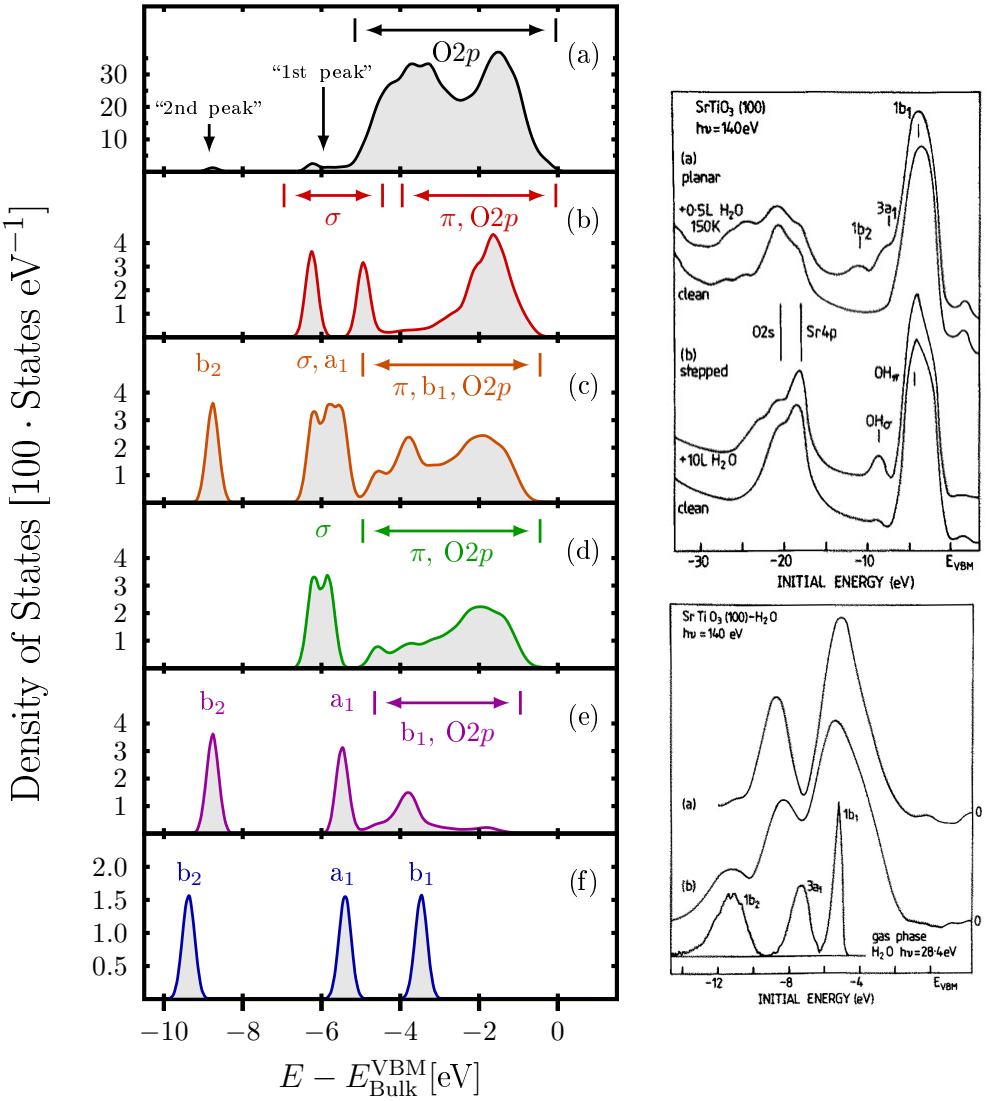

Figure 5.10: Left: Density of states of the adsorbed water molecule on the $SrTiO_3(001)$-surface. Panel (a): Sum of the PDOS of the topmost two layers of the configurations (IIA1), (IIB1) and (IIB2). Panel (b): PDOS of the hydroxyl-pair in configuration (IIA1). Panel (c): Sum of the PDOSs of the adsorbed water molecule in configuration (IIB1) and the two hydroxyls in (IIB2), which are being shown singly in panel (d) and panel (e), respectively. Panel (f): DOS of the isolated water molecule. The eigenvalue spectra have been convoluted with a Gaussian of 1.5 eV width and are referenced to the valence band maximum of the central layers of the slab model, being identified with the valence band maximum of the bulk crystal. The DOS for the isolated water molecule in panel (f) has been aligned at the a_1-peak with the PDOS of configuration (IIB1) in panel (e). Right: Top panel: UPS-spectra resulting from water adsorption on the planar (graph a) and stepped (graph b) surface. Bottom panel: The respective UPS-difference-spectra for the planar (graph b) and stepped (graph a). These figures were taken from Ref. [254].

mediate coverage regimes adsorption geometries become important, which comprise mixtures of hydroxyl-groups and water molecules such as the one Lin *et al.* [230] considered exemplary. Although the relevance of such mixed modes has been confirmed recently for the water adsorption for materials such as $Fe_3O_4(001)$ [258], α-$Al_2O_3(0001)$ [259] and TiO_2 [260] we do not address them here. The essential reason is that such adsorption geometries would be most likely stabilized only beyond the low-pressure regime which is actually hard to access reliably with the present methodology. The second reason is that for this intermediate coverage regime ranging from about 0.3 ML up to 1.0 ML the number of possible candidate configurations becomes indeed very large. Of course, in this regime it is not impossible that the water molecules and hydroxyl-groups exhibit an interesting interplay with each other and the underlying crystal lattice, such as for instance the recently discovered formation of pentagon-structured rows on Cu(110) by water molecules [261]. However, we have seen above that not only the binding energies of the adsorbate configurations but also the dissociation barrier exhibit a coverage dependence. Thus, in order to obtain a conclusive picture and to estimate the statistical relevance of each proposed configuration, most likely the MEP of very many reactions would have to be calculated. These would then serve as a basis to calculate the stationary and dynamical properties of the interacting water species in terms of a generalized Ising-model or time dependent statistical simulations [262, 263, 264, 265]. However, we feel that without at least a hint from the experimental side into that direction the substantial effort for such study is not justified, and we will restrict ourselves in the last section of this chapter to discuss the diffusion dynamics of the hydroxyl-groups in the dilute limit.

5.4 Diffusion of surface hydroxyls

As before, the low coverage limit will be established by employing surface models with (3×3) unit cells and one adsorbed H_2O species. In order to save computational time, we employed only seven atomic layers, which guarantee at least the qualitative correctness of the calculated MEPs as we explicitly checked in Section 5.1. The configurations IIA2-IIA5 and IIB3-IIB5 shown in Figure 5.11, Figure 5.13 and Figure 5.12 were calculated in independent geometry optimizations and subsequently connected by the MEP calculated as before employing the NEB-method.

5.4.1 SrO termination

For the decomposition of the adsorption geometry IIA1 shown in Figure 5.1, the motion of the protruding hydroxyl group O(1)H(1) has to be considered as the most likely step in order break the bond O(1)–H(2) and to disentangle thereby the hydroxyl-pair. Figure 5.11 shows the resulting configuration IIA2 and the corresponding energy profile. After having surmounted the substantial barrier $\Delta E_{\mathrm{IIA12}}$ of 0.94 eV, the hydroxyl's oxygen atom O(1) assumes in IIA2 a bridging position between two strontium atoms in the unit cell next to the original adsorption site, with the hydrogen atom H(1) pointing to its neighboring surface oxygen atom O(3). The further diffusion may now proceed through a reorientation of the hydroxyl-group to point away from its initial position in IIA1, resulting in configuration IIA3. The latter flip is connected with the negligible energetic barrier $\Delta E_{\mathrm{IIA23}}$ of only 0.08 eV and may be followed with an additional hop

to the next binding site, achieving eventually in configuration IIA4 the maximum distance to its initial position in IIA1, which can be accessed in a periodically continued (3×3) surface model. The last hop is accompanied with the intermediate energetic barrier $\Delta E_{\mathrm{IIA23}}$ of 0.41 eV, which may be regarded consequently as the rate limiting step for the diffusion of isolated hydroxyls on the SrO termination, because the binding energies of configurations IIA2, IIA3 and IIA3 are practically the practical identical binding energy of the identical and excluding thereby possible long-range interactions of the two hydroxyl-groups. This binding energy itself is 0.67 eV higher than the one in the most favorable configuration IIA1, highlighting the substantial contribution of the hydroxyl-pairing to the high affinity of the SrO termination towards water. In fact, our calculations predict that it is actually this pairing mechanism, which enables the experimentally observed hydroxylation of the SrO terminated domains at lowest background humidity. Because of this enormous bond strength and the extraordinary high barrier $\Delta E_{\mathrm{IIA12}}$ for breaking it, our results challenge seriously the presence of freely diffusing hydroxyl-groups originating from adsorbed water molecules.

On the other hand, in the three atomic arrangements IIA2, IIA3 and IIA4, the occupation of the hydroxyls' oxygen atom O(1) of the bridging position between two adjacent strontium atoms in a height of about 1.7 Å above the surface corresponds always to the oxygen site in the continued perovskite lattice. This is line with the experimental observations that in presence of hydrogen and water the growth rate of $SrTiO_3$ is notably increased [52], because pure oxygen ad-atoms have been found previously, in the Chapter 4 to form covalently bonded dioxygen species. Thus, the formation of hydroxyl groups from oxygen and hydrogen ad-atom may be one possible process to remove the these covalent bonds and to ensure the emergence of the "correct" pervoskite lattice structure. Due to their similarity, such a mechanism would also apply for the crystallization of the other alkaline oxides $BaTiO_3$ and $CaTiO_3$, but probably also for more complex oxide system, emphasizing once again the general importance of hydrogen for superficially regarded very different applications.

5.4.2 TiO_2 termination

For the dynamics of the two hydroxyl-groups after the dissociation on the TiO_2 termination, two distinct diffusion processes come into consideration. At first, the motion of the single hydrogen H(2) in Figure 5.12 is investigated by illustrating an exemplary pathway separating the water fragments on the surface. Because during its motion the hydrogen atom forms subsequently hydroxyl-groups with the lattice oxygen atoms, the whole process may also be viewed as an effective diffusion of one hydroxyl-group, disregarding the fact that the position of the respective lattice oxygen atom does not change.

In connection with the dissociation of the water molecule, the hydrogen H(2) is transferred to the adjacent surface oxygen atom in configuration IIB3, followed by a lateral reorientation of the newly formed OH-bond towards the adjacent surface unit cell and arriving thereby at configuration IIB4. With an additional bond breaking hop the diffusing hydrogen atom H(2) has finally reached in configuration IIB5 the maximum distance to its original position in configuration IIB2, which is possible in a (3×3) unit cell. Similar to the case of the hydroxyl-group diffusing on the SrO termination, the configurations IIB3, IIB4 and IIB5 have practically the same binding energy, which is with less than 50 meV slightly favored over the one correspond-

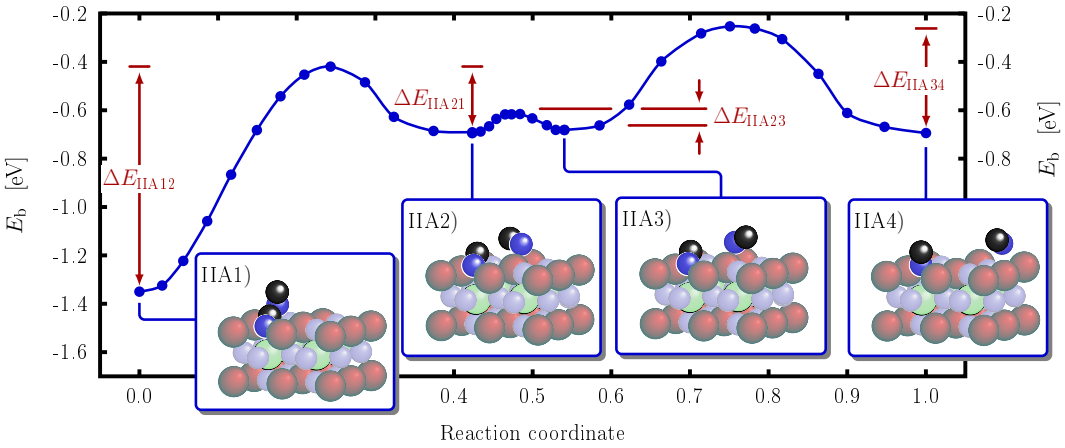

Figure 5.11: Energy profile for surface diffusion of the protruding O(1)H(1) hydroxyl group over the SrO terminated surface. The initial state IIA1 corresponds to the hydroxyl-pair after the immediate water dissociation process shown in Figure 5.1. The transition from state IIA1 to A2 breaks the hydroxyl-pair and is accompanied by a substantial energetic barrier. Configurations IIA2 and IIA3 differ essentially in the mutual orientation of the two hydroxyl-groups, whereas in state IIA4 the diffusing species has further increased the distance to its original position IIA1 by hopping to the adjacent binding site.

ing to IIB2. The reason for the slight decrease in energy is the lifting of the distortions of the bond O(2)–Ti(1) due to the removal of the surface hydroxyl group upon dislodging of the hydrogen atom H(2). In addition, the energy profile in Figure 5.12 displays equally moderate barriers $\Delta E_{\mathrm{IIB23}}$ and E_{IIB45} for the two explicitly calculated bond-breaking hops at different distances to the protruding hydroxyl-group. Thus, alike the SrO termination, on the TiO_2 termination, long range interactions between the hydroxyl-groups are very small. We note that the numerical value obtained for the barriers $\Delta E_{\mathrm{IIB23}}$ and $\Delta E_{\mathrm{IIB45}}$ of about 0.51 eV agrees very well with the barrier of 0.5 eV computed for the proton diffusion in bulk $SrTiO_3$ [266]. The activation energy for the necessary reorientation of the OH-bond is with $\Delta E_{\mathrm{B34}} = 0.38$ eV expectedly smaller, but not as small as for the corresponding motion on the SrO termination, which is also quite comprehensible because here the hydroxyl group is directly coordinated with two surface Ti-atoms and therefore much deeper embedded into surface lattice. The velocity of the hydrogen diffusion on the surface can be assessed by inserting the barrier $\Delta E_{\mathrm{IIB23}}$ into Eq. (4.2), resulting in a rate in the order of $10^4 \mathrm{s}^{-1}$ at room temperature. Thus, if water molecules are present on the TiO_2 termination, the herewith discussed hydrogen diffusion will play a probably a relevant role for the entire surface dynamics, which is most likely even more important for higher water coverages, when this surface presumably covered with a mixture of intact and dissociated water molecules.

Although we did not address this issue explicitly, we emphasize that this hydrogen diffusion is not strictly restricted to surface, but it could also point out one possible way to the hydrogen contamination of the $SrTiO_3$ sample [266, 267, 268, 269].

Starting from configuration IIB2, a second way to arrive at configuration IIB4 would be established with the transfer and subsequent rotation about the z-axis of the protruding, titanium coordinated hydroxyl-group O(1)H(1) to the next binding site, i. e. the next surface titanium atom.

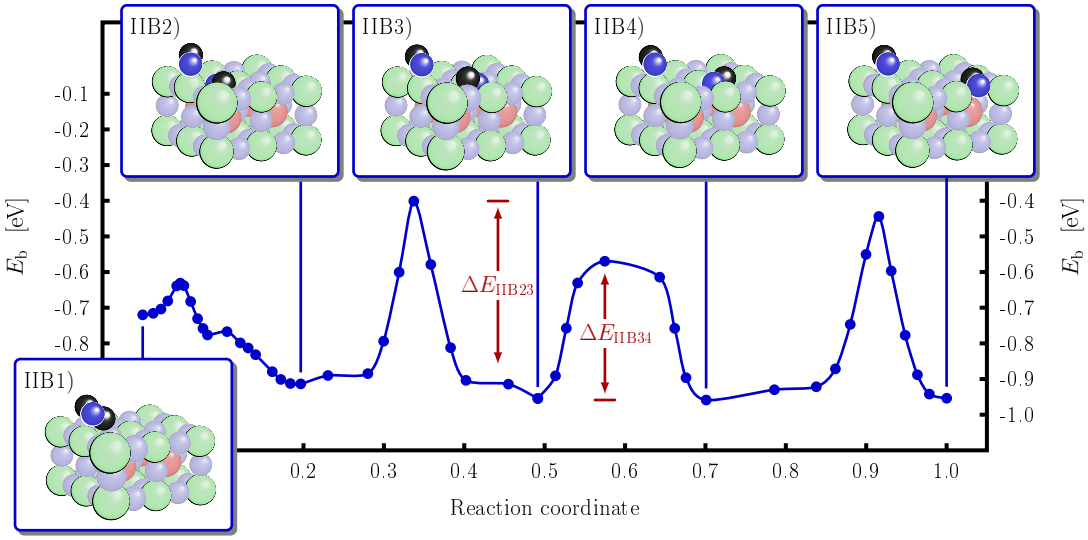

Figure 5.12: Energy profile for surface diffusion of the split-off H(2) atom over the TiO_2 terminated surface. The initial states IIB1 and IIB2 correspond to the molecular precursor and dissociated hydroxyl-pair shown in Figure 5.3 and Figure 5.5, respectively Further disintegration takes place via a hop of the surface H(2) atom to an adjacent lattice O anion (IIB3) with a barrier $\Delta E_{\mathrm{IIB23}} = 0.51$ eV, followed by a flip of the orientation of the newly formed hydroxyl group towards the neighboring surface unit-cell (IIB4) with a barrier $\Delta E_{\mathrm{IItB34}} = 0.38$ eV. The ensuing equivalent hop to an even more distant lattice O anion (IIB5) exhibits essentially the same energy profile, indicating overall only small longer-range lateral interactions between the hydroxyl groups.

This hopping process is studied in Figure 5.13, where we have also sketched the atomic positions at the transition state (TS) of this diffusion pathway. Interestingly, in this atomic arrangement the hydroxyl's oxygen atom and the lattice oxygen atom below assume a fourfold-bonded configuration with the two neighboring titanium atoms, rendering this arrangement very reminiscent of the adsorption geometry IB shown in Figure 4.1, where the oxygen ad-atom has adsorbed on the TiO_2 termination. However, in contrast to the latter case, where we have found the formation of a quasi-molecular peroxide anion at the surface, here the additional hydrogen atom seems to be responsible for the strong repulsion of the two oxygen atoms, which is indicated by their remarkably large distance of 2.3 Å.

As discussed above, the depicted energy profile exhibits a rather flat characteristics near the initial and final point of the process, which illustrates that rotations about the surface normal poses only very little energetic cost for the hydroxyl group O(1)H(1). Whereas in configuration IIB2 a clear tendency was observed for the two hydroxyl groups to arrange in parallel planes, in a greater distance, the alignment of the protruding hydroxyl group with each of the four underlying Ti-O bonds results in practically the same energy, suggesting thereby a fast dangling dynamics. However, the substantial, quasi-insurmountable barrier of 1.5 eV prohibits essentially the proposed hydroxyl-hopping and renders the hydroxyl-titanium bond rather stable. With binding energy of the H_2O species never falling below -1.5 eV on the TiO_2 termination, and with the moderate hopping barriers for the hydrogen diffusion, the protruding hydroxyl group is much more likely to recombine with a diffusing hydrogen atom to the water molecule in configuration IIB1 and subsequently desorb then from the surface instead of hopping to the next surface titanium atom.

As aforementioned in Chapter 3 the surface preparation and characterization of $SrTiO_3$ is formidable task for the experimentalists. With considering $SrTiO_3$ as a stack of SrO and TiO_2 plane and the notion that bulk TiO_2 is an acidic and bulk SrO as basic oxide, Kawasaki pioneered the preparation of smoothly TiO_2 terminated $SrTiO_3$ samples using a ph-controlled NH_4F-HF-solution [178]. This method was refined by later by Koster *et al.* [270, 271], who suggested that water would actually form a strontium hydroxide complex, which would then dissolve in the acid. Looking at the ground-state geometry IIA1 in Figure 5.1 and the energetics for the its decomposition, this picture is quite compatible with our results. With demonstrating that a large fraction of the bond strength is actually due to the formation of the hydroxyl-pair and with the huge energy barrier shown in Figure 5.11, this entity is rather stable. Contrariwise, the bond of the surface lattice oxygen at the adsorption site to the subsurface Ti-atom is stretched by almost one fifth indicating its substantial weakening. Therefore it seem quite possible that upon reaction with further species in the environment the $Sr(OH)_2$ unit at surface might be removed, such that only the subsurface TiO_2 layers remains. This applies especially to the extremely high water coverages being certainly achieved during this surface preparation procedure, because then also the step edges of the SrO terraces will most likely be decorated with the hydroxyl-pairs. The activation energy to separate these from the surface should be much lower than the energy threshold for the removal of a hydroxyl-pair in the center of a SrO terrace. Consequently, the entire SrO terrace would dissolve which is line the Koster *et al.*'s picture. On the other hand we have seen that upon water exposure on the TiO_2 termination hydrogen atoms are well available, such that possible isolated and very stable hydroxyl-groups can be expected to recombine to water molecules, which are less stable and can be removed from the surface more easily. Its

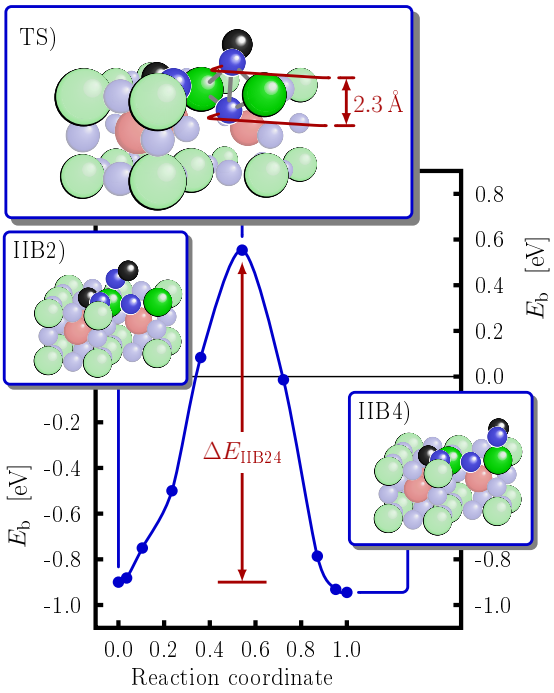

Figure 5.13: Energy profile for one surface diffusion hop of topmost hydroxyl group O(1)H(1) in configuration IIB2 as shown in Figure 5.5. The shown surface models have been cut open to visualize also the motion of the oxygen atom between the two titanium atoms.

noteworthy that the presence of the hydroxyl-pair is necessary for the facilitate the removal of the SrO surface layers, because as demonstrated in Figure 3.8, peeling off the pure SrO layer costs much more energy than the doing the same with the pristine TiO_2 surface layers. Moreover, as indicated in Figure 5.9 the suggested mechanism takes the $SrTiO_3$ sample farer away from the global thermodynamic equilibrium rather than leading into it.

6 Hydrogen and hydroxyls on $SrTiO_3$(001)

In Section 5.4 the separation of the dissociated water molecule in the dilute limit has been discussed for the both terminations. Intuitively one expects that upon a sufficiently large distance between the water species on the surface, their individual properties should also be confirmed in individual surface model systems. Consequently, we address in Section 6.1 the properties of the singly adsorbed hydrogen atom. This issue has also been worked on recently by Lin *et al.* [201] and we discuss critically the conclusion made by the authors. Then, in Section 6.2 we will briefly present our calculations addressing the singly adsorbed hydroxyl-groups on the surface. Finally, we complete this chapter with a discussion of the hydrogen co-adsorbed oxygen molecule in Section 6.3

6.1 Adsorption of atomic hydrogen

Very recently, atomic hydrogen on the $SrTiO_3$(001) surface has been studied theoretically by Lin *et al.* [201], concentrating thereby predominantly on the TiO_2 termination. Similar to the aforementioned preceding studies concerning the oxygen and water adsorption, the authors did not perform tests with respect to the size of the employed model system. As we have shown these two cases, too small model systems clearly miss essential parts of the physics, but they may be justified in some limiting cases, for instance, at high coverages. For the hydrogen ad-atom we will be able to show that the energetics obtained only with DFT in the semi-local approximation are misleadingly wrong when relying only on too small model systems.

6.1.1 Geometry

Figure 6.1 displays the adsorbed hydrogen ad-atom in its ground-state configuration on both terminations. As expected from the results obtained in the previous chapters, the hydrogen ad-atom binds to lattice oxygen atoms forming a surface hydroxyl-group. The bond lengths listed in Table 6.1 and Table 6.2 indicates that the hydrogen ad-atom inflicts differently severe distortions in the lattice.

On the SrO termination, the atomic hydrogen adsorption results in a dramatic lifting of the lattice oxygen atom O(1) out of the surface plane into the vacuum. The axis of the hydroxyl-group is sloped less than 20° with respect the surface normal vector, giving the impression that the hydroxyl-group assumes rather an upright than a tilted position. The bond of the oxygen atom O(1) to the subsurface titanium atom Ti(1) is stretched dramatically by almost 50% to 2.8 Å suggesting an even more pronounced weakening of this bond than in the cases of the atomic oxygen and the water adsorption on the SrO termination. The distance between Ti(1) and oxygen atom O(5) in the third layer shrinks by 13% upon hydrogen adsorption, confirming again the predominantly vertical propagation of the lattice distortions on the SrO termination.

Table 6.1: Characteristic bond lengths in the atomic configurations of the hydrogen ad-atom the SrO-termination, with Δd indicating the change in percent due to adsorption. The atomic labeling is defined in Figure 6.1.

IIIA	$d\,[\text{Å}]$	$\Delta d\,[\%]$		$d\,[\text{Å}]$	$\Delta d\,[\%]$
H(1) — O(1)	0.98	—	O(1) — Ti(1)	2.80	+47
O(1) — O(2)	4.24	+8	O(1) — Sr(1)	3.10	+11
O(3) — Ti(1)	1.94	-1	Ti(1) — O(4)	2.80	-1
Ti(1) — O(5)	1.78	-13	Ti(2) — O(3)	1.91	~ 0

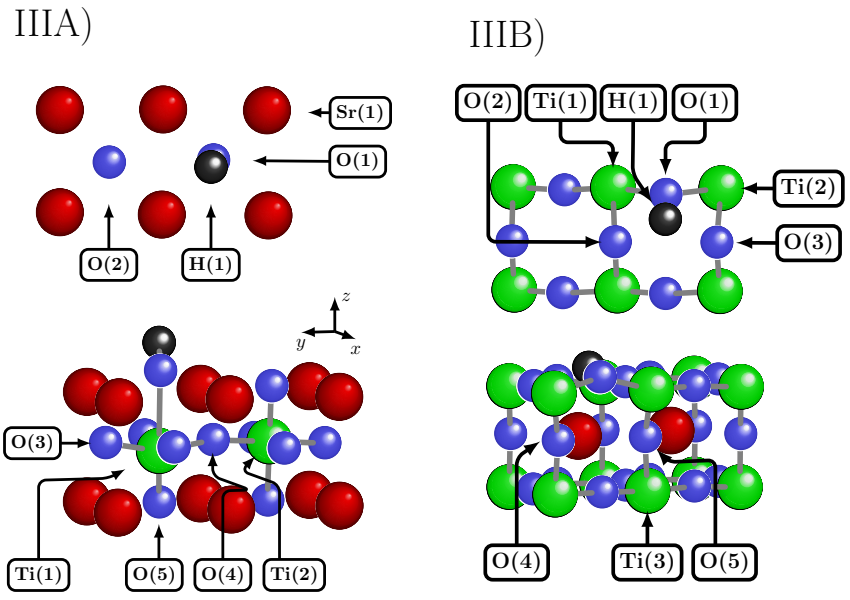

Figure 6.1: Ground state geometries assumed by the hydrogen ad-atom on the SrO-termination (left side) and the TiO_2-termination (right side). The upper panel shows a top-view and the bottom panel a perspective view on the respective configuration.

Table 6.2: Characteristic bond lengths in the atomic configurations of the hydrogen ad-atom the TiO_2-termination, with Δd indicating the change in percent due to adsorption. The atomic labeling is defined in Figure 6.1.

IIIB	$d\,[\text{Å}]$	$\Delta d\,[\%]$		$d\,[\text{Å}]$	$\Delta d\,[\%]$
H(1) — O(1)	0.98	—	H(1) — O(2)	2.27	—
H(1) — O(3)	2.23	—	O(1) — Ti(1)	2.14	+9
O(1) — Ti(2)	2.27	+14	Ti(1) — O(5)	1.84	~ 0
Ti(2) — O(4)	1.83	~ 0	O(5) — Ti(3)	2.07	+2

Contrariwise, the lattice distortions on the TiO_2 termination are comparably moderate and do not permeate deeper into the surface. Similar to geometry IIB2 of the dissociated water molecule, the formation of the hydroxyl-group pulls the lattice oxygen O(1) somewhat out of the surface plane, such that the distances to the adjacent Ti(1) and Ti(2) atoms are stretched in a similar fashion by 14% and 9%, respectively. The axis of the hydroxyl-group is tilted by 80° with respect to the surface normal and points to the hollow site above the subsurface strontium atom. However, the slightness of these lattice deformation does not guarantee an easy calculation of the optimal geometry. In contrast, our experience suggests that exactly these subtle deformations are responsible for the emergence of many local minima in the energy landscape, hampering seriously geometry optimizations for extremely large TiO_2 terminated surface models.

6.1.2 Binding energy

In spite of this different change of the geometric parameters, the energetics could not be converged for none of the two terminations in the same rigorous way as in the previous chapters. The binding energy is referenced here to the half of the total energy of the gas phase hydrogen molecule $E_{H_2}^{Gas}$:

$$E_b = \frac{1}{2}\left[E_{H@Surf} - E_{Surf} - E_{H_2}^{Gas}\right] \quad , \tag{6.1}$$

and exhibits a dramatic decrease with increasing size of the surface models. In Figure 6.2 the binding energies obtained in various model geometries are shown as a function of the reciprocal cubic root of the volume V of the $SrTiO_3$ slab in the surface model. Plotting in this way, the displayed graphs referring to a constant number of atomic layers with dropping coverage exhibit an approximately *linear* decrease of the binding energy for larger V. Such a behavior is clearly expected for calculations of charged systems in periodic super-cells but not for charge neutral ones [272, 273]. In Figure 3.6 we have demonstrated already that increasing the vacuum space separating the two surfaces of the slab model left the respective total energy virtually unchanged, which rules out ultimately the unlikely possibility, that the employed CASTEP code placed erroneously a net charge into the super-cell.

In any case, the graphs in Figure 6.2 allow to filter out the effect of the lattice distortions on the energetics. For the SrO termination we find that the data obtained in surface models with

seven and nine atomic are distinctly different from those corresponding to the eleven and 13 atomic layers. The latter two lie virtually on top of each other, indicating that these energies have been converged with respect to the lattice relaxations, nevertheless they exhibit a likewise decreasing behavior with increasing volume of the supporting $SrTiO_3$ slab.

On the TiO_2 termination, the calculated binding energies exhibit essentially the same trend. Here, the greater spreading of the data reflects the aforementioned difficulties to find the correct ground-state structure. In addition, the graphs for different number of atomic layers are hard to distinguish, furnishing the appropriate description of the lattice distortions on the TiO_2 termination provided by seven layer surface models.

For completeness, we have added the corresponding binding energies calculated by Lin *et al.* to Figure 6.2, who focused exclusively on seven layer surface models. Although the authors employed a very similar methodology, i. e. density functional theory with the PW91 gradient-corrected exchange correlation functional of Perdew and Wang [82] and a plane wave basis set corresponding to $E_{\mathrm{Cut}} = 400$ eV, we can reproduce only their binding energies for the TiO_2 termination corresponding to 1.0 ML and 0.5 ML coverage within 100 meV. This deviation may be explained with their insufficient relaxed geometries, whereas the drastic discrepancy between their and our binding energy at 0.25 ML coverage on TiO_2 termination as well as their binding energy for the SrO termination could not be reproduced even after numerous attempts. Irritatingly, Lin *et al.*'s binding energy given for the TiO_2 terminated (1×1) seven layer surface model agrees within 20 meV to ours for the five layer slab. Such a small deviation would be expected for calculations with identical settings differing only in the different flavors of GGAs for the electronic exchange correlation. On any account, our data presented in Figure 6.2 challenges seriously the conclusions made by Lin *et al.* on the basis of their insufficiently explored energetics.

Intuitively, the persistently decreasing binding energy in a charge-neutral super-cell is non-physical and most likely only a symptom of the applied semi-local exchange correlation. Therefore, only the binding energy in the limit of the infinite volume of the super-cell is certainly the only quantity to characterize the binding of the hydrogen ad-atom in a reasonable way. Our Ansatz for the fitting function to extrapolate our data is motivated by the formula of Makov and Payne [273, 274] for the electrostatic contribution to the total energy in charged periodic super-cells

$$E(L) = E_\infty + \frac{q^2\alpha}{2\varepsilon L} + \frac{2\pi Qq}{3\varepsilon L^3} + \mathcal{O}(L^{-5}) \quad , \tag{6.2}$$

with L being the cubic root of the super-cell's volume and q,ε, α and Q are the total charge in the super-cell, the dielectric constant, the Madelung constant and the second radial moment of the electron density. Clearly, the total charge in the system under investigation is zero, letting us consider the coefficients in the latter equation simply as fit parameters A and B in the function

$$E_{\mathrm{b}}(v) = E_{\mathrm{b}}^{\infty} + Av + Bv^3 \qquad \text{with} \qquad v = V^{-\frac{1}{3}} \quad . \tag{6.3}$$

As illustrated in Figure 6.2, the data for the SrO termination is described extremely well by the latter relation. For the models with 13 atomic layers, the aimed binding energy E_{b}^{∞} for infinitely

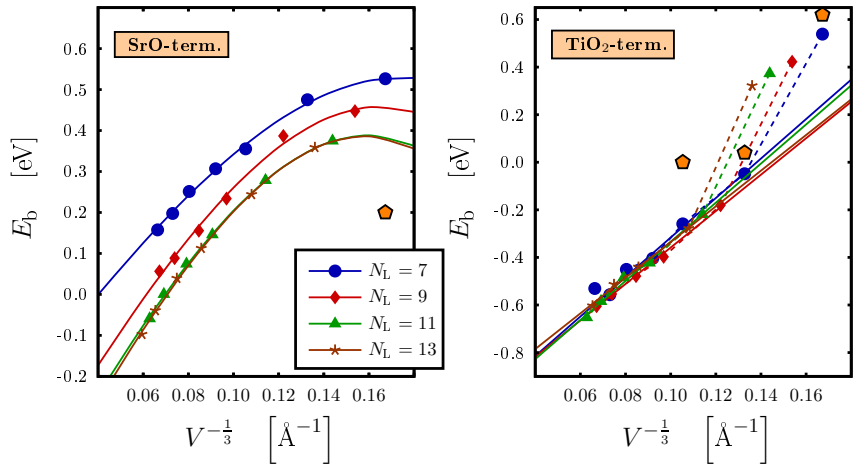

Figure 6.2: Binding energy of the adsorbed hydrogen atom on both terminations as a function of the reciprocal cubic root of the substrates' volume V in the surface model. The different colors and symbols discriminate the data for constant number of atomic layers N_L with decreasing coverage. The symbols and the dashed lines denote the calculated data, whereas the solid lines represent the respective fit used for the extrapolation to infinite volume. The pentagons stand for the binding energies obtained by Lin *et al.* [201] with their seven-layer-surface models. In order to allow a fair comparison, their numbers have been shifted with our theoretical value of the dissociation energy of the hydrogen molecule.

large super-cell is extrapolated to -0.64 eV. For their remote position on the abscissa, the greatest error of the fitted parameters is induced by the binding energies calculated for high coverages in (1×1) super-cells. Omitting these data in the fitting procedure did not lead to changes larger than 100 meV for E_b^∞ for the case of the SrO termination, which should be viewed as a small variation under the prevailing circumstances. In contrast, on the TiO_2 termination the greater scattering of the unfortunately too scarce data results in unreasonably large deviations of the fitted parameters. On the other hand, visual inspection yields a practically linear falling of the binding energy, if the data obtained in (1×1) surface models is neglected. With the parameter B in Eq. (6.3) set to zero in advance, we fit therefore only the calculated binding energies for lower hydrogen coverages with straight lines. The resulting extrapolated binding energies are all in the relatively small range from -1.09 eV to -1.16 eV for the different numbers of atomic layers, inspiring confidence in the validity of the applied procedure.

At this points, we do not take futile steps in order to assign a deeper physical importance to the factors A and B in Eq. (6.3), because their numerical values are functions of the volume V, too. We calculated the volume V as the product of the surface cells, the number of layers and the lattice constant multiplied with a factor of $\frac{1}{2}$ accounting for the strict mirror symmetry of the employed surface models. On the other hand, omitting the latter or applying another arbitrary factor changes A and B, but does not affect the extrapolated binding energy.

Before rationalizing the binding energy's peculiar behavior a bit further, we briefly comment on the calculation of the data in Figure 6.2. The different ad-atom densities have been modeled by placing the hydrogen ad-atom on (1×1), $(\sqrt{2} \times \sqrt{2})$, (2×2), (2×3), (3×3), (3×4)

and (4×4) surface models, corresponding to hydrogen coverages of 1.0 ML, 0.5 ML, 0.25 ML, 0.25 ML, 0.17 ML, 0.11 ML, 0.08 ML and 0.06 ML. For their pricy computational cost, we were not able to get fully converged results for (4×4) surface cells with more than seven atomic layers. The hydrogen induced metalization of the $SrTiO_3$ surface renders finer meshes of **k**-points in the Brillouins-zone necessary. Corresponding to the aforementioned super-cells, we had to use grids of $(12 \times 12 \times 1)$, $(8 \times 8 \times 1)$, $(6 \times 6 \times 1)$, $(6 \times 4 \times 1)$, $(4 \times 4 \times 1)$, $(4 \times 3 \times 1)$ and $(3 \times 3 \times 1)$ **k**-points, each ensuring a convergence of the total energy $E_{\mathrm{H@Surf}}$ of at least 10 meV. We also confirmed in tests using (1×1) and (2×2) surface models, that spin-polarization did never exceed the magnitude of numerical noise and had no relevant effect on the resulting total energies. In addition, we emphasize at this point that these calculations consumed substantial resources. For instance, the calculation of the TiO_2 terminated (3×4) super-cell with 13 atomic layers requires per **k**-point and CPU approximately 5 GB memory, if one **k**-point is distributed over 128 processors. This system has six **k**-points in the irreducible wedge of the Brillouins-zone and therefore we parallelized this particular calculation over 768 CPUs allocating thereby in total 3.8 TB memory. With this set-up and the processors clocked at 3.0 GHz, one step in the geometry optimization takes still about six hours As a matter of course, these enormous costs made a careful recycling of structure information obtained in smaller super-cells as described in Section 3.2.2 and preparative geometry optimizations with only one **k**-point indispensable in order to reduce the number of steps in the geometry optimization procedure.

6.1.3 Electronic properties

The key point of Lin *et al.*'s paper is the aforementioned metalization of the $SrTiO_3$ surface due to hydrogen adsorption [201]. In agreement, we also find in our calculated eigenvalue spectra a non zero density of states at the Fermi level, which is the recognition feature of metals. However, monitoring the contribution of the individual atoms casts doubt on the interpretation of Lin *et al.* that the *surface* becomes metallic upon atom hydrogen adsorption. Figure 6.3 presents the total density of states of the adsorption geometries IIIA and IIIB, the detailed contributions of the formed hydroxyl-group as well as the projection on the individual titanium atoms integrated over the respective atomic layers. The newly occupied states are located at the lower edge of conduction band, which is formed exclusively by the 3*d* orbitals of the titanium atoms allowing to spare the oxygen and strontium contributions in Figure 6.3. Apparently, the metallic states are not located in the topmost surface layer. As it is quite intuitive for the SrO termination, for the TiO_2 termination this is somewhat surprising, because the surface titanium atoms have a charge state different from that of their colleagues in the bulk and are therefore certainly the best candidates for playing an essential role in modification of the electronic structure in the surface region. In addition, the projections on the deeper TiO_2 layers, show that the metalization seems to be a *bulk* phenomenon, because the bulk-like layers in the surface model contribute significantly to the density of states at the Fermi-level for both terminations. Moreover, in case of the TiO_2 termination, this contribution seems to increase with distance to the surface.

On the other hand, Figure 6.3 helps to understand the strange behavior of the binding energy in Figure 6.2 a little better. As the graphs in Figure 6.2 imply that the binding energy is crucially

controlled by the electrostatic or Hartree energy E_{Hartree} in the periodically repeated super-cell:

$$E_{\text{Hartree}} = \frac{1}{2}\sum_{\{\mathbf{l}\}}\int_{V_C}\int_{V_C} \mathrm{d}^3r\,\mathrm{d}^3r'\,\frac{\rho(\mathbf{r})\rho(\mathbf{r}')}{|\mathbf{r}-\mathbf{r}'+\mathbf{l}|} \quad , \tag{6.4}$$

with $\rho(\mathbf{r})$ and V_C being the charge density, and the super-cell's volume, respectively. The sum runs over the complete, infinite lattice, i. e. $\{\mathbf{l}\}$ is the set of lattice vectors defined by $n_1\mathbf{a}_1 + n_2\mathbf{a}_2 + n_3\mathbf{a}_3$ for any combination for the triple of arbitrary integers n_i and the vectors $\mathbf{a}_i$ spanning the super-cell. The derivation of a more feasible expression without the unwieldy lattice sum requires summation techniques being developed for instance in Refs. [275, 276, 277, 278] and was executed by Makov and Payne [273]. For details, we refer the reader to their paper and we proceed immediately with the argumentation leading to Eq. (6.2). Starting the evaluation of the last expression requires at first an estimation of the charge density $\rho_{\text{H@surf}}$ of the combined system of the $SrTiO_3$ surface and the hydrogen ad-atom. In an approximate fashion, we regard this simply as the total charge density ρ_{surf} of the pure $SrTiO_3$ slab-model comprising the electronic and ionic contributions, a point charge q denoting the effective charge of the hydrogen's proton at the position $\mathbf{r}_0$ and a part, which models the delocalized charge injected in the conduction band as illustrated in Figure 6.3. The latter is obviously concentrated in the vicinity of the titanium atoms. However, these species are uniformly distributed in $SrTiO_3$, allowing to approximate this contribution as a jellium-like charge background formed by the hydrogen electron. Hence, the requested density is written as:

$$\begin{aligned}\rho_{\text{H@surf}} &= \rho_{\text{surf}} + q\delta(\mathbf{r}-\mathbf{r}_0) - \frac{q}{V} \\ &= \rho_{\text{surf}} + \rho_{\text{H}} \quad .\end{aligned} \tag{6.5}$$

From this charge distribution, essentially three terms for the electrostatic energy arise. The most unproblematic one is obtained by inserting ρ_{surf} into Eq. (6.4), which is of the order of $\mathcal{O}(V^{-\frac{5}{3}})$ [273] and cancels to large extent when calculating the binding energy, because E_{Surf} in Eq. (6.1) comprises a very similar contribution.

The second part E_2 is due the interaction of ρ_{surf} and ρ_{H}, to which the arguments of Makov and Payne apply directly allowing us to adopt their result without hesitation:

$$E_2 = \frac{2\pi q}{3\varepsilon V}\int_V \mathrm{d}^3r\, r^2\rho_{\text{Surf}}(\mathbf{r}) + \mathcal{O}(V^{-\frac{5}{3}}) \quad . \tag{6.6}$$

The leading term E_1 is obtained by evaluation the double integral in Eq. (6.4) for ρ_{H} as defined in Eq. (6.5). Obviously, this is nothing but the Madelung energy of an infinite array of positive point charges q immersed in a neutralizing jellium background:

$$E_1 = \frac{q^2\alpha}{2\varepsilon V^{\frac{1}{3}}} \quad . \tag{6.7}$$

Adding the last two expressions recovers Eq. (6.2). This supports clearly the use of Eq. (6.3) in order to extrapolate empirically the binding energy, we have also identified, origin of the binding energy's pathologic behavior. It is ultimately the charge delocalization that leads in a periodic

arrangement to an effective charging of the system, although the net charge in the super-cell is zero. This corresponds exactly to the usual textbook case where an infinite array of point charge is discussed, and which requires a constant background jellium in order to lift the occurring singularity in Eq. (6.4) [279] and to well-define the electrostatic energy. The positive slope of the graphs in Figure 6.2 denotes a strongly repulsive interaction between the hydrogen ad-atom with its periodic image, corroborating strongly this interpretation. In addition, the appearance of the second radial moment Q of the charge density ρ_{Surf} of the clean surface is also very consistent with the different behavior of the binding energy with respect to the term proportional to the inverse volume in Eq. (6.3). For numerical reasons we have omitted when fitting the data for the TiO_2 termination, but the curvatures of the graphs including the data for the high coverages in Figure 6.2 drops a hint at an opposite, termination specific sign of this term, reflecting in turn the converse charge state of the two regular terminated surfaces.

Having now established the direct impact of the electronic delocalization on the energetics, we suggest that Lin *et al.*'s metalization of the $SrTiO_3$ surface is an artifact due to the severest failure of the semi-locally approximated exchange-correlation, namely the grotesque underestimation of the electronic band-gap. The panels (b) in Figure 6.3 itemize the contributions of the individual molecular orbitals of the formed hydroxyl-groups. We have got acquainted already to the occupied σ and π states in Section 5.3 letting us concentrate directly on the lowest unoccupied states. These are located for the SrO and TiO_2 termination slightly above 2 eV and approximately at 3 eV, respectively, which is clearly higher than the lowest Ti $3d$ states in the conduction band. This implies in turn that the present treatment of the electronic structure is incapable to describe an occupied localized hydrogen impurity level in the band gap, which would be the experimentally relevant situation.

Finazzi *et al.* [280] studied recently the delocalization of the electronic ground state wave function for hydrogen impurities in TiO_2 in dependence of different exchange-correlation functionals. Their smashing conclusion is, that pure semi-local functionals are definitely not appropriate to attack this problem in a realistic way and, even more devastating, employing hybrid functionals does not necessarily improve the situation. For the latter, the localization properties of the computed ground-state wave-function depend crucially on details in the Hartree-Fock exchange mixing procedure, which is of course unsatisfactory. It is known that $SrTiO_3$ may become semi-conducting upon doping [30, 152, 281] and it has been shown to be a good proton conductor [154], too. However, the density of states at the Fermi level should be zero at 0 K for a semi-conductor, which is definitely not the case in Figure 6.3. On the other hand, the intriguing phenomenon of "local-metalization" in $SrTiO_3$ samples being reported by Szot *et al.* [282] seem to for more complex than to be explained just with hydrogen contamination.

Similar unexpected behaviors of formation energies with respect to the super-cell have been reported recently for charged defects [274, 283] as well as neutral defects and hydrogen impurities in ZnO [284]. In the latter study the correction due to Eq. (6.2) has also been applied achieving thereby good consistency with experimental observations. This raises our hopes that the extrapolated binding energies of the hydrogen ad-atom are probably not completely meaningless, although the present treatment of the underlying electronic structure can not grasp the correct physics. However, this needs to be checked in future using approaches being able to correct the malicious band-gap, for instance the "GGA+U" method [118, 119], especially fitted hybrid functionals or the more rigorous but also much more demanding GW-approximation [62].

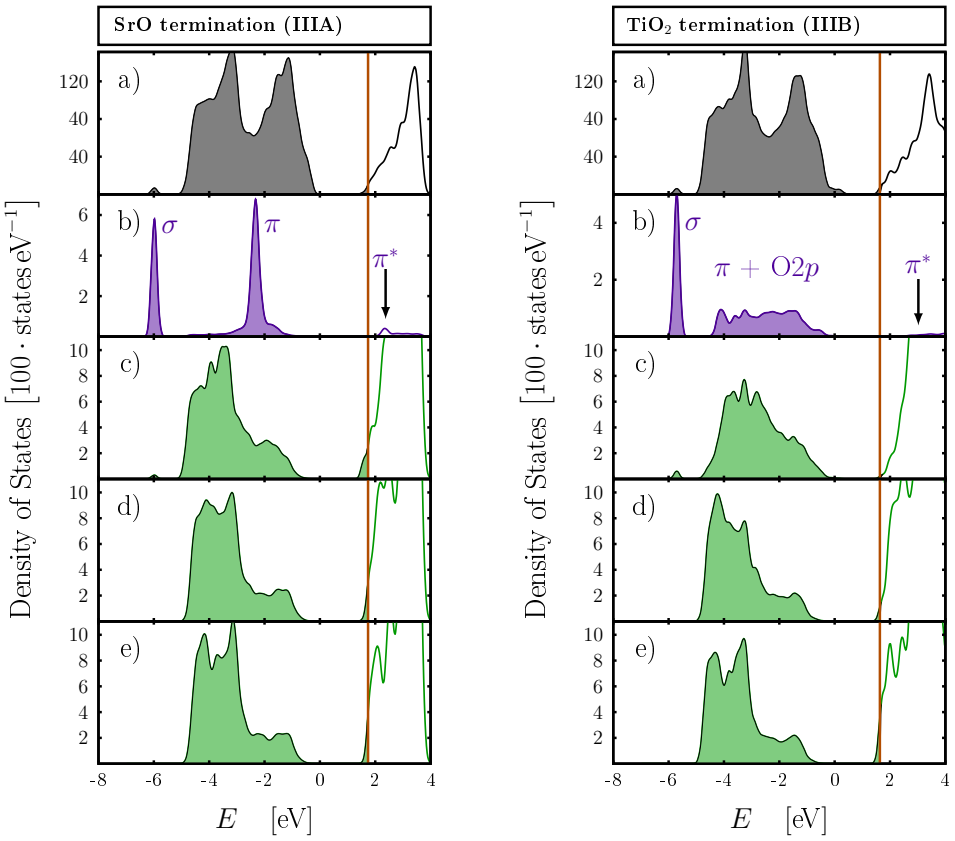

Figure 6.3: Density of states of the hydrogen adsorption on both terminations of the $SrTiO_3(001)$ surface. For both sides, panel (a) shows the total density of states and panel (b) displays respective the projection on the hydroxyl-group of the adsorption geometries IIIA and IIIB, respectively. On the left side, the lower three panels (c), (d) and (e) indicate the contribution of the all titanium atoms in the second, fourth and sixth atomic layer, while on the left side the same panels show the corresponding projection of the titanium atoms in topmost, the third and the fifth atomic layer, respectively. The occupied states are highlighted by filled, the unoccupied by empty curves. The original eigenvalue spectra have been aligned with the respective maximum of the valence band in the central layers of the surface model. Subsequently, they have been convoluted with a Gaussian of a width of 0.1 eV. The vertical orange line denotes the Fermi energy.

Table 6.3: Characteristic bond lengths in the atomic configurations IVA and IVB of the isolated hydroxyl-group adsorbed, with Δd indicating the change in percent due to adsorption. The atomic labeling is defined in Figure 6.4.

IVA	$d\,[\text{Å}]$	$\Delta d\,[\%]$	**IVB**	$d\,[\text{Å}]$	$\Delta d\,[\%]$
H(1) — O(1)	0.98	—	H(1) — O(1)	0.98	—
H(1) — O(2)	2.27	—	H(1) — O(2)	2.80	—
O(1) — Sr(2)	2.55	—	O(1) — O(2)	2.90	—
O(1) — Sr(1)	2.52	—	O(1) — Ti(1)	1.82	—
O(1) — O(2)	2.43	—	Ti(1) — O(3)	2.27	+23
O(2) — Ti(1)	2.13	+10	O(3) — Ti(2)	1.85	-10
O(3) — Ti(2)	1.86	-2	Ti(1) — O(2)	2.17	+5
O(2) — O(3)	4.59	+16			

6.2 Adsorption of single hydroxyls

A possibly complete picture of the adsorption of aqueous species on $SrTiO_3(001)$ requires necessarily also the consideration of the single adsorbed hydroxyl-groups. However, as before we have restrict ourselves to present, unfortunately merely preliminary, non-conclusive results.

6.2.1 Geometry and Energetics

The positions taken by the singly adsorbed hydroxyl-group are illustrated in Figure 6.4 with the configurations IVA and IVB for the SrO and TiO_2 termination, respectively. These geometries are further characterized in Table 6.3 with some selected bond lengths and display properties reminiscent to the protruding hydroxyl-groups found for the decomposed water molecule in Section 5.4. On the SrO termination the hydroxyls' oxygen atom O(1) assumes again bridging, perovkite-type position between the two surface strontium atoms Sr(1) and Sr(2) in a vertical distance of approximately 1.6 Å. The most notable difference to the geometries IIA3 and IIA4 is the tilting of the OH-bond about 50° with respect to the surface normal, letting the hydrogen atom point into the vacuum, whereas in the previous discussed geometries, the OH-bond were directed to the respective adjacent lattice oxygen O(2). The adsorbed hydroxyl-group seems also to result in a repulsion both of the neighboring lattice oxygen atom O(2) and O(3), which is detected by their about 16% increased distance due to adsorption. In addition, we note that the oxygen atom O(2) is lifted somewhat into the vacuum, whereas the other atom O(3) is pressed slightly into the bulk. On the other hand, compared to the adsorption geometries for the SrO terminations we discussed before, the lattice distortions have to be classified as moderate in this case. On the TiO_2 termination, the position of the adsorbed hydroxyl-group corresponds almost exactly to the one of the protruding species of configuration IIB2 shown in Figure 5.5, i. e. the hydroxyls' axis is again tilted by 60° with respect to the surface normal and the titanium atom Ti(1) at the adsorption site is lifted somewhat into the vacuum, resulting in a distance Ti(1)-O(1) of 1.85 Å.

We define the binding energy for convenience with respect to the total energy of the gas phase

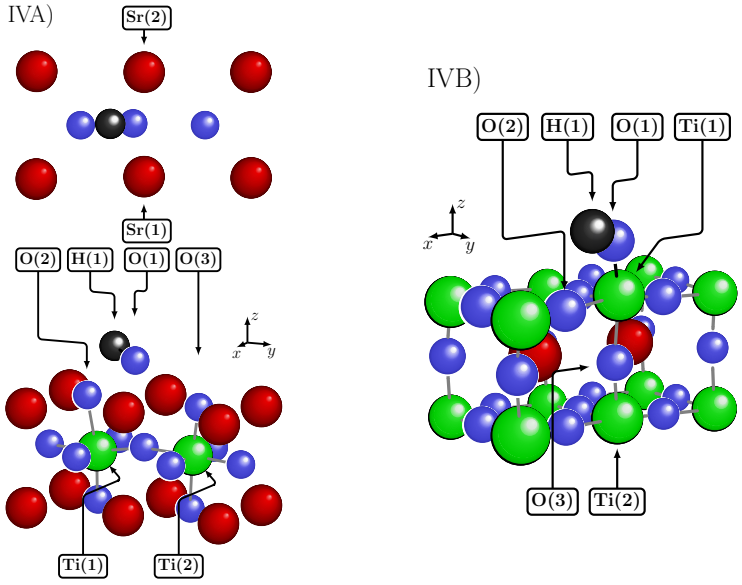

Figure 6.4: Ground-state geometry of the adsorbed hydroxyl-group on the on the SrO termination (left) and the TiO_2 termination (right). For the sake of clarity, for SrO termination a top view on the first atomic layer and perspective side view in bottom panel are shown. Contrariwise, a top view for the TiO_2 termination would not be assistant, because the topmost hydroxyl-group partly covers atoms of the surface layer.

hydrogen and oxygen molecule:

$$E_{\mathrm{b}} = \frac{1}{2}\left[E_{\mathrm{OH@Surf}} - E_{\mathrm{Surf}} - E^{\mathrm{Gas}}_{\mathrm{H_2}} - E^{\mathrm{Gas}}_{\mathrm{O_2}}\right] \quad . \tag{6.8}$$

Despite their frequent occurrence, single, $(\mathrm{OH})^-$ radicals are not stable and consequently they do not represent an appropriate thermodynamic reference. In spite of the relatively mild lattice distortions induced by the adsorption, the binding energies listed in Table 6.4 clearly miss a convincing convergence with the surface model size. However, the energetic difference between the adsorption geometries IVA and IVB is approximately constant ranging from 200 eV to 300 eV for equivalent geometric model geometries. In fact, comparing the data for high and low coverage yields for both terminations the same decrease of approximately 0.5 eV in binding energy and therefore we may conclude that the adsorption of the hydroxyl on the TiO_2 termination is indeed preferred over the other. Despite the scarceness of the data in Table 6.4 we perceive a trend being distinctly different from the behavior in the case of the water molecule discussed in Chapter 5, where employing increased model systems resulted in a qualitative difference between the two terminations due to differently pronounced lattice distortions. As aforementioned, for the adsorbed hydroxyl-group lattice distortions do not seem to play a major role for the energetics, which must be consequently controlled primarily by the electronic structure.

Table 6.4: Binding energies of a single hydroxyl-group on the SrO (IVA) and the TiO_2 termination (IVB) for some specific geometry set-ups. The configurations IVA and IVB are shown in Figure 6.4.

Surface	**k**-points	N_L	E_b^{IVA} [eV]	E_b^{IVB} [eV]
(1×1)	$(12\times12\times1)$	7	-0.79	-1.06
		9	-0.79	-1.08
		11	-0.78	-1.08
(2×2)	$(6\times6\times1)$	7	-0.93	-1.26
		9	-0.96	-1.29
		11	-0.99	-1.32
(3×3)	$(4\times4\times1)$	7	-1.25	-1.43
		9	-1.29	-1.51
		11	-1.33	-1.56

6.2.2 Electronic properties

It is known that OH-groups are powerful electron scavengers, in fact, hydroxyls occur in practice only as charged $(OH)^-$ radicals A similar thing is happening in configurations IVA and IVB, where the adsorbed hydroxyl-groups trap charge from the supporting $SrTiO_3$ substrate, being quantified with the Hirshfeld-(Mullliken-) charges of the entire hydroxyl-group computed to the of -0.23e (-0.45e) and -0.14e (-0.37e) for the SrO and TiO_2 termination, respectively. This charge trapping is equivalent to the injection of a hole into the valence band, which we confirm explicitly in Figure 6.5 for the TiO_2termination with the position of the Fermi energy below the top of the valence band. The observed metalization of the model system requires again the use of increased **k**-point-grids as listed in Table 6.4). Therefore we surmise on the basis of the binding energies in Table 6.4 and the discussion for the hydrogen ad-atom in the previous section that corrections to finite super-cell size are crucially important for the energetics in this case, too. Of course, the effective charge q will bear certainly the opposite sign and will be of different magnitude with respect to the corresponding quantity in Eq. (6.5). However, the present scarceness of the data does not allow for a robust argumentation into this direction. Interestingly, the charge state of the hydroxyl's oxygen atom O(1) is very similar to the one of the lattice oxygen atoms in the first layer bearing a Hirshfeld- and Mulliken charge of -0.32e and -0.72e. Therefore, as discussed for the water adsorption in Chapter 5, the hydroxyl-group completes the octahedral coordination shell of the surface Ti(1) atom. In fact, this allows the interpretation that the water molecule is stabilized on the TiO_2 termination in the dissociated states IIB2-IIB5 in Figure 5.12, because the second hydrogen atom H(2) provides the charge necessary to prevent de-population of the valence band, which in turn gives in a huge energy gain.

For the SrO termination in configuration IVA, the Fermi energy is computed directly on top of the valence band, and thus strictly speaking we do not observe delocalization of the electronic wave-functions. However, we see that the hydroxyl adsorption leads to a shallow acceptor level at about 0.2 eV above the Fermi-level, a feature, which is clearly absent for the TiO_2 termination.

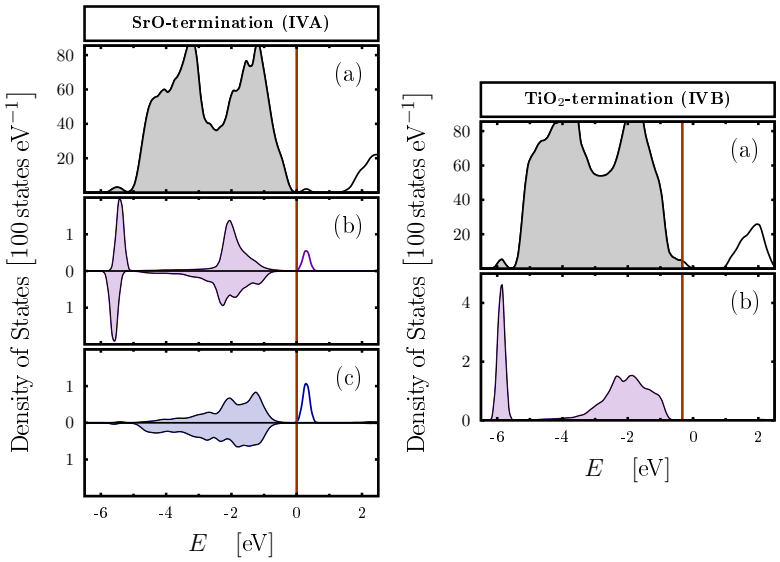

Figure 6.5: Electronic density of states after the adsorption of a single hydroxyl-group for both terminations on the $SrTiO_3$ surface. The panels (a) and (b) show the total density of states, as well as the projection on the hydroxyl-group. In addition, panel (c) on the right side shows the contribution of the lattice oxygen atom O(2) next to the hydroxyl-group. Panels (b) and (c) are subdivided in order to highlight the individual contributions of the spin up and spin down channels. The vertical red line marks the Fermi-energy and (un-) occupied states are drawn using (empty) filled curves. The original eigenvalue spectra have been convoluted with a Gaussian smearing of 0.1 eV. The energy scale has been shifted to the valence band maximum of the three inner layers in the slab, serving as an approximation for the top of the valence band in the bulk.

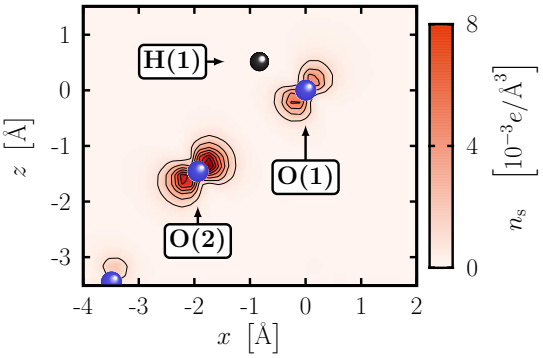

Figure 6.6: Spin density in the *xz*-plane near the adsorbed hydroxyl group on the SrO termination. The atomic labeling is defined in Figure 6.4.

With this acceptor level, the SrO terminated surface will act indeed as a *p*-doped semiconductor, which is qualitatively different from the metalization of the TiO_2 surface. As unravelled in Figure 6.5, this acceptor level is predominantly formed by unoccupied spin-up states of the hydroxyl-group and the neighboring lattice oxygen atom O(2), leading to the initially unsuspected preference of an electronic ground-state bearing a net spin polarization. We illustrate this in Figure 6.6 by presenting the spin density defined as the difference between the density of the spin-up and spin-down electrons:

$$n_S(\mathbf{r}) = n_\uparrow(\mathbf{r}) - n_\downarrow(\mathbf{r}) \quad . \tag{6.9}$$

In the vicinity of the hydroxyl-group, an alignment of the spin-polarized orbitals of the hydroxyls' oxygen O(1) and the neighboring lattice oxygen O(2) atom is clearly visible. This polarization spans also to a minor extent the oxygen atom in the second atomic layer, which is located roughly on the extended connection line O(1)-O(2) and is indeed quite remarkable, because both, naturally occurring $(OH)^-$ radicals and $SrTiO_3$ are diamagnetic, but in combination our calculations say that they are not. The Hirshfeld and Mulliken charges of the O(2) anion amounts -0.27*e* and -0.87*e*, respectively, whereas the same quantities for the clean SrO termination measure -0.40*e* and -0.83*e*, which is consistent with the picture that the O(2) surface anion shares a fractional electron with O(1). However, this charge transfer is not sufficient to compensate the *neutral* OH-species' spin moment, resulting in turn in the adsorption induced spin moment on the surface. Similar to case of the TiO_2 termination, in configuration IVB, such a compensation requires additional charge by for instance one more hydrogen atom on the surface as discussed in Chapter 5. This concept is very consistent with the energy profiles shown in Figure 5.11 and Figure 5.12, where practically no longer ranged interaction between the diffusion species was found and the hydrogen H(2) atom seems to play only the role of an electron donor.

6.3 Molecular adsorption of oxygen

As mentioned already in Chapter 4 and in Ref. [208] molecular oxygen adsorption is unlikely to happen on the perfect $SrTiO_3(001)$ surface.. On the other hand, in presence of defects and impurities charge carriers become more available and thus binding of the impinging gas molecules via charge transfer is much more likely. However, explicit the treatment of defects in bulk-$SrTiO_3$ and particular on the surface is especially difficult [210]. In the last two sections we have demonstrated that hydrogen ad-atoms make charge effectively available allowing us to thereby simulate the presence of unspecified defects and impurities with a formally charge neutral surface model. This is a primary motivation to perform also calculations addressing the molecular oxygen adsorption due to surface hydrogen ad-atoms. Apart from the possibility to examine in a relatively unproblematic way the presence of charge carriers , this situation has certainly also experimental relevance, because hydrogen and hydroxyls will are likely to interact with gas phase oxygen in a sufficiently humid environment. However, as in the preceding sections the results presented here represent only a first steps in order to assess such an interaction.

6.3.1 Binding energy and geometry

As in the preceding sections we define the binding energy with respect to the neutral, thermodynamic relevant gas phase oxygen and hydrogen:

$$E_{\mathrm{b}} = \frac{1}{2}\left[E_{(\mathrm{O_2+H})@\mathrm{Surf}} - E_{\mathrm{Surf}} - E_{\mathrm{H_2}} - 2E_{\mathrm{O_2}}\right] \quad . \tag{6.10}$$

Due to the scarceness of data similar to the preceding section, the energetics can be considered as sufficiently converged with the respect to the super-cell size only for the TiO_2 termination. In spite of this drawback the computed binding energies in Table 6.5 allow to identify clearly the preferred adsorption on the SrO termination over the other at lower coverages. Differently, but similar to the water molecule in Chapter 5 at higher coverages the adsorption process seems to be favored equally for both terminations.

The ground-state adsorption geometries VIA and VIB for the hydrogen co-adsorbed oxygen molecule are presented for each termination in Figure 6.7 and Figure 6.8. Not unexpectedly, the hydrogen atom forms a surface hydroxyl-group with a lattice oxygen atom, reminiscent to the configuration IIIA and IIIB in Figure 6.1. On both terminations the oxygen molecule does not dissociate, but as perceptible from the data in Table 6.6 and Table 6.7, the oxygen-oxygen bond is increased by 9% and 7% for the SrO and the TiO_2 termination, respectively. This increase suggests already the formation of a negatively charged super oxide anion O_2^-, whose intra-molecular bond is weakened by the charge uptake [211, 212]. In contrast to the peroxide ion discussed in Chapter 4, the super oxide anion is in principle stable in gas phase [212], but due its net charge, it is likely to react quickly with ambient specimen. However, on surfaces it is frequently found in experiment and theory either as stable species or as a precursor state before the dissociation of the oxygen molecule [214, 211].

The adsorption geometry IVA on the SrO termination in Figure 6.7 is reminiscent of the hydroxyl-pairs discussed in Chapter 5. The most notable difference is the obvious tilting of the uppermost oxygen O(1b) towards the adjacent strontium atoms Sr(1), which is due to the

Table 6.5: Binding energies of the hydrogen co-adsorbed oxygen molecule on both terminations for some specific super-cell sizes. The adsorption geometries VIA and VIB are presented in Figure 6.7 and Figure 6.8.

Surface	**k**-points	N_L	E_b^{IVA} [eV]	E_b^{IVB} [eV]
(1×1)	$(7\times7\times1)$	7	-1.01	-1.05
		9	-1.01	-1.06
		11	-1.01	-1.06
(2×2)	$(4\times4\times1)$	7	-1.82	-1.50
		9	-1.87	-1.58
		11	-1.92	-1.61
(3×3)	$(2\times2\times1)$	7	-1.94	-1.54
		9	-2.00	-1.62
		11	-2.06	-1.65

coulomb attraction of the negatively charged super oxide anion and the cation. Contrariwise, hydrogen atoms in hydroxyl-groups hold usually positive Hirshfeld- or Mulliken charges leading to the upright position of the topmost hydrogen atom in Figure 5.1 due to repulsion from the adjacent strontium atoms. Similar to the pure water adsorption, the oxygen atom O(1a) forming the bond to the surface hydroxyl-group is again sited approximately on the perovskite-type bridging position between the adjacent Sr-atoms Sr(1) and Sr(2) on the surface, The contribution of the bond O(1a)-H(1) to the overall stabilization is estimated in the same manner as in Section 5.4 by placing the adsorbed oxygen molecule at an adsorption site in a distant surface unit cell and calculating the binding energy again. It is found to be -1.54 eV, if calculated in (3×3) surface model with seven atomic layers, which is 0.3 eV higher than the same quantity for the ground state configuration IVA. Thus, the strength of the bond O(1a) – H(1) is approximately 0.4 eV weaker than its counterpart in the hydroxyl-pair in configuration IIA1, but it makes up a substantial part for the preference of the SrO termination. Thus, we feel it is justified to refer to the atomic arrangement IVA in Figure 6.7 as a "oxygen-hydroxyl-pair". In addition, we note that even without this pairing, hydrogen ad-atoms can attract quite possibly oxygen molecules from the gas phase to surface, even in an area extending the direct vicinity of the surface hydroxyl-group.

On the TiO_2-termination, the oxygen molecule binds to the surface titanium atom with a doubly bonded η^2 coordination, not atypical for the formation of a O_2^--anion on metal oxide surfaces [211]. The binding energies in Table 6.10 confirm that for lower coverages the decrease of the binding energy with the super-cell size is similar to for the water adsorption shown in Table 5.1. Consequently, the energy gain should be primarily due to the comparable lattice distortions listed in Table 6.7 and we can therefore not underpin for lower coverages a substantial longer-range coulomb repulsion between the O_2^- species. In contrast, for the adsorption geometry VIA the energetics in Table 6.5 indicate a drastic dependence on the number of layer, indicating again the predominantly vertical progressing lattice distortions. Quite astonishingly, the difference in binding energy between the seven and nine layer surface models is at lower

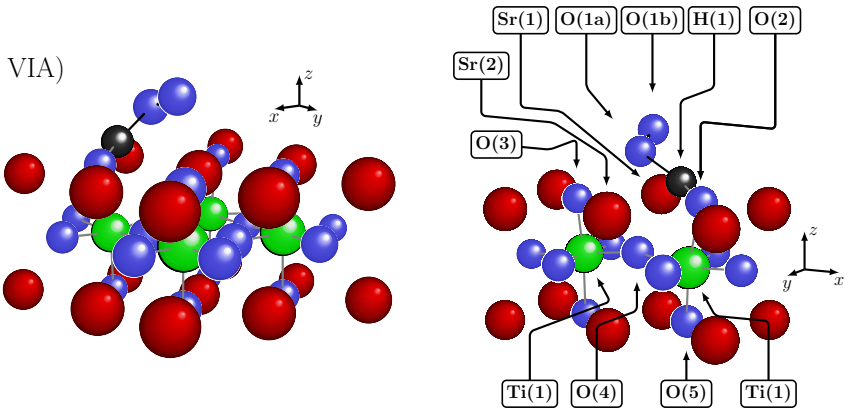

Figure 6.7: Schematic illustration of the hydrogen co-adsorbed oxygen molecule on the SrO-termination of $SrTiO_3(001)$.

Table 6.6: Characteristic bond lengths of the hydrogen co-adsorbed oxygen molecule on the SrO termination, with Δd indicating the change with to the state prior to adsorption. The atomic labeling is defined in Figure 6.7.

VIA	d [Å]	Δd [%]		d [Å]	Δd [%]
O(1a) — O(1b)	1.35	9	O(2) — Ti(1)	2.30	+21
O(1a) — H(1)	1.73	–	O(5) — Ti(1)	1.85	-10
O(1a) — Sr(1)	2.89	–	O(2) — O(3)	4.65	+17
O(1a) — Sr(2)	2.65	–	Ti(1) — O(4)	1.97	≈ 0
O(1b) — Sr(2)	2.57	–	Ti(2) — O(4)	1.97	+2
O(2) — H(1)	0.99	–	Sr(1) — O(2)	3.18	+14
O(4) — O(1a)	3.52	–	Ti(1) — O(3)	1.87	-2

Table 6.7: Characteristic bond lengths of the hydrogen co-adsorbed oxygen molecule on the TiO_2-termination, with Δd indicating the change prior to the adsorption of the hydrogen atom and the oxygen molecule. The atomic labeling is defined in Figure 6.8.

IVB	d [Å]	Δd [%]		d [Å]	Δd [%]
O(1a) — O(1b)	1.33	7	O(2) — Ti(1)	2.22	+19
O(1a) — H(1)	2.49	–	O(2) — Ti(2)	2.09	+10
O(1a) — Ti(1)	2.04	–	O(4) — Ti(1)	1.85	+3
O(2) — H(1)	0.98	–	Ti(3) — O(5)	1.89	-5
Ti(1) — Ti(3)	4.14	+7	Ti(1) — O(5)	2.26	+2

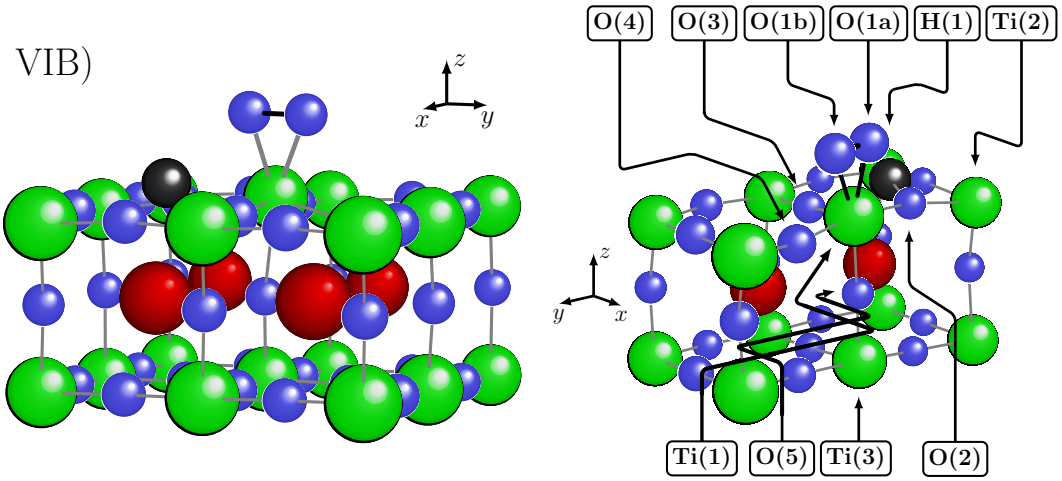

Figure 6.8: Schematic illustration of the hydrogen co-adsorbed oxygen molecule on the TiO_2-termination of $SrTiO_3(001)$.

coverages with 0.6 eV quite substantial and even more smashing, practical identical. Therefore, in complete analogy to the case of the adsorbed water molecule, we have to assign the major responsibility for this behavior to the long-range relaxations in the substrate, which we list in detail in Table 6.7.

6.3.2 Electronic properties

In contrast to the O_2^{2-}-species described in Chapter 5, the super oxide anion bears a non-zero magnetic moment, which is frequently utilized when identifying this species experimentally on surfaces using electron paramagnetic resonance (EPR) [212, 16]. As in the preceding section, we detect this non-zero spin-moment by plotting in Figure 6.9 the spin density defined in Eq. (6.9) in the vicinity of the oxygen molecule. In both geometries VIA and VIB this spin moment is obviously concentrated being concentrated exclusively on the *p*-orbitals. The Hirshfeld- and Mulliken-charges of the two oxygen atoms O(1a) and O(1b) of the adsorbed oxygen molecule measure in configuration VIA and VIB -0.14*e* and -0.32*e* as well as -0.17*e* and -0.32*e*, which is less than the corresponding values found for the per oxide anion in Chapter 4. These properties in combination with the increase oxygen-oxygen bond length fully substantiate the formation of the super oxide anion.

In Figure 6.10 we present the resulting electronic eigenvalue spectrum. Analogously to the adsorbed water molecule, the binding σ molecular orbital of the surface hydroxyls is sited energetically right below the valence band of the substrate, while their π-orbitals do overlap again significantly with the O2*p*-states. Consequently, the electronic structure of the hydroxyl-groups has not changed with respect to the dissociated water molecules in Chapter 5 and underlines the function of the hydrogen atoms as mere electron donors.

The adsorption geometry on the SrO termination shows in total eleven peaks in density of states projected on the oxygen molecule below the Fermi-energy, which may be assigned to the

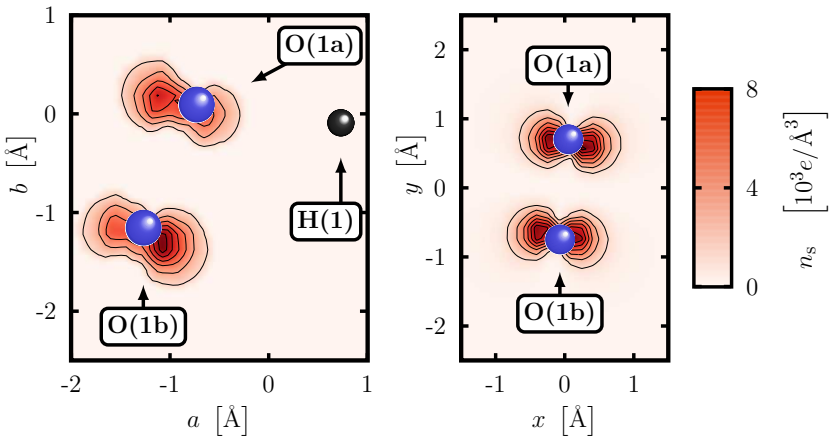

Figure 6.9: Contour plot of the spin-density n_s of the hydrogen co-adsorbed oxygen molecule on the SrO- (left panel) and the TiO_2-termination (right panel). For the SrO-termination, the plotting plane is defined by the atoms of the oxygen molecule and the hydrogen ad-atom, whereas on the TiO_2-termination, the plotting plane was chosen simply to be co-linear to the surface. The atomic labeling is defined in Figure 6.7 and Figure 6.8.

eleven valence electrons in uppermost σ and π-levels of the singly charged oxygen molecule. On the TiO_2-termination, adsorption configuration VIB the O_2^- molecule is aligned almost exactly along the x direction, rendering the whole atomic arrangement slightly more symmetric with respect to the geometry VIA. This lets collapse the two split σ-peaks into one for each spin-channel. The most striking qualitative difference between the oxygen projected spectra for the two terminations is that the additional peak marking the formation of the super-oxide ion is for the case of the SrO termination in the range of the anti-bonding π^*-orbitals at approximately -1 eV, whereas on the TiO_2 termination it lies much lower at -4.5 eV, which is clearly in the ballpark of the bonding π-levels. A second remarkable difference is the location of the highest occupied molecular orbitals clearly within the band-gap on the SrO termination, whereas on the TiO_2-termination the corresponding orbitals lie energetically below the surface states of the lattice oxygen atoms. However, on both terminations the lowest unoccupied molecular orbital is located very close above the Fermi-energy and forms thereby again a shallow acceptor level. With background of the preceding sections, this levels will certainly be occupied in the presence of more hydrogen atoms, i. e. more charge carriers, which will then lead to the formation of a O_2^{2-} species. If not confined, this species is unstable and would shrink the significance of the oxygen-hydrogen pair to an intermediate configuration with only a limited lifetime. This stepwise decomposition is in line with the usual picture of dissociative adsorption of gas phase oxygen due to successive charge transfer from the surface to the molecule [16, 15].

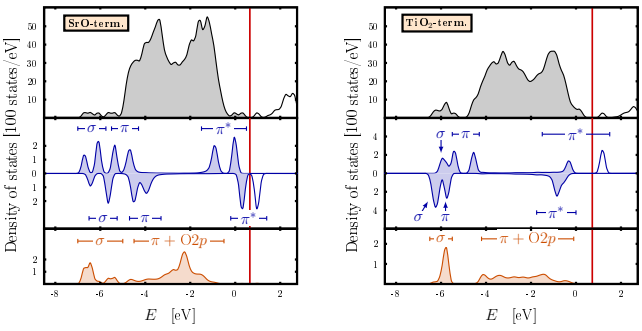

Figure 6.10: Electronic density of states for the hydrogen co-adsorbed oxygen molecule on the SrO (left side) and the TiO_2 termination (right side). The topmost panels show the PDOS of the respective two topmost atomic layers in the surface model, the second ones show the PDOS of the adsorbed oxygen molecule of the two spin-channels and the bottom panel show the PDOS of the hydroxyl, formed by the adsorbed hydrogen and a lattice oxygen atom. The red vertical line denotes the Fermi-level. The eigenvalue spectrum has been aligned to the valence band maximum of the three central layers in the surface model.

7 Conclusions and outlook

Summarizing, we performed an comprehensive DFT-study of oxygen ad-atoms and adsorbed water molecules on the two regular terminations of the $SrTiO_3$(001) surface. This should been viewed as a fundamental step in order to amplify the understanding of the interaction of aqueous species and complex oxide in general. The distinctive feature of this work is that the actual interesting energetics have been converged systematically with respect to the size of the surface model and can therefore be viewed as superior compared to the aforementioned earlier studies on this subject. For the oxygen atom and the water molecule we were able to show that the standard GGA-PBE functional for the exchange correlation gives energetics similar to the much more elaborate "hybrid" approach for rather small model-geometries [208, 34], which inspires confidence in our results for the actually converged geometric model set-ups.

We confirmed that single-oxygen ad-atoms are unstable on the $SrTiO_3$(001) surface from the thermodynamic viewpoint and moreover, they would form a covalent oxygen-oxygen bond. Pure $SrTiO_3$ does not contain such a bond and we expect therefore that oxygen ad-atoms do not promote epitaxial of growth of non-peroxides on $SrTiO_3$.

This focused the attention on the water molecule where it was found that the sheer presence of hydrogen lets the adsorbed oxygen atoms occupy the actual oxygen sites of the continued supporting $SrTiO_3$ crystal lattice, which is in line with the experimental observations of the change of the growth rate with the variation of the hydrogen pressure [52].

For the latter case, converging the energetics with respect to the system size led to a qualitative difference in the binding energy, which develops only for small coverages and relatively many atomic layers. It was found that on the SrO terminated surface the water molecule adsorbs and dissociates without any appreciable barrier followed by the formation of a hydroxyl-pair. This pairing comprises approximately half of the actual binding energy and has to be identified with the actual reason for the preferred water adsorption at SrO terminated domains. On the TiO_2 terminated domains, where such a pairing does not exist, the water molecule may adsorb in a molecular and dissociative mode. The binding energy of these modes was found to be depended on the coverages and thanks to an immaterial dissociation barrier, the adsorption mode on the TiO_2 is also dependent on the actual coverage. These binding energy could then be translated into adsorption free energies, which could be directly compared to the experiment of Iwahori *et al.* [38]. The agreement with the latter was found to be extraordinary good. We then illustrated that the picture of the interplay between $SrTiO_3$ and water suggested by our results does not contradict further, earlier experiments. From today's perspective, the latter seem to have only limited significance, once because the were focusing almost exclusively only on the high water coverages and on the other hand because the exact characterization of the surface itself posed substantial problems for the experimentalists. Therefore, the essential and admittedly somewhat overly didactic message from this study for similar future works is that comparison to experimental data requires energetics that has been converged with respect the parameters of

the model geometry, such that possible artifacts due its the finiteness of its size can be safely excluded.

Following the concept of studying systematically the interaction of $SrTiO_3$ with oxygen and aqueous species in general, we extended the scope in Chapter 6 to the adsorption of single hydrogen atoms and hydroxyl-groups. Here we could demonstrate that the pure semi-local DFT-methodology results in peculiarities, which prohibit to draw expressive conclusions for the experiment, Our preliminary results signalize that effects due to charge localization and charge transfer play the leading role for the adsorption of these, at first glance relatively simple specimen. Indeed, it appears that the feasibility of the calculations for the oxygen ad-atom and the water molecules is closely related to the details of the electronic spectrum, i. e. the occupation of electronic levels at or below the valence band maximum can be identified with the reason why the description of within GGA-PBE for the exchange correlation works here so well. However, there is no obvious reason, why these issues would not be of similar importance for the reaction of more complex atoms and consequently for the actual nucleation and growth process on $SrTiO_3$(001). Consequently, as aforementioned in Chapter 6, we presume that the derivation of physically relevant energetics requires the appliance of methods being capable to capture the correct electronic properties, especially the electronic band gap. With the appliance of the GGA+U method or possibly even higher level theories to the problem of the hydrogen ad-atom in Chapter 6 should lead to a confirmation or at least a reinforced revision of the suggested electrostatic model, which explains the drastic decrease of the binding energy in the presently available data and which is based predominantly on the argumentation in Makov and Payne's original paper [273]. In fact, this issue needs clearly more attention, because Lany and Zunger found the anomalies in the Makov-Payne correction were due to a dielectric screening response [274]. In addition, Oba *et al.* included explicitly the static dielectric constant at room temperature, when discussing the finite size dependence of the defect formation energies in ZnO [284, 285]. However, presently it is unclear, if this is appropriate for the case of $SrTiO_3$ with the drastic increase of the dielectric constant for lower temperatures as it was mentioned in Section 3.1. In addition, we presume that solving this problem serves most likely a fundamental show case for the adsorption of more complex atoms leading to occupied charge states near the conduction band bottom or unoccupied closely above the valence band maximum. Then, in a second step the investigations should focus on the stability of adsorbate configurations in the presence of the impurities or defects reflecting the actual situation in many experiments. In an approximate fashion, these may be modeled by adding or subtracting explicitly charge to the model system in the super-cell. Subsequently the first-principles formalism is extended with a term proportional to the charge of the system times the Fermi energy being the chemical potential of electrons [48]. This extension has already been applied in studies concerning defects in insulators, and with demonstrating the capabilities for the herewith presented, much simpler case confined to strict charge neutrality, we are quite confident that this extension of the first-principle thermodynamics formalism will certainly lead to a substantial amplification of the understanding of the surface chemistry of $SrTiO_3$ and related materials.

A Miscellaneous materials

This appendix briefly summarizes the calculations in order to obtain the total energies of various materials, which were required occasionally in the text. All data presented in this appendix were calculated using the plane-basis-set corresponding to a cut-off energy of 430 eV, which was also one used in the main body of this work. Tests not being shown here confirmed that this basis set was truly sufficient to describe capture the essential properties appropriately. The reported structures were obtained in CASTEP geometry optimization run that were continued until the enthalpy of the system changed less than 1 meV per atom and all force components dropped below 0.005 eV/Å.

A.1 Strontium and titanium

Strontium is an alkaline earth metal of silvery-grayish color and does not occur in pure form naturally. At room temperature it has the face-centered cubic $Fm3m$ structure (α Sr) with the experimental lattice parameters varying between 6.085 Å [122] and 6.073 Å [286]. In addition, two more phases are known, namely the β Sr assuming the hexagonal-closed-packed (hcp) structure at 521 K and the γ Sr forming at 887 K the body-centered cubic (bcc) structure. However, for the sake of clarity we considered only α Sr.

Titanium is the a silvery-colored light weight metal with excellent resistance against corrosion, establishing its importance in for instance air-craft manufacturing and in medicine applications. It has the hexagonal-closed packed (hcp) structure and therefore two lattice parameters to optimize.

Calculating an isolated strontium atom and isolated titanium atom with the computational set-up specified in Appendix B lets us compute the cohesive or formation energy of the bulk strontium and titanium at 0 K:

$$E_{\mathrm{Sr}}^{\mathrm{Form}} = E_{\mathrm{Sr}}^{\mathrm{Bulk}} - E_{\mathrm{Sr}}^{\mathrm{Iso}} \qquad\qquad E_{\mathrm{Ti}}^{\mathrm{Form}} = E_{\mathrm{Ti}}^{\mathrm{Bulk}} - E_{\mathrm{Ti}}^{\mathrm{Iso}} \quad , \tag{A.1}$$

where the $E_{\mathrm{Sr}}^{\mathrm{Bulk}}$ and $E_{\mathrm{Ti}}^{\mathrm{Bulk}}$ refer to the total energy of the bulk metals per atom. Special care had to be taken for the density of the integration points in the Brillouins-zone, and we found that the change of energies $E_{\mathrm{Sr}}^{\mathrm{Bulk}}$ and $E_{\mathrm{Ti}}^{\mathrm{Bulk}}$ is smaller than 0.2 meV, if grids of $(10 \times 10 \times 10)$ and are employed for strontium and titanium, respectively.

A.2 Strontium oxide and strontium peroxide

Strontium oxide is a strong basic acid and formed when pure strontium reacts with oxygen. It has the simple sodium chloride structure, which does not need to be explained any further. In

Table A.1: Formation energy and lattice parameters of bulk strontium and titanium and comparision to the value in literature.

Sr			$E_{\mathrm{Sr}}^{\mathrm{Form}}$ [eV]	a [Å]	**Ti**	$E_{\mathrm{Ti}}^{\mathrm{Form}}$ [eV]	a [Å]	c [Å]
This work	LDA		-1.90	5.79		-6.44	2.87	4.53
	PBE		-1.61	6.04		-5.27	2.91	4.65
Theory	B3PW	[33]		6.22			2.94	4.69
Exp.		[122]		6.09			2.95	4.67

contrast, SrO_2 crystallizes in the carbide structure, which can by obtained from the SrO simply by replacing the oxygen anions with dioxygen dumbbells with their axis aligned the c-direction leading to the tetragonal distortion. This incorporation of a formal O_2^{2-} species with an oxygen-oxygen distance $d_{\mathrm{O-O}}$ in the range from 1.45 Å to 1.54 Å is certainly the recognition feature of the alkaline peroxides, which seems to prevail up to high temperature and pressures [287]. In accordance to our notation, we define the formation- or cohesive energies per formula unit:

$$E_{\mathrm{SrO}}^{\mathrm{Form}} = E_{\mathrm{SrO}}^{\mathrm{Bulk}} - E_{\mathrm{Sr}}^{\mathrm{Bulk}} - \frac{1}{2}E_{\mathrm{O_2}}^{\mathrm{Gas}} \quad , \qquad E_{\mathrm{SrO_2}}^{\mathrm{Form}} = E_{\mathrm{SrO_2}}^{\mathrm{Bulk}} - E_{\mathrm{Sr}}^{\mathrm{Bulk}} - E_{\mathrm{O_2}}^{\mathrm{Gas}} \quad , \tag{A.2}$$

again with $E_{\mathrm{SrO}}^{\mathrm{Bulk}}$ and $E_{\mathrm{SrO_2}}^{\mathrm{Bulk}}$ as total energies per formual unit. These two related materials are a good insulators, SrO for instance has an optical band gap of 5.6 eV [288], which is the reason why convergence of the total energies with respect to the sampling in the Brillouins-zone is achieved quickly using $(6\times6\times6)$ in both cases. Subsequently the lattice parameter of the SrO was determined with a third order polynomial fit, while the three lattice paramters of SrO_2 were determined in geometry optimization. Table A.2 summarizes the results and compares them to the values obtained in the combined experimental and theoretical study by Königstein and Catlow [289, 290]. The lattice parameters can be considered in very good agreement with ours, and we identified their higher formation energies with the different dissociation energy due to the use or our pseudo potentials. Because Königstein and Catlow computed the formation energies with respect to isolated strontium, we subtracted from their data our value for $E_{\mathrm{Sr}}^{\mathrm{Bulk}}$ in order to allow a fair comparision.

Usually the LDA calculates formation and cohsive energies worse than the GGA compared to the experiment, which suggests that the relatively good agreement off the LDA value with the experiment in Table A.2 is certainly somewhat suspicious. It is interesting to note that all methods compute the 0 K formation energy for these materials very similar, the largest difference predicts the LDA with 0.69 eV, while in PBE the formation of SrO is favored with 0.19 eV. Königstein and Catlow calculate this difference in the same range, i. e. using DFT with the PW91 exchange-correlation functional and Hatree-Fock (HF) gives 0.27 eV and 0.41 eV, respectively. This suggests that the further oxidation of SrO is quite possible. However, we are not aware of any experimental study determining the heat of formation of SrO_2.

Table A.2: Formation energy and lattice parameters of SrO and SrO_2 and comparision to the value in literature.

SrO			E_{SrO}^{Form} [eV]	a [Å]	**SrO_2**	$E_{SrO_2}^{Form}$ [eV]	a / c / d_{O-O} [Å]
This work	LDA		-6.26	5.07		-6.95	3.48 / 6.47 / 1.47
	PBE		-5.48	5.20		-5.67	3.57 / 6.81 / 1.51
Theory	B3PW	[33]	-6.16				
	PW91	[289]	-5.22[a]	5.31		-5.49[a]	3.58 / 6.70 / 1.53
	HF	[289]	-5.82[a]	5.19		-6.23[a]	3.65 / 6.69 / 1.45
Exp.		[223]	-6.13				
		[289]		5.16			3.56 / 6.61 / 1.48

[a] The values are corrected with our value for the formation energy of bulk strontium listed in Table A.1.

A.3 Titanium dioxide

Titanium dioxide is probably the most intensively studied transition metal oxide. Listing its properties could easily fill pages and for the sake of brevity we refer the reader to the excellent reviews by Grant [291] and Diebold [47] as well as Henrich's and Cox's book [1]. Titanium oxides exit in several stochiometries, for instance TiO, Ti_2O_3 and TiO_2. The latter is the most stable among these and occurs in essentially three crystal structure, namely rutile, anastase and brookite, of which the first is in turn the most stable. After having ensured that $(6\times6\times8)$ **k**-points provide the required numerical accuracy, the lattice structure was again calculated using in a geometry optimizing run. The rutile structure has two lattice constants and one internal parameter. However, the latter adjusts only the position of the oxygen atoms is found in all calculations consistently to be 0.306, which agrees with the experimental value. The 0 K formation energy is calculated accoring to

$$E_{TiO_2}^{Form} = E_{TiO_2}^{Bulk} - E_{Ti}^{Bulk} - E_{O_2}^{Gas} \quad . \tag{A.3}$$

In Table A.3 we summerize the calculated data. Just as before, the sick description of the gas phase molecule renders the formation too low in PBE, while the LDA over-corrects this with a too strong binding of the TiO_2 crystal. We note that Heifets *et al.*'s hybrid functional performs again extraordinary good with respect to experimental energetics [33].

A.4 Strontium hydroxide and strontium hydroxide monohydrate

Drawing the phase diagram for the water adsorption on $SrTiO_3$ in Section 5.2.3 required the formation energy of anhydrous $Sr(OH)_2$ and its monohydrate $Sr(OH)_2\cdot H_2O$. These are defined

Table A.3: Formation energy and lattice parameters of TiO_2 in the rutile structure.

TiO_2			$E^{\text{Form}}_{TiO_2}$ [eV]	a [Å]	c [Å]
This work	LDA		-10.38	4.55	2.92
	PBE		-9.23	4.64	2.98
Theory	B3PW	[33]	-9.78		
	PBE	[292]	-9.20[a]	4.65	2.97
Exp.		[293]	-9.78		
		[291]		4.59	2.69

[a] This value includes the uncorrected orginal total energy of the oxygen molecule calculated in PBE.

with respect to the gas phase water molecule:

$$E^{\text{Form}}_{Sr(OH)_2} = E^{\text{Bulk}}_{Sr(OH)_2} - E^{\text{Bulk}}_{Sr} - \frac{1}{2}E^{\text{Gas}}_{O_2} - E^{\text{Gas}}_{H_2O}$$
$$E^{\text{Form}}_{Sr(OH)_2\cdot H_2O} = E^{\text{Bulk}}_{Sr(OH)_2\cdot H_2O} - E^{\text{Bulk}}_{Sr} - \frac{1}{2}E^{\text{Gas}}_{O_2} - 2E^{\text{Gas}}_{H_2O} \quad . \tag{A.4}$$

For the sake of brevity, we performed these calculation only with the PBE for the exchange-correlation and did not compare to results obtained in LDA.

For the monohydrate, the procedure was the same as in the privious case. We used the structure data given by Buchmeier and Lutz [247], verified that $(4\times4\times8)$-**k**-points are well sufficient for the targeted total energy and started the geometry optimization. We then obtained the 0 K formation energy of -7.38 eV and lattice vectors of 6.76 Å, 6.24 Å and 3.94 Å versus 6.71 Å, 6.20 Å and 3.64 Å measured by Buchmeier and Lutz.

Unfortunately, we are not aware of any experimental study providing the complete structure anhydrous $Sr(OH)_2$. Because of difficulties to achieve a sufficiently high resolution, Berggruen and Brown and Grueninger and Barnighausen [248, 246] could measure only the positions of the four strontium and eight oxygen, but the not the coordinates of the hydrogen atoms in the othorombic unit cell. We therefore started a series of 55 geometry optimizations, in which the initial positions of the strontium and oxygen atoms were randomly varied about the their experimental coordinates. The hydrogen atoms were then put randomly in a distance ranging from 0.7 Å to 1.4 Å next to the oxygen atoms. Using such a random configuration in advance we verified that $(2\times4\times6)$-**k**-points are certainly enough to obtain the aimed accuracy for the energy as well as for the ionic forces. In contrast to the geometry optimizations performed in the many-body of this thesis, only the orthogonality of the cell vectors was enforced and no further geoemtric or implicit symmetry constraints were applied to the atoms in the unit cell for obvious reasons. Although each step in these geometry optimization was computationally relatively cheap compared to calculations in Chapters 4, 5 and 6, to optimize all 55 structure took several months, because for each run several hundreds, sometimes up to ten-thousand individuals optimizinng steps had to be taken.

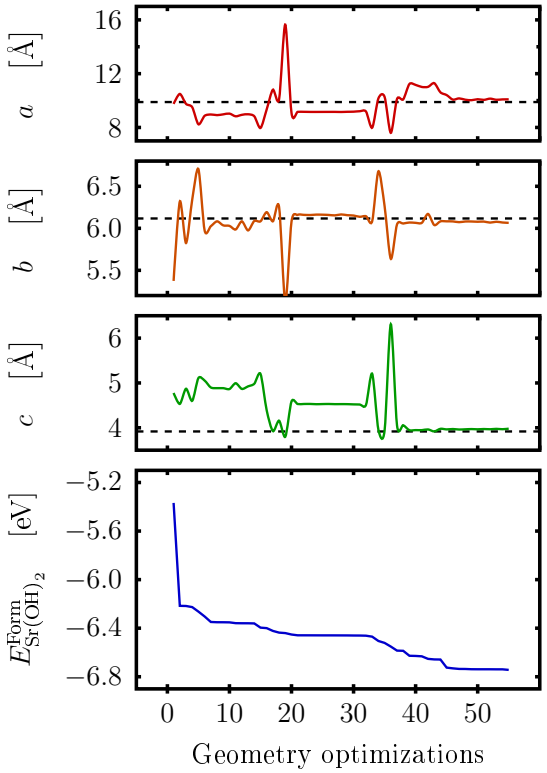

Figure A.1: Different lattice parameters and 0 K formation energies of $Sr(OH)_2$ obtained in 55 independent, randomly initialized geometry optimization runs. The black dashed lines stand for the experimental values given by Berggruen and Brown and Grueninger and Barnighausen [248, 246].

Figure A.1 plots the formation energy and the lattice parameters obtained from all structure optimizations. The good agreement between the measured lattice parameters and those found for the structures lowest in energy raises hopes, that they might have indeed their correspondence in experiment. However, the bulk of the calculated formation energies spreads over a range of 0.5 eV and some structures exhibit lattice parameters deviating up to 50% from the experiment. This points at the existence of possibly many phases of this material, which is also in line findings of Dinescu and Preda [243], who studied the thermal decomposition of variously hydrated strontium hydroxides. They mentioned in total four different variations of $Sr(OH)_2$, which were encountered upon subsequent dehydration of strontium hydroxide octahydrate. Of course, for drawing the phase diagram in Section 5.2 we used the lowest value of value for $E^{\mathrm{Form}}_{\mathrm{Sr(OH)_2}}$, i. e. -6.73 eV.

B Gas phase molecules

This appendix reports the determination of the total energies and geometries of the gas phase species and isolated atoms, which were required in several passages in the text. Still applying periodic boundary conditions, the specimen were modeled in very large super-cells in order to suppress any artificial interaction with the respective replica. Systematic tests showed that orthorhombic super-cells measuring more than $(20 \times 19.5 \times 19.7)$ Å served that purpose in every case presented forward below. Since the electronic eigenstates of gas phase molecules and isolated atoms do not show any dispersion, for all calculations only the Γ-point was employed here for the sampling of the Brillouins-zone.

The gas phase oxygen molecule has in its ground stated its ground-state two unpaired electrons, which results in a non-zero spin moment. The corresponding singlet state is 0.98 eV higher and occurs in practice only as intermediate in chemical reactions [212]. Obviously, this property can be captured only within explicitly spin-polarized calculations. In order to test the basis set, we used the dissociation energy of the oxygen molecule, which is determined from the total energy of the molecule and the isolated atom, respectively:

$$E_{\mathrm{Dis}}(\mathrm{O_2}) = \frac{1}{2}\left[E^{\mathrm{Gas}}_{\mathrm{O_2}} - 2E^{\mathrm{Iso}}_{\mathrm{O}}\right] \quad . \tag{B.1}$$

as reported in Chapter 3, a basis set truncated at the energy of 430 eV ensured a numerical accuracy better 1 meV of this quantity, when using the experimental bond length of 1.23 Å. Afterwards the dissociation energy was calculated as a function of oxygen-oxygen distance $d_{\mathrm{O-O}}$ in order to determine the optimal bond length and the stretching frequency $\nu_{\mathrm{O_2}}$ from a third order polynomial fit. The resulting as well as some published data is compiled in Table B.1 and illustrates the difficulties of the semi-local exchange correlation functionals to describe nature quantitatively correct. The LDA in combination with the used ultra-soft pseudo potentials give the $E_{\mathrm{Dis}}(\mathrm{O_2})$ much to low, while the all-electron calculation in Ref. [294] the improves the situation with respect to the experimental values only slightly. Appliance of the PBE in combination with the ultra-soft potentials seems to come closest to experiment, however, most likely for the wrong reasons. In spite of the error of more than 10% for the dissociation energy, the stretching frequency deviate from the experimental value by only 2%, suggesting that the intramolecular forces are described relatively well.

The steps taken to calculate the total energy of the hydrogen in gas phase were in every minor detail identical to that of the previously presented case of oxygen and we skip a lengthy repetition. The dissociation energy of the hydrogen molecule defined as

$$E_{\mathrm{Dis}}(\mathrm{H_2}) = \frac{1}{2}\left[E^{\mathrm{Gas}}_{\mathrm{H_2}} - 2E^{\mathrm{Iso}}_{\mathrm{H}}\right], \tag{B.2}$$

where the first summand represents the total energy of the hydrogen molecule and the second

Table B.1: Dissociation energy, bond length and stretching frequency ν_{O_2} of the isolated oxygen molecule for different functionals and pseudopotentials.

Oxygen			E_{Dis} [eV]	$d_{\mathrm{O-O}}$ [Å]	ν_{O_2} [cm^{-1}]
This work	LDA		-3.63	1.23	1662
	PBE		-2.81	1.24	1589
	PBE/OTF		-2.94	1.23	1589
Theory	PBE	[292]	-2.94	—	—
	PBE	[239]	-2.93	—	1452
	PBE	[294]	-3.11	1.22	—
Experiment		[211, 212]	-2.54	1.21	1557

Table B.2: Dissociation energy, bond length and stretching frequency ν_{H_2} of the isolated hydrogen molecule for different functionals and pseudopotentials.

Hydrogen			E_{Dis} [eV]	$d_{\mathrm{O-O}}$ [Å]	ν_{O_2} [cm^{-1}]
This work	LDA		-2.45	0.77	4259
	PBE		-2.26	0.75	4347
	PBE/OTF		-2.27	0.75	4323
Theory	LDA	[296]	-2.44	0.77	—
	PBE	[296]	-2.29	0.75	4347
	PBE	[295]	-2.27	0.74	–
	RPA	[295]	-2.36	0.74	–
	Exact	[297]	-4.37	0.74	–
Experiment		[298]	-2.36	0.74	4404

the one of the isolated hydrogen atom. The calculated data is listed in Table B.2 and compares for the PBE again well with the further experimental and theoretical values in the literature. However, we would like to mention here that the calculation of the ground-state wave-functions of a simple H_2-molecule for arbitrary bond length is already a challenge for the density functional theory. For bond lengths close to the energetic minimum in the molecular state, gradient corrected functionals such as the PBE reflect the physics reasonably, however, in the limit $d_{\mathrm{H-H}} \to \infty$, where actually two separated identical hydrogen atoms needs to be described. Here the semi-local functionals delocalized the wave function too much, which results then in an severe overestimation of the dissociations energy. On the other hand, breaking artificially the symmetry by concentrating the spin-up at one proton and the spin-down at the other results in energetics agreeing much better with the experiment, but which are poisened with an unphysical spin polarization [295].

Having now obtained the energies $E_{H_2}^{\mathrm{Gas}}$ and $E_{O_2}^{\mathrm{Gas}}$, we are able calculate the dissociation energy

Table B.3: Dissociation energy, bond length, bond angle and frequencies of the gas phase water molecule for different exchange-correlation functionals and pseudopotentials.

Water			E_{Dis} [eV]	$d_{\mathrm{O-H}}$ [Å]	α	ν_{S} / ν_{A} / ν_{B} [cm^{-1}]
This work	LDA		-2.84	0.98	106°	
	PBE		-2.47	0.99	106°	3823 / 4024 / 1556
	PBE/OTF		-2.47	0.97	106°	
Theory	PBE	[296]	-2.54	0.97	102°	3420 / 3508 / 1597
Experiment		[232]	-2.58	0.96	105°	3657 / 3756 / 1595
		[293]	-2.51			

of the water molecule as defined in Eq. (5.4). For convenience, the geometry of the water molecule was not calculated by polynomial fits but again in a geometry optimization run. In order to test the reliability of applied methods a little further we have also calculated the water molecules' symmetric, asymmetric strechtching as well as the bending frequencies, i. e. ν_{S}, ν_{A} and ν_{B} by diagonalizing the dynamical matrix at the Γ-point. The relatively good agreement of $E_{\mathrm{Dis}}(H_2O)$, the bond-length and the bond angle is contrasted by the remarkable deviation in order of 10%, which also was encountered by previous studies.

As before, a plane-wave basis of 430 eV ensured the convergence of the data listed in Table B.2 and Table B.3.

Bibliography

[1] V. E. Henrich and P. A. Cox, *The surface science of metal oxides* (Cambridge University Press, Cambridge, 1994).

[2] C. J. Först, K. Ashman, C. R.and Schwarz, and P. E. Blöchl, Nature **427**, 53 (2004).

[3] R. A. McKee, F. J. Walker, and M. F. Chisholm, Science **293**, 468 (2001).

[4] R. A. McKee, F. J. Walker, and M. F. Chisholm, Phys. Rev. Lett. **81**, 3014 (1998).

[5] K. Eisenbeiser, J. M. Finder, Z. Yu, J. Ramdani, J. A. Curless, J. A. Hallmark, R. Droopad, W. J. Ooms, L. Salem, S. Bradshaw, and C. D. Overgaard, Appl. Phys. Lett. **76**, 1324 (2000).

[6] R. Droopad, Z. Yu, J. Ramdani, L. Hilt, J. Curless, C. Overgaard, J. L. Edwards, J. Finder, K. Eisenbeiser, and W. Ooms, Mat. Sci. Eng. B **87**, 292 (2001).

[7] J. Robertson, Rep. Prog. Phys. **69**, 327 (2006).

[8] A. Tagantsev, V. Sherman, K. Astafiev, J. Venkatesh, and N. Setter, J. Electroceram. **11**, 5 (2003).

[9] J. M. Phillips, J. Appl. Phys. **79**, 1829 (1996).

[10] N. Setter, D. Damjanovic, L. Eng, G. Fox, S. Gevorgian, S. Hong, A. Kingon, H. Kohlstedt, N. Y. Park, G. B. Stephenson, I. Stolitchnov, A. K. Taganstev, D. V. Taylor, T. Yamada, and S. Streiffer, J. Appl. Phys. **100**, 051606 (2006).

[11] M. E. Lines and A. M. Glass, *Priniciples and applications of ferroelectric and related materials* (Oxford University Press, Walton Street Oxford OX2 6DP, 1979) ISBN 0-19-852003-4.

[12] M. Dawber, K. M. Rabe, and J. F. Scott, Rev. Mod. Phys. **77**, 1083 (2005).

[13] O. Auciello, J. F. Scott, and R. Ramesh, Physics Today **51**, 22 (1998).

[14] C. H. Ahn, K. M. Rabe, and J.-M. Triscone, Science **303**, 488 (2004).

[15] R. Merkle and J. Maier, Phys. Chem. Chem. Phys. **4**, 4140 (2002).

[16] R. Merkle and J. Maier, Angew. Chem. Int. Ed. **47**, 3874 (2008).

[17] C. Tragut and K. H. Härdtl, Sens. Actuators B **4**, 425 (1991), ISSN 0925-4005.

[18] T. Hara, T. Ishiguro, N. Wakiya, and K. Shinozaki, Jpn. J. App. Phys. **47**, 7486 (2008).

[19] A. Ohtomo and H. Y. Hwang, Nature **427**, 423 (2004).

[20] R. Pentcheva and W. E. Pickett, Phys. Rev. B **74**, 035112 (2006).

[21] R. Pentcheva, M. Huijben, K. Otte, W. E. Pickett, J. E. Kleibeuker, J. Huijben, H. Boschker, D. Kockmann, W. Siemons, G. Koster, H. J. W. Zandvliet, G. Rijnders, D. H. A. Blank, H. Hilgenkamp, and A. Brinkman, Phys. Rev. Lett. **104**, 166804 (2010).

[22] G. Herranz, M. Basletić, M. Bibes, C. Carrétéro, E. Tafra, E. Jacquet, K. Bouzehouane, C. Deranlot, A. Hamzić, J.-M. Broto, A. Barthélémy, and A. Fert, Phys. Rev. Lett. **98**, 216803 (2007).

[23] Z. S. Popović, S. Satpathy, and R. M. Martin, Phys. Rev. Lett. **101**, 256801 (2008).

[24] J. Mannhart and D. G. Schlom, Science **327**, 1607 (2010).

[25] Y. Liang and D. A. Bonnell, Surf. Sci. **310**, 128 (1994).

[26] K. Szot and W. Speier, Phys. Rev. B **60**, 5909 (1999).

[27] T. Kubo and H. Nozoye, Phys. Rev. Lett. **86**, 1801 (2001).

[28] N. Erdman, K. R. Poeppelmeier, M. Asta, O. Warschkow, D. E. Ellis, and L. D. Marks, Nature **419**, 55 (2002).

[29] N. B. Brookes, F. M. Quinn, and G. Thornton, Vacuum **38**, 405 (1988).

[30] V. E. Henrich, G. Dresselhaus, and H. J. Zeiger, Phys. Rev. B **17**, 4908 (1978).

[31] N. Erdman and L. D. Marks, Surf. Sci. **526**, 107 (2003).

[32] K. Johnston, M. R. Castell, A. T. Paxton, and M. W. Finnis, Phys. Rev. B **70**, 085415 (2004).

[33] E. Heifets, S. Piskunov, E. A. Kotomin, Y. F. Zhukovskii, and D. E. Ellis, Phys. Rev. B **75**, 115417 (2007).

[34] R. A. Evarestov, A. V. Bandura, and V. E. Alexandrov, Surf. Sci. **601**, 1844 (2007).

[35] J. D. Baniecki, M. Ishiim, K. Kurihara, K. Yamanaka, T. Yano, K. Shinozaki, T. Imada, and Y. Kobayashi, J. Appl. Phys. **106**, 054109 (2009).

[36] P. A. Cox, R. G. Egdell, and P. D. Naylor, J. Electron Spectrosc. Relat. Phenom. **29**, 247 (1983).

[37] L.-Q. Wang, K. F. Ferris, and G. S. Herman, J. Vac. Sci. Technol. A **20**, 239 (2002).

[38] K. Iwahori, S. Watanabe, M. Kawai, K. Kobayashi, H. Yamada, and K. Matsushige, J. Appl. Phys. **93**, 3223 (2003).

[39] J. G. Mavroides, J. A. Kafalas, and D. F. Kolesar, Appl. Phys. Lett. **28**, 241 (1976).

[40] M. S. Wrighton, A. B. Ellis, P. T. Wolczanski, D. L. Morse, H. B. Abrahamson, and D. S. Ginley, J. Am. Chem. Soc **98**, 2774 (1976).

[41] F. T. Wagner, S. Ferrer, and G. A. Somorjai, Surf. Sci. **101**, 462 (1980).

[42] A. Fujishima and K. Honda, Nature **238**, 37 (1972).

[43] A. Kudo, Pure Appl. Chem. **79**, 1917 (2007).

[44] R. Konta, T. Ishii, H. Kato, and A. Kudo, J. Phys. Chem. B **108**, 8992 (2004).

[45] R. G. Carr and G. A. Somorjai, Nature **290**, 576 (1981).

[46] Y. Matsumoto, T. Ohsawa, R. Takahashi, and H. Koinuma, Thin Solid Films **486**, 11 (2005).

[47] U. Diebold, Surf. Sci. Rep. **48**, 53 (2003), ISSN 0167-5729.

[48] C. G. Van de Walle and J. Neugebauer, J. Appl. Phys. **95**, 3851 (2004).

[49] S. A. Chambers, Adv. Mater. **22**, 219 (2010).

[50] M. Leskelä and M. Ritala, Angew. Chem. Int. Ed. **42** (2003), doi:\bibinfo{doi}{10.1002/anie.200301652}.

[51] Q. D. Jiang and J. Zegenhagen, Surf. Sci. **425**, 343 (1999).

[52] T. W. Simpson, I. V. Mitchell, J. C. McCallum, and L. A. Boatner, J. Appl. Phys. **76**, 2711 (1994).

[53] M. Paradinas, L. Garzón, F. Sánchez, R. Bachelet, D. B. Amabilino, J. Fontcuberta, and C. Ocal, Phys. Chem. Chem. Phys. **12**, 4452 (2010).

[54] R. Bachelet, F. Sánchez, J. Santiso, C. Munuera, C. Ocal, and J. Fontcuberta, Chem. Mater. **21**, 2494 (2009).

[55] R. M. Dreizler and E. K. U. Gross, *Density functional theory* (Springer-Verlag, Berlin, 1990).

[56] M. Born and R. Oppenheimer, Ann. Phys. **389**, 457 (1927).

[57] D. R. Hartree, Proc. Camb. Phil. Soc. **24**, 89 (1928).

[58] W. Pauli, Phys. Rev. **58**, 716 (1940).

[59] W. Pauli, Z. Phys. **43**, 601 (1927).

[60] J. Čižek, J. Chem. Phys. **45**, 4256 (1966).

[61] C. Møller and M. S. Plesset, Phys. Rev. **46**, 618 (1934).

[62] L. Hedin, Phys. Rev. **139**, A796 (1965).

[63] G. D. Mahan, *Many particle physics*, 3rd ed. (Kluwer, New York, 2000).

[64] V. Fock, Z. Phys. **61**, 126 (1930).

[65] J. C. Slater, Phys. Rev. **81**, 385 (1951).

[66] P.-O. Löwdin, Phys. Rev. **97**, 1509 (1955).

[67] P. Nozières and D. Pines, Phys. Rev. **111**, 442 (1958).

[68] W. Kohn, Rev. Mod. Phys. **71**, 1253 (1999).

[69] R. O. Jones and O. Gunnarsson, Rev. Mod. Phys. **61**, 689 (1989).

[70] P. Hohenberg and W. Kohn, Phys. Rev. **136**, B864 (1964).

[71] W. Kohn and L. J. Sham, Phys. Rev. **140**, A1133 (1965).

[72] J. F. Janak, Phys. Rev. B **18**, 7165 (1978).

[73] D. M. Ceperley and B. J. Alder, Phys. Rev. Lett. **45**, 566 (1980).

[74] J. P. Perdew and A. Zunger, Phys. Rev. B **23**, 5048 (1981).

[75] M. C. Payne, M. P. Teter, D. C. Allan, T. A. Arias, and J. D. Joannopoulos, Rev. Mod. Phys. **64**, 1045 (1992).

[76] O. Gunnarsson and B. I. Lundqvist, Phys. Rev. B **13**, 4274 (1976).

[77] U. von Barth and L. Hedin, J. Phys. C: Solid State Phys. **5**, 1629 (1972).

[78] D. C. Langreth and M. J. Mehl, Phys. Rev. B **28**, 1809 (1983).

[79] J. P. Perdew, J. A. Chevary, S. H. Vosko, K. A. Jackson, M. R. Pederson, D. J. Singh, and C. Fiolhais, Phys. Rev. B **46**, 6671 (1992).

[80] J. P. Perdew, K. Burke, and Y. Wang, Phys. Rev. B **54**, 16533 (1996).

[81] S.-K. Ma and K. A. Brueckner, Phys. Rev. **165**, 18 (1968).

[82] J. P. Perdew and Y. Wang, Phys. Rev. B **45**, 13244 (1992).

[83] J. P. Perdew, K. Burke, and M. Ernzerhof, Phys. Rev. Lett. **77**, 3865 (1996).

[84] J. P. Perdew, A. Ruzsinszky, G. I. Csonka, O. A. Vydrov, G. E. Scuseria, L. A. Constantin, X. Zhou, and K. Burke, Phys. Rev. Lett. **100**, 136406 (2008).

[85] F. Bloch, Z. Phys. **52**, 555 (1929).

[86] H. J. Monkhorst and J. D. Pack, Phys. Rev. B **13**, 5188 (1976).

[87] J. C. Phillips, Phys. Rev. **112**, 685 (1958).

[88] M. L. Cohen, Rep. Phys. **110**, 293 (1984).

[89] W. E. Pickett, Comput. Phys. Rep. **9**, 115 (1989).

[90] D. R. Hamann, M. Schlüter, and C. Chiang, Phys. Rev. Lett. **43**, 1494 (1979).

[91] A. Zunger and M. L. Cohen, Phys. Rev. **18**, 5449 (1978).

[92] S. G. Louie, S. Froyen, and M. L. Cohen, Phys. Rev. B **26**, 1738 (1982).

[93] G. P. Kerker, J. Phys. C: Solid State Phys. **13**, L189 (1980).

[94] L. Kleinman and D. M. Bylander, Phys. Rev. Lett. **48**, 1425 (1982).

[95] E. L. Shirley, D. C. Allan, R. M. Martin, and J. D. Joannopoulos, Phys. Rev. B **40**, 3652 (1989).

[96] D. Vanderbilt, Phys. Rev. B **41**, 7892 (1990).

[97] K. Laasonen, A. Pasquarello, R. Car, C. Lee, and D. Vanderbilt, Phys. Rev. B **47**, 10142 (1993).

[98] R. P. Feynman, Phys. Rev. B **56**, 340 (1939).

[99] M. Scheffler, J. P. Vigneron, and G. B. Bachelet, Phys. Rev. B **31**, 6541 (1985).

[100] P. Pulay, Mol. Phys. **17**, 197 (1969).

[101] W. H. Press, S. A. Teukolsky, W. T. Vetterling, and B. P. Flannery, *Numercial Recipes in C*, 2nd ed. (Cambridge University Press, New York, 1992).

[102] S. J. Clark, M. D. Segall, C. J. Pickard, P. J. Hasnip, M. L. J. Probert, K. Refson, and M. Payne, Z. Kristallogr. **220**, 567 (2005).

[103] N. D. Mermin, Phys. Rev. **137**, A1441 (1965).

[104] N. Marzari, D. Vanderbilt, and M. C. Payne, Phys. Rev. Lett. **79**, 1337 (1997).

[105] G. Kresse and J. Furthmüller, Phys. Rev. B **54**, 11169 (1996).

[106] S. Kurth, J. P. Perdew, and P. Blaha, Int. J. Quant. Chem. **75**, 889 (1999).

[107] J. P. Perdew, S. Kurth, A. Zupan, and P. Blaha, Phys. Rev. Lett. **82**, 2544 (1999).

[108] S. Kümmel and L. Kronik, Rev. Mod. Phys. **80**, 3 (2008).

[109] O. Gunnarsson, M. Jonson, and B. I. Lundqvist, Phys. Rev. **20**, 3136 (Oct 1979).

[110] D. B. Jochym and S. J. Clark, Phys. Rev. B **76**, 075411 (2007).

[111] A. D. Becke, Phys. Rev. A **38**, 3098 (1988).

[112] C. Adamo and V. Barone, J. Chem. Phys. **110**, 6158 (1999).

[113] A. D. Becke, J. Chem. Phys. **98**, 1372 (1993).

[114] J. P. Perdew, M. Ernzerhof, and K. Burke, J. Chem. Phys. **105**, 9982 (1996).

[115] M. S. Hybertsen and S. G. Louie, Phys. Rev. B **34**, 5390 (1986).

[116] A. Görling, Phys. Rev. A **54**, 3912 (1996).

[117] P. Rinke, A. Qteish, J. Neugebauer, C. Freysoldt, and M. Scheffler, New J. Phys. **7**, 126 (2005).

[118] V. I. Anisimov, J. Zaanen, and O. K. Andersen, Phys. Rev. B **44**, 943 (1991).

[119] V. I. Anisimov, I. V. Solovyev, M. A. Korotin, M. T. Czyżyk, and G. A. Sawatzky, Phys. Rev. B **48**, 16929 (1993).

[120] J. P. Perdew, R. G. Parr, M. Levy, and J. L. Balduz, Phys. Rev. Lett. **49**, 1691 (1982).

[121] H. Jiang, R. I. Gomez-Abal, P. Rinke, and M. Scheffler, Phys. Rev. Lett. **102**, 126403 (2009).

[122] R. W. G. Wyckoff, *Crystal Structures (Suppl. 3,1)*, Vol. 1 (Interscience Publishers Inc., New York, 1958) Chap. 2.

[123] E. Courtens, Phys. Rev. Lett. **29**, 1380 (1972).

[124] P. A. Fleury, J. F. Scott, and J. M. Worlock, Phys. Rev. Lett. **21**, 16 (1968).

[125] B. Alefeld, Z. Phys. **222**, 155 (1969).

[126] G. Shirane and Y. Yamada, Phys. Rev. **177**, 858 (1969).

[127] H. Thomas and K. A. Müller, Phys. Rev. Lett. **21**, 1256 (1968).

[128] R. A. Cowley, Phil. Trans. R. Soc. Lond. A **354**, 2799 (1996).

[129] T. Sakudo and H. Unoki, Phys. Rev. Lett. **26**, 851 (1971).

[130] J. F. Scott and H. Ledbetter, Z. Phys. **104**, 635 (1997).

[131] K. A. Müller and H. Burkard, Phys. Rev. B **19**, 3593 (1979).

[132] J. G. Bednorz and K. A. Müller, Phys. Rev. Lett. **52**, 2289 (1984).

[133] M. Itoh, R. Wang, Y. Inaguma, T. Yamaguchi, Y.-J. Shan, and T. Nakamura, Phys. Rev. Lett. **82**, 3540 (1999).

[134] N. A. Pertsev, A. K. Tagantsev, and N. Setter, Phys. Rev. B **61**, R825 (2000).

[135] J. H. Haeni, P. Irvin, W. Chang, R. Uecker, P. Reiche, Y. L. Li, S. Choudhury, , W. Tian, M. E. Hawley, B. Craigo, A. K. Tagantsev, X. Q. Pan, S. K. Streiffer, L. Q. Chen, S. W. Kirchoefer, J. Levy, and D. G. Schlom, Nature **430**, 758 (2004).

[136] M. P. Warusawithana, C. Cen, C. R. Sleasman, J. C. Woicik, Y. Li, L. F. Kourkoutis, J. A. Klug, H. Li, P. Ryan, L.-P. Wang, M. Bedzyk, D. A. Muller, L.-Q. Chen, J. Levy, and D. G. Schlom, Science **324**, 367 (2009).

[137] W. J. Burke and R. J. Pressley, Solid State Commun. **9**, 191 (1971).

[138] S. Piskunov, E. Heifets, R. I. Eglitis, and G. Borstel, Comp. Mat. Sci. **29**, 165 (2004).

[139] B. Meyer, J. Padilla, and D. Vanderbilt, Faraday Discuss. **114**, 395 (1999).

[140] F. Birch, Phys. Rev. **71**, 809 (1947).

[141] F. D. Murnaghan, Am. J. Math. **59**, 235 (1937).

[142] R. Wahl, D. Vogtenhuber, and G. Kresse, Phys. Rev. B **78**, 104116 (2008).

[143] R. D. King-Smith and D. Vanderbilt, Phys. Rev. B **49**, 5828 (1994).

[144] S. Kimura, J. Yamauchi, M. Tsukada, and S. Watanabe, Phys. Rev. B **51**, 11049 (1995).

[145] Landolt-Börnstein, *Numerical Data and Functional Relations in Science and Technology-Crystal and Solid State Physics* (Springer, Berlin, 1982).

[146] M. Cardona, Phys. Rev. **140**, A651 (1965).

[147] H. E. Weaver, J. Phys. Chem. Sol. **11**, 274 (1959).

[148] E. Hegenbarth, Phys. Stat. Sol. **6**, 333 (1964).

[149] D. C. Meyer, A. A. Levin, S. Bayer, A. Gorbunov, W. Pompe, and P. Paufler, Appl. Phys. A **80**, 515 (2005).

[150] O. N. Tufte and P. W. Chapman, Phys. Rev. **155**, 796 (1967).

[151] H. P. R. Frederikse, W. R. Thurber, and W. R. Hosler, Phys. Rev. **134**, A442 (1964).

[152] T. Higuchi, T. Tsukamoto, N. Sata, M. Ishigame, Y. Tezuka, and S. Shin, Phys. Rev. B **57**, 6978 (1998).

[153] N. Sata, M. Ishigame, and S. Shin, Solid State Ionics **86-88**, 629 (1996).

[154] N. Sata, K. Hiramoto, M. Ishigame, S. Hosoya, N. Niimura, and S. Shin, Phys. Rev. B **54**, 15795 (1996).

[155] J. F. Schooley, W. R. Hosler, and M. L. Cohen, Phys. Rev. Lett. **12**, 474 (1964).

[156] G. Binnig, A. Baratoff, H. E. Hoenig, and J. G. Bednorz, Phys. Rev. Lett. **45**, 1352 (1980).

[157] K. S. Takahashi, D. Matthey, D. Jaccard, J.-M. Triscone, K. Shibuya, T. Ohnishi, and M. Lippmaa, Appl. Phys. Lett. **84**, 1722 (2004).

[158] K. W. Blazey, Phys. Rev. Lett. **27**, 146 (1971).

[159] A. H. Kahn and A. J. Leyendecker, Phys. Rev. **135**, A1321 (1964).

[160] E. Heifets, R. I. Eglitis, E. A. Kotomin, J. Maier, and G. Borstel, Surf. Sci. **513**, 211 (2002).

[161] G. Cappellini, S. Bouette-Russo, B. Amadon, C. Noguera, and F. Finocchi, J. Phys.: Condens. Matter **12**, 3671 (2000).

[162] K. van Benthem, C. Elsasser, and R. H. French, J. Appl. Phys. **90**, 6156 (2001).

[163] B. N. Figgis and M. A. Hitchman, *Ligand field theory and its applications* (Wiley-VCH, New York, 2000).

[164] N. Nakagawa, H. Y. Hwang, and D. A. Muller, Nat. Mater. **5**, 204 (2006).

[165] F. L. Hirshfeld, Theoret. Chim. Acta **44**, 129 (1977).

[166] M. D. Segall, R. Shah, C. J. Pickard, and M. C. Payne, Phys. Rev. B **54**, 16317 (1996).

[167] J. Goniakowski and C. Noguera, Surf. Sci. **365**, L657 (1996), ISSN 0039-6028.

[168] D. Deak, Mater. Sci. Technol. **23**, 127 (2007).

[169] M. Henzler and M. Göpel, *Oberflächenphysik des Festkörpers* (Teubner, Stuttgart, 1994).

[170] W. Demtröder, *Experimentalphysik 3* (Springer, Heidelberg, 2000).

[171] G. Binnig, H. Rohrer, C. Gerber, and E. Weibel, Appl. Phys. Lett. **40**, 178 (1982).

[172] G. Binnig, C. F. Quate, and C. Gerber, Phys. Rev. Lett. **56**, 930 (1986).

[173] H. W. Hao, A. M. Baro, and J. J. Saenz, J. Vac. Sci. Technol. B **9**, 1323 (1991).

[174] G. Meyer and N. M. Amer, Appl. Phys. Lett. **57**, 2089 (1990).

[175] R. M. Overney, E. Meyer, J. Frommer, D. Brodbeck, R. Lüthi, L. Howald, H.-J. Gintherodt, M. Fujihira, H. Takano, and Y. Gotoh, Nature **359**, 133 (1992).

[176] R. Lüthi, E. Meyer, H. Haefke, L. Howald, W. Gutmannsbauer, M. Guggisberg, M. Bammerlin, and H.-J. Güntherodt, Surf. Sci. **338**, 247 (1995).

[177] B. Cord and R. Courths, Surf. Sci. **162**, 34 (1985).

[178] M. Kawasaki, K. Takahashi, T. Maeda, R. Tsuchiya, M. Shinohara, O. Ishiyama, T. Yonezawa, M. Yoshimoto, and H. Koinuma, Science **266**, 1540 (1994).

[179] Y. Kido, T. Nishimura, Y. Hoshino, and H. Namba, Nucl. Instr. and Meth. in Phys. Res. B **161-163**, 371 (2000).

[180] T. Nishimura, A. Ikeda, H. Namba, T. Morishita, and Y. Kido, Surf. Sci. **421**, 273 (1999).

[181] M. Yoshimoto, T. Maeda, K. Shimozono, H. Koinuma, M. Shinohara, O. Ishiyama, and F. Ohtani, Appl. Phys. Lett. **65**, 3197 (1994).

[182] P. A. W. van der Heide, Q. D. Jiang, Y. S. Kim, and J. W. Rabalais, Surf. Sci. **473**, 59 (2001).

[183] M. Naito and H. Sato, Physica C **229**, 1 (1994).

[184] Q. Jiang and J. Zegenhagen, Surf. Sci. **367**, L42 (1996).

[185] T. Matsumoto, H. Tanaka, T. Kawai, and S. Kawai, Surf. Sci. **278**, L153 (1992).

[186] H. Tanaka, T. Matsumoto, T. Kawai, and S. Kawai, Surf. Sci. **318**, 29 (1994).

[187] Y. Liang and D. A. Bonnell, Surface Science **285**, L510 (1993).

[188] S. N. Ruddlesden and P. Popper, Acta Cryst. **10**, 538 (1957).

[189] S. N. Ruddlesden and P. Popper, Acta Cryst. **11**, 54 (1958).

[190] M. R. Castell, Surf. Sci. **516**, 33 (2002).

[191] M. R. Castell, Surf. Sci. **505**, 1 (2002).

[192] N. Erdman and L. D. Marks, Surf. Sci. **526**, 107 (2003).

[193] L. M. Liborio, C. G. Sánchez, A. T. Paxton, and M. W. Finnis, J. Phys.: Condens. Matter **17**, L223 (2005).

[194] V. Vonk, S. Konings, G. J. van Hummel, S. Harkema, and H. Graafsma, Surf. Sci. **595**, 183 (2005).

[195] R. Herger, P. R. Willmott, O. Bunk, C. M. Schlepütz, B. D. Patterson, B. Delley, V. L. Shneerson, P. F. Lyman, and D. K. Saldin, Phys. Rev. B **76**, 195435 (2007).

[196] R. Herger, P. R. Willmott, O. Bunk, C. M. Schlepütz, B. D. Patterson, and B. Delley, Phys. Rev. Lett. **98**, 076102 (2007).

[197] C. Cheng, K. Kunc, and M. H. Lee, Phys. Rev. B **62**, 10409 (2000).

[198] J. Padilla and D. Vanderbilt, Surf. Sci. **418**, 64 (1998).

[199] E. Heifets, R. I. Eglitis, E. A. Kotomin, J. Maier, and G. Borstel, Phys. Rev. B **64**, 235417 (2001).

[200] S. Piskunov, E. A. Kotomin, E. Heifets, J. Maier, R. I. Eglitis, and G. Borstel, Surf. Sci. **575**, 75 (2005), ISSN 0039-6028.

[201] F. Lin, S. Wang, F. Zheng, G. Zhou, J. Wu, B.-L. Gu, and W. Duan, Phys. Rev. B **79**, 035311 (2009).

[202] R. I. Eglitis and D. Vanderbilt, Phys. Rev. B **77**, 195408 (2008).

[203] N. Bickel, G. Schmidt, K. Heinz, and K. Müller, Phys. Rev. Lett. **62**, 2009 (1989).

[204] T. Hikita, T. Hanada, M. Kudo, and M. Kawai, Surf. Sci. **287-288**, 377 (1993).

[205] P. W. Tasker, J. Phys. C: Solid State Phys. **12**, 4977 (1979).

[206] D. J. Singh, Ferroelectrics **164**, 143 (1995).

[207] S. Tinte, M. G. Stachiotti, C. O. Rodriguez, D. L. Novikov, and N. E. Christensen, Phys. Rev. B **58**, 11959 (1998).

[208] S. Piskunov, Y. F. Zhukovskii, E. A. Kotomin, E. Heifets, and D. E. Ellis, Mat. Res. Soc. Symp. Proc. **894**, 295 (2006).

[209] H. Guhl, W. Miller, and K. Reuter, Surf. Sci. **604**, 372 (2010).

[210] J. Carrasco, F. Illas, N. Lopez, E. A. Kotomin, Y. F. Zhukovskii, R. A. Evarestov, Y. A. Mastrikov, S. Piskunov, and J. Maier, Phys. Rev. B **73**, 064106 (2006).

[211] H. Allen, O. Hill, and D. G. Tew, in *Comprehensive coordination chemistry*, edited by G. Wilkinson, R. D. Gillard, and J. A. Cleverty (Pergamon Oxford, 1970).

[212] M. Che and A. J. Trench, Adv. Catal. **32**, 1 (1983).

[213] L. N. Kantorovich and M. J. Gillan, Surf. Sci. **374**, 373 (1997).

[214] A. Gurlo, Chem. Phys. Chem. **7**, 2041 (2006).

[215] D. Schwarzenbach, Inorg. Chem. **9**, 2391 (1970).

[216] L. Vaska, Acc. Chem. Res. **9**, 175 (1976).

[217] P. Hänggi, P. Talkner, and M. Borkovec, Rev. Mod. Phys. **62**, 251 (1990).

[218] G. H. Vineyard, J. Phys. Chem. Sol. **3**, 121 (1957).

[219] M. Scheffler and J. Dabrowski, Philos. Mag. A **58**, 107 (1988).

[220] K. Reuter and M. Scheffler, Phys. Rev. B **65**, 035406 (2001).

[221] L. D. Landau and E. M. Lifschitz, *Lehrbuch der theoretischen Physik V – Statistische Physik (Teil 1)*, 5th ed. (Akademie-Verlag, Berlin, 1979).

[222] L. D. Landau and E. M. Lifschitz, *Lehrbuch der theoretischen Physik II – Quantenmechanik*, 5th ed. (Akademie-Verlag, Berlin, 1979).

[223] D. R. Stull and H. Prophet, *JANAF Thermochemical Tables*, 2nd ed. (U.S. National Bureau of Standards, Washington D. C., 1971) `http://webbook.nist.gov/chemistry/`.

[224] R. Bachelet, F. Sanchez, F. Palomares, C. Ocal, and J. Fontcuberta, Appl. Phys. Lett. **95**, 141915 (2009).

[225] R. A. Evarestov, E. A. Kotomin, and Y. F. Zhukovskii, Int. J. Quant. Chem. **106**, 2173 (2006).

[226] J. T. S. Irvine, D. J. D. Corcoran, A. Lashtabeg, and J. C. Walton, Solid State Ionics **154**, 447 (2002).

[227] H. Guhl, W. Miller, and K. Reuter, Phys. Rev. B **81**, 155455 (2010).

[228] B. Santra, A. Michaelides, and M. Scheffler, J. Chem. Phys. **127**, 184104 (2007).

[229] L.-Q. Wang, K. F. Ferris, S. Azad, and M. H. Engelhard, J. Phys. Chem. B **109**, 4507 (2005).

[230] F. Lin, F. W. Zheng, and F. P. Ouyang, Acta Phys. Sin. **58**, S193 (2009).

[231] M. A. Henderson, Surf. Sci. Rep. **46**, 1 (2002).

[232] P. A. Thiel and T. E. Madey, Surf. Sci. Rep. **7**, 211 (1987).

[233] J. Carrasco, F. Illas, and N. Lopez, Phys. Rev. Lett. **100**, 016101 (2008).

[234] G. Henkelman, B. P. Uberuaga, and H. Jónsson, J. Chem. Phys. **113**, 9901 (2000).

[235] S. R. Bahn and K. W. Jacobsen, Comput. Sci. Eng. **4**, 56 (2002).

[236] G. Geneste and B. Dkhil, Phys. Rev. B **79**, 235420 (2009).

[237] V. A. Ranea, W. F. Schneider, and I. Carmichael, Surf. Sci. **602**, 268 (2008), ISSN 0039-6028.

[238] K. C. Hass, W. F. Schneider, A. Curioni, and W. Andreoni, Science **282**, 265 (1998).

[239] Q. Sun, K. Reuter, and M. Scheffler, Phys. Rev. B **67**, 205424 (2003).

[240] K. Iwahori, S. Watanabe, K. T., M. Kawai, A. Saito, Y. Kuwahara, and M. Aono, Jpn. J. Appl. Phys. **38**, 3946 (1999).

[241] K. Iwahori, S. Watanabe, M. Kawai, K. Mizuno, K. Sasaki, and M. Yoshimoto, J. Appl. Phys. **88**, 7099 (2000).

[242] H. S. Kato, S. Shiraki, M. Nantoh, and M. Kawai, Surf. Sci. **544**, L722 (2003).

[243] R. Dinescu and M. Preda, J. Thermal Anal. **5**, 465 (1973).

[244] J. S. Ricci, R. C. Stevens, R. K. McMullan, and W. T. Klooster, Acta Cryst. B **61**, 381 (2005).

[245] H. G. Smith, Acta Cryst. **6**, 604 (1953).

[246] H. W. Grueniger and H. Bänighausen, Z. anorg. allg. Chem. **368**, 53 (1969).

[247] W. Buchmeier and H. D. Lutz, Z. anorg. allg. Chem. **528**, 131 (1986).

[248] G. Berggruen and A. Brown, Acta Chem. Scand. **25**, 1377 (1971).

[249] R. I. Masel, *Principles of adsorption and reaction on solid surfaces* (John Wiley and Sons Inc., New York, 1996).

[250] P. Redhead, Vaccum **12**, 203 (1962).

[251] V. E. Henrich, G. Dresselhaus, and H. J. Zeiger, Solid State Commun. **24**, 623 (1977).

[252] C. Webb and M. Lichtensteiger, Surf. Sci. **107**, L345 (1981).

[253] S. Eriksen, P. D. Naylor, and R. G. Egdell, Spectrochim. Acta A. **43**, 1535 (1987).

[254] I. W. Owen, N. B. Brookes, C. H. Richardson, D. R. Warburton, F. M. Quinn, D. Norman, and G. Thornton, Surf. Sci. **178**, 897 (1986).

[255] S. Ferrer and G. A. Somorjai, Surf. Sci. **94**, 41 (1980).

[256] V. E. Henrich, G. Dresselhaus, and H. J. Zeiger, J. Vac. Sci. Technol. **15**, 534 (1978).

[257] N. B. Brookes, G. Thornton, and F. M. Quinn, Solid State Commun. **64**, 383 (1987).

[258] N. Mulakaluri, R. Pentcheva, M. Wieland, W. Moritz, and M. Scheffler, Phys. Rev. Lett. **103**, 176102 (2009).

[259] P. Thissen, G. Grundmeier, S. Wippermann, and W. G. Schmidt, Phys. Rev. B **80**, 245403 (2009).

[260] P. J. D. Lindan, N. M. Harrison, and M. J. Gillan, Phys. Rev. Lett. **80**, 762 (1998).

[261] J. Carrasco, A. Michaelides, M. Forster, S. Haq, R. Raval, and A. Hodgson, Nat. Mater. **8**, 427 (2009).

[262] J. M. Sanchez, F. Ducastelle, and D. Gratias, Physica A **128**, 334 (1984).

[263] C. Stampfl, H. J. Kreuzer, S. H. Payne, H. Pfnür, and M. Scheffler, Phys. Rev. Lett. **83**, 2993 (1999).

[264] N. Goldenfeld, *Lectures on phase transitions and the renomalisation group* (Westview Press, 1992).

[265] D. T. Gillespie, J. Comp. Phys. **22**, 403 (1976).

[266] W. Münch, K. D. Kreuer, G. Seifertli, and J. Majer, Solid State Ionics **125**, 39 (1999).

[267] G. Weber, S. Kapphan, and M. Wöhlecke, Phys. Rev. B **34**, 8406 (1986).

[268] N. Sata, K. Hiramoto, M. Ishigame, S. Hosoya, N. Niimura, and S. Shin, Phys. Rev. B **54**, 15795 (1996).

[269] T. Norby and Y. Larring, Cur. Opin. Solid State Mater. Sci. **2**, 593 (1997).

[270] G. Koster, B. L. Kropman, G. J. H. M. . Rijnders, D. H. A. Blank, and H. Rogalla, Applied Physics Letters **73**, 2920 (1998).

[271] G. Koster, G. Rijnders, D. H. A. Blank, and H. Rogalla, Physica C **339**, 215 (2000), ISSN 0921-4534.

[272] M. Leslie and N. J. Gillan, J. Phys. C: Solid State Phys. **18**, 973 (1985).

[273] G. Makov and M. C. Payne, Phys. Rev. B **51**, 4014 (1995).

[274] S. Lany and A. Zunger, Phys. Rev. B **78**, 235104 (2008).

[275] P. P. Ewald, Ann. Phys. **369**, 253 (1921).

[276] B. R. A. Nijboer and F. W. De Wette, Physica **23**, 309 (1957).

[277] S. W. de Leeuw, J. T. Perram, and E. R. Smith, Proc. R. Soc. Lond. A **373**, 27 (1980).

[278] S. W. de Leeuw, J. T. Perram, and E. R. Smith, Proc. R. Soc. Lond. A **373**, 57 (1980).

[279] J. M. Ziman, *Principles of the theory of solids*, 2nd ed. (Cambridge University Press, London, 1972).

[280] E. Finazzi, C. Di Valentin, G. Pacchioni, and A. Selloni, J. Chem. Phys. **129**, 154113 (2008).

[281] B. Reihl, J. G. Bednorz, K. A. Müller, Y. Jugnet, G. Landgren, and J. F. Morar, Phys. Rev. B **30**, 803 (1984).

[282] K. Szot, W. Speier, R. Carius, U. Zastrow, and W. Beyer, Phys. Rev. Lett. **88**, 075508 (2002).

[283] U. Gerstmann, P. Deák, R. Rurali, B. Aradi, F. Th., and H. Overhof, Physica B **340-342**, 190 (2003).

[284] F. Oba, A. Togo, I. Tanaka, J. Paier, and G. Kresse, Phys. Rev. B **77**, 245202 (2008).

[285] N. Ashkenov, B. N. Mbenkum, C. Bundesmann, V. Riede, M. Lorenz, D. Spemann, E. M. Kaidashev, A. Kasic, M. Schubert, M. Grundmann, G. Wagner, H. Neumann, V. Darakchieva, H. Arwin, and B. Monemar, J. Appl. Phys. **93**, 126 (2003).

[286] E. A. Sheldon and A. J. King, Acta Cryst. **6**, 100 (1952).

[287] H. Föppl, Z. anorg. allg. Chem. **291**, 12 (1957).

[288] B. P. Johnson and E. B. Hensley, Phys. Rev. **180**, 931 (1969).

[289] M. Königstein and C. R. A. Catlow, J. Solid State Chem. **140**, 103 (1998).

[290] M. Königstein, A. A. Sokol, and C. R. A. Catlow, Phys. Rev. B **60**, 4594 (1999).

[291] F. A. Grant, Rev. Mod. Phys. **31**, 646 (1959).

[292] P. M. Kowalski, B. Meyer, and D. Marx, Phys. Rev. B **79**, 115410 (2009).

[293] J. D. Cox, D. D. Wagman, and V. A. Medvedev, *CODATA key values for thermodynamics* (Hemisphere Publishing Corp., New York, 1984) `http://webbook.nist.gov/chemistry/`.

[294] A. Kiejna, G. Kresse, J. Rogal, A. D. Sarkar, K. Reuter, and M. Scheffler, Phys. Rev. B **73**, 035404 (2006).

[295] M. Fuchs, Y.-M. Niquet, X. Gonze, and K. Burke, J. Chem. Phys. **122**, 094116 (2005).

[296] Q. Sun, K. Reuter, and M. Scheffler, Phys. Rev. B **70**, 235402 (2004).

[297] W. Kolos and C. C. J. Roothaan, Rev. Mod. Phys. **32**, 219 (1960).

[298] *CRC Handbook of Chemistry and Physics*, 81st ed. (CRC Press, Boca Raton, 2000).

Danksagung

Der größte Dank gebührt selbstverständlich dem Direktor des Leibniz Instituts für Kristallzüchtung (IKZ) Prof. R. Fornari und Dr. W. Miller sowie den übrigen Mitgliedern der AG Numerik des IKZ für die Unterstützung meiner Arbeit, obgleich Thema und Methodik für das IKZ relativ neu sind.

Ausdrücklich möchte ich mich aber auch bei Karsten Reuter für die Betreuung in seiner Nachwuchsgruppe in der Theorieabteilung des Fritz-Haber-Instituts bedanken. Die Diskussionen mit ihm sowie seine vielfältigen Anmerkungen und Hinweise haben zu einem ganz erheblichen Teil zur Fertigstellung dieser Arbeit beigetragen,
Das gilt natürlich auch für die Mitglieder oder die ehemaligen Mitglieder der seiner Nachwuchsgruppe Falko Axmann, Ralf Gehrke, Matthias Gramzow, Max Hoffmann, Jelena Jelić, Matteo Maestri, Claudia Mangold, Sebastian Matera, Eric McNellis, Jörg Meyer, Michael Rieger und Andrea Sanfilippo, ohne deren fachliche oder auch nicht weniger wichtige technische Hinweise diese Arbeit ebenfalls nicht denkbar wäre.

Darüber hinaus habe ich in Gesprächen mit Javier Carrasco, Martin Fuchs, Mathis Gruber, Sergey Levchenko, Matthias Scheffler, Annabella Selloni, Norina Richter, Patrick Rinke und Gou-Xu Zhang Anregungen und Impulse erhalten, die für diese Arbeit ebenfalls nicht unbedeutend sind.

Selbständigkeitserklärung

Ich erkläre, dass ich die vorliegende Arbeit selbständig und nur unter Verwendung der angegebenen Literatur und Hilfsmittel angefertigt habe.

Berlin, den 28.01.2008 Hannes Guhl